

INTEGRATED FLUORESCENCE SENSOR

A DISSERTATION

SUBMITTED TO THE DEPARTMENT OF ELECTRICAL ENGINEERING

AND THE COMMITTEE ON GRADUATE STUDIES

OF STANFORD UNIVERSITY

IN PARTIAL FULFILLMENT OF THE REQUIREMENTS

FOR THE DEGREE OF

DOCTOR OF PHILOSOPHY

Evan P. Thrush

December 2004

© Copyright by Evan P. Thrush 2005
All Rights Reserved

I certify that I have read this dissertation and that in my opinion it is fully adequate, in scope and quality, as dissertation for the degree of Doctor of Philosophy.

James S. Harris, Jr., Principal Advisor

I certify that I have read this dissertation and that in my opinion it is fully adequate, in scope and quality, as dissertation for the degree of Doctor of Philosophy.

Stephen J. Smith

I certify that I have read this dissertation and that in my opinion it is fully adequate, in scope and quality, as dissertation for the degree of Doctor of Philosophy.

Peter Peumans

Approved for the University Committee on Graduate Studies.

ABSTRACT

Miniaturized and total analysis systems (μ TAS) or lab-on-a-chip technology is epitomized by the integration of complex microfluidic systems (such as channels, mixers, pumps, particulate filters, etc.) with complex chemical processing and analysis (Polymerase Chain Reaction (PCR), DNA fluorescent labeling, capillary electrophoresis, etc.) to create compact biological and chemical analysis systems. μ TAS has received much attention due to its potential application in medical diagnostics and high-throughput research instrumentation. Fluorescence sensing remains one of the most widely used detection technologies for μ TAS due to its superior sensitivity and specificity. Unfortunately, traditional fluorescence sensing systems remain bulky, non-portable and expensive, stifling the application of μ TAS in portable diagnostics and medical care. The theme of this research is to capitalize on optoelectronics developed for telecommunications to create an integrated sensing solution. Integrated semiconductor optoelectronic devices can provide a portable, parallel and inexpensive solution for on-chip fluorescence sensing.

In this work, vertical-cavity surface-emitting lasers (VCSELs) operating at 773nm, PIN photodetectors and emission filters are monolithically integrated to form the optoelectronic basis of the integrated fluorescence sensor. These optoelectronic components are placed in a proximity sensing architecture, where the VCSEL is surrounded by a donut photodetector. This is the first work to integrate a laser and photodetector in such close proximity ($\approx 50\mu\text{m}$) towards fluorescence sensing. By bringing the optoelectronic components in such close proximity, laser background sources are created that limit the sensor sensitivity. Laser background sources are characterized, and design solutions are proposed and implemented to reduce laser background. With integrated metal optical blocks, the internal optical isolation between the photodetector and laser is greater than 10^6 , which shows that highly sensitive detection is possible despite the close optoelectronic integration. With the metal blocking structures, the dominant source of laser background is due to reflections occurring above the sensor. The sensor is particularly sensitive to these reflections due to sub-optimal

performance from the emission filter. With reflections taken into account, the total optical isolation between the laser and photodetector is approximately 2×10^4 .

The sensor is integrated with microfluidic channels to test sensor sensitivity. The experimental and theoretical limit of detection of IR-800 dye is determined to be 250nM and 40nM respectively. These detection limits are sufficient for applications such as clinical chemistry and immunology. Large increases in sensor sensitivity are possible through the systematic reduction of laser background and will enable a wider range of applications. Results from this first generation sensor suggest that order of magnitude increases in sensitivity will be possible by improving the filter performance and increasing spatial filtration. It is believed that this technology holds great potential to reach detection limits less than 1nM and compete against bulk optical approaches.

ACKNOWLEDGEMENTS

The journey towards a Ph.D. degree can be treacherous but also exciting and pleasurable. I have many to thank for helping me through the hard times and sharing the good times throughout my graduate work. First and foremost, I would like to thank my advisor Professor James S. Harris, Jr. or, as we like to call him, Coach. Coach created a wonderful open research environment which allowed me to pursue my interests unfettered and gain confidence from the positive results of my own free thinking. His support for me and my research was always strong, which fueled me along until the end of my thesis and beyond! I would like to thank Professor Stephen Smith for being my unofficial co-advisor during this work. His excitement and enthusiasm is truly inspirational. Prof. Smith provided the biological and fluorescence sensing expertise in order to steer us towards fruitful research endeavors. I would also like to thank Professor W. E. Moerner for collaborating with us and lending his chemistry expertise and laboratory instrumentation. Professors Olav Solgaard and Kishna Shenoy were a great support for me and always available to support my research project and lend advice towards future endeavors. I would like to thank Professor Peter Peumans for agreeing to be on my Ph.D. committee under short notice and giving me feedback on this thesis. Finally, I would like to thank my undergraduate advisors at Trinity University, Professors Farzan Aminian and David Hough, who gave me the confidence and courage to attend graduate school.

There were many fellow colleagues at Stanford who helped me technically and emotionally throughout my graduate work. I would like to thank Dr. Ofer Levi for working with me over the years and always pushing me to excel in research. Laura Cook, Tom Lee, Meredith Lee and Ke Wang were members of our bio-research team and contributed to this work in various ways. I would like to thank my roommate Rafael Aldaz for being a great friend and help in graduate school. He was always available to lend a helping hand whether in discussing processing or debugging computer networks. Wonill Ha and Glen Carey were instrumental to this research for the epitaxial growth of the sensors at Novalux, Inc. Senior Harris group members, Chien-Chung Li and Thierry

Pinguet, helped me begin my graduate career by teaching me processing and other basic laboratory techniques. I would like to thank Mark Wistey, Seth Bank, Lynford Goddard, Homan Yuen and Hopil Bae for helpful discussions and MBE growth favors. I would like to thank Jason Deich and Andrea Kurtz for collaborating with us and helping us with chemistry.

I would like to give a special thanks to Gail Chun-Creech, whose administrative skills keep the Harris group going year after year. She was always extremely helpful and always gave her help with a smile. I would also like to thank the CIS staff and technicians for providing me the infrastructure needed to pursue this work.

The work for this dissertation was largely funded by the Defense Advanced Research Project Agency (DARPA) contract #MDA972-00-1-0032. I would also like to thank the National Science Foundation (NSF) for supporting me for three years under a NSF Graduate Fellowship. Agilent Technologies provided student funding during the last year of graduate school through the Stanford Photonics Research Center.

Last but not least, I would like to thank my many friends and family for their undying support. My good friends in the bay area who kept me company on a more frequent basis include my friend and girlfriend Jen, my roommates, Rafael and Sameer, my Aunt Ann, Mark Morris, Josh Sperry, Jonathan Ziebarth, Scott Brave, Vijit, Seth, Mike Weimer, Gigi, Andy Hayes, Dan Grupp and Richard. My older friends who continue to provide me inspiration and support include Jason, Omar, Matt Emerson, Jonathan Fairman, Lewis and the Kappas.

Finally, I would like to thank my Mother and Father for their love and generosity. My bother continues to inspire me to a more natural way of life by seeking happiness in nature. My step-parents, Mike and Sandy, have been a great support to me over the years. My Grandfather Miller has been a great inspiration to me and continues to be. I would like to thank both of my Grandmothers for their love and support. Finally, I would like to dedicate this dissertation to my friends and family.

CONTENTS

Abstract.....	iv
Acknowledgements.....	vi
List of tables.....	xi
List of figures.....	xii
Chapter 1 Introduction.....	1
1.1 Miniaturized and total analysis systems.....	1
1.2 Molecular sensing.....	3
1.3 Integrated fluorescence sensing.....	5
1.4 Outline.....	6
Chapter 2 Laser induced fluorescence detection.....	8
2.1 Basic physics of fluorescence.....	8
2.2 Excitation and fluorescence signal.....	11
2.2.1 Basic description of LIF system.....	11
2.2.2 Absorption of excitation light.....	13
2.2.3 Emitted fluorescence and collection efficiency.....	13
2.2.4 Detector signal from fluorescence.....	15
2.3 Laser background.....	16
2.3.1 Noise from background.....	16
2.3.2 Laser background levels and reduction.....	16
2.4 Near-infrared fluorescence detection.....	18
2.5 Conclusions.....	19
Chapter 3 Semiconductor optoelectronic devices.....	20
3.1 Semiconductor bandgap and optical transitions.....	20
3.2 PIN photodetectors.....	23
3.3 Semiconductor lasers.....	25
3.3.1 Basic laser physics.....	25
3.3.2 Distributed Bragg reflectors.....	27
3.3.3 Vertical-cavity surface-emitting lasers.....	30
3.4 Conclusions.....	32
Chapter 4 Sensor design.....	33
4.1 Literature review.....	33
4.2 Novel approach.....	34
4.3 Optical architectures.....	35

4.4	Optoelectronic design.....	38
4.4.1	Integration.....	38
4.4.2	Filter design.....	39
4.5	Conclusions.....	43
Chapter 5	Fabrication.....	44
5.1	Low-noise photodetector fabrication.....	44
5.2	Integrated sensor fabrication.....	46
5.2.1	Epitaxial structure.....	46
5.2.2	Semiconductor processing.....	48
5.3	Conclusions.....	56
Chapter 6	Optoelectronic device characterization.....	57
6.1	Photodetector measurements.....	57
6.1.1	Electrical measurements.....	57
6.1.2	Optical measurements.....	60
6.2	Optical filter measurements.....	64
6.2.1	Electrical measurements.....	64
6.2.2	Optical measurements.....	64
6.3	VCSEL measurements.....	69
6.3.1	LIV measurements.....	69
6.3.2	Modal and spectral characterization.....	71
6.4	Conclusions.....	75
Chapter 7	Laser background analysis.....	76
7.1	Sources of laser background.....	76
7.2	Direct incidence of spontaneous emission.....	77
7.2.1	Characterization.....	77
7.2.2	Metal blocking walls.....	81
7.3	Laser background from reflections.....	83
7.3.1	Introduction.....	83
7.3.2	Characterization.....	84
7.4	Conclusions.....	88
Chapter 8	Sensitivity.....	89
8.1	Sensitivity in microarray format.....	89
8.1.1	Experimental setup.....	89
8.1.2	Measurement of sensitivity.....	90
8.1.3	Discussion.....	92

8.2	Sensitivity in microfluidic format.....	93
8.2.1	Sensor architecture and experimental setup.....	93
8.2.2	Sensitivity measurement.....	97
8.2.3	Comparison to theory and simulation.....	99
8.2.4	Discussion.....	100
8.3	Improving sensor sensitivity.....	102
8.4	Conclusions.....	103
Chapter 9 Summary and future work.....		104
9.1	Summary.....	104
9.2	Future work.....	105
9.2.1	Laser background reduction.....	105
9.2.2	Optical system design.....	106
9.2.3	Applications.....	107
Appendix A Epitaxial structures.....		108
A.1	Low-noise photodetector (wafer P222).....	108
A.2	Integrated sensor (wafer P763-5).....	108
Appendix B Processing recipes.....		111
B.1	Electrical contacts.....	111
B.1.1	Lithography for 1.5 μ m film bilayer liftoff process.....	111
B.1.2	Lithography for 3 μ m film bilayer liftoff process.....	112
B.1.3	Metal deposition for P-contact and liftoff.....	112
B.1.4	Metal deposition for N-contact and liftoff.....	112
B.1.5	Thermal annealing.....	113
B.2	Etching.....	113
B.2.1	Lithography for 2 μ m resist etch mask.....	113
B.2.2	Lithography for 7 μ m resist etch mask.....	114
B.2.3	Mesa dry etching.....	114
B.2.4	Wet etch sequence for intracavity contact.....	114
B.3	Oxidation.....	115
B.4	Via and metal block formation.....	115
B.4.1	Lithography for resist microstructures.....	115
B.4.2	Oven cure.....	116
B.4.3	Lithography for 7 μ m film bilayer liftoff process.....	116
B.4.4	Metalization for via and metal block.....	116
Bibliography.....		117

LIST OF TABLES

Table 6.1. Typical VCSEL operational parameters for oxide diameters of $a = 4, 7, 14$ and $20\mu\text{m}$. Data collected from sensor samples (P763-5).....	70
Table 8.1. Important sensing parameters used to calculate the theoretical sensor response. These parameters are determined in the characterization presented in this thesis (See Sections 6.1, 6.2 and 8.1).....	99

LIST OF FIGURES

Fig. 1.1. Schematic of hypothetical μ TAS. Microfluidic channels, sample reaction chambers, particulate filters and fluorescence sensing can be integrated and used to perform biological analysis for diagnostic purposes or scientific research.....	2
Fig. 1.2. Schematic of typical analytical analysis based on spatial separation. (Left) Example of capillary electrophoresis (CE). Molecules are separated based on their charge-to-mass ratio. (Right) Example of microarray technology. Molecules are separated based on their binding properties to immobilized probes.....	3
Fig. 1.3. Example measurements from CE and microarray experiments. (Left) Schematic of CE readout. Peak vs. time signature allows readout of spatial distribution of separated molecules. (Right): Schematic readout of microarray experiment. The two dimensional spot pattern identifies binding properties.....	3
Fig. 2.1. Modified Jablonski diagram. The diagram illustrates the electronic levels of fluorescent molecules and the process of absorption, fluorescence and phosphorescence..	9
Fig. 2.2. Measured absorption and emission spectra of IR-800 (LI-COR, Inc.) in methanol. Measurement is conducted with a UV/VIS/NIR spectrophotometer (Perkin Elmer-Lambda 19) and fluorimeter (Instruments S.A.- FluoroMax-2).....	10
Fig. 2.3. Illustration of LIF system and operation. The lens is used to focus the laser beam (solid line) and collect the emitted photons (dashed line) from the fluorescent molecules. The filter is used to block the reflected and scattered laser light from reaching the photodetector.....	12
Fig. 2.4. Spectral regions of autofluorescence for biological molecules and typical fluorescent markers. After [30].....	18
Fig. 3.1. Electronic energy-level diagram of semiconductor material. The difference between the conduction band edge, E_c , and valence band edge, E_v , is often called the energy bandgap.....	21
Fig. 3.2. Diagram of possible optical transitions in a semiconductor material. The processes of absorption, spontaneous emission and stimulated emission are three possible ways in which light can interact with semiconductors.....	22
Fig. 3.3. Diagram of PIN photodetector operation. Photon is absorbed in I region, creating an electron-hole pair. The electron-hole pair are separated by the internal electric field and measured as current.....	23
Fig. 3.4. Optical absorption of GaAs. Taken from Palik [42].....	25
Fig. 3.5. Diagram of laser operation. An optical cavity is formed around an optical gain medium. The light is amplified by the optical gain medium and the optical cavity is used for optical feedback. The laser beam output is the finite optical transmission through Mirror 1.....	27

Fig. 3.6. Diagram of DBR. Two alternating materials of optical thickness $\lambda/4$ are used to form a DBR.....	28
Fig. 3.7. Theoretical power reflectivity spectrum from DBR. DBR design is centered on $\lambda = 780\text{nm}$ and composed of 40 alternating pairs of AlAs and $\text{Al}_{0.3}\text{Ga}_{0.7}\text{As}$ layers.....	29
Fig. 3.8. Schematic of VCSEL. Two DBRs surround quantum well (QW) gain region. Electrical contact is made to the PIN diode in order to forward bias the diode and drive the VCSEL.....	30
Fig. 3.9. Diagram of quantum well. A thin (5-10nm) material is placed between two materials of larger bandgap, creating an energy well to which electrons and holes are attracted.....	31
Fig. 4.1. Illustration of ideal sensing system which utilizes state-of-the-art optoelectronic technology, such as VCSELs, photodetectors and optical filters. In addition, CMOS electronics, micro-optics and microfluidics can be easily integrated with the optoelectronic devices to make a complete system. CMOS electronics are not implemented in the sensor presented in this thesis.....	35
Fig. 4.2. Schematic of general system architectures possible with VCSELs: a) Imaging, b) Waveguide, and c) Proximity.....	36
Fig. 4.3. Schematic of optoelectronic design. VCSEL is grown on top of the photodetector. Photodetector uses the bottom N-DBR of the VCSEL as an optical filter. Complete sensor unit is made through one simple modification to a typical VCSEL epitaxial structure.....	39
Fig. 4.4. Theoretical reflectivity of DBR plotted together with absorption and emission characteristics of IR-800 dye on a linear (left) scale. Theoretical transmission of DBR is plotted on a log scale (right).....	40
Fig. 4.5. Theoretical reflectivity from modified DBR design compared with a typical DBR design. The addition of a simple $\lambda/8$ matching layer on top of the DBR significantly improves the pass-band performance of the filter.....	41
Fig. 4.6. Theoretical angular dependence of $\text{Al}_x\text{Ga}_{1-x}\text{As}$ filter for TE and TM modes. Good filtration of OD 4 is maintained up to $\theta = 60^\circ$ at $\lambda = 770\text{nm}$	42
Fig. 5.1. Low-noise PIN photodetectors (Wafer #P222). (Left) Epitaxial design for low-noise detector sample. See Appendix A.1 for exact epitaxial structure. (Right) SEM image of processed mesa photodetectors.....	45
Fig. 5.2. Epitaxial structure for integrated sensor. The VCSEL is grown on top of the photodetector by MOCVD. See Appendix A.2 for exact structure.....	47
Fig. 5.3. SEM images of the sensor epitaxial structure. (Left) Complete epitaxial structure. (Right) Close-up image of cavity and current spreading layer.....	47
Fig. 5.4. SEM images of processed sensors. (Left) Complete sensor unit in a proximity architecture. (Right) Close-up image of VCSEL showing via formations and metal blocking layers.....	48

Fig. 5.5. Schematic of semiconductor processing sequence used to realize sensor. See Appendix B for detailed processing recipes.....	49
Fig. 5.6. Measured reflectivity profile during dry etching of sensor (P763-5). Image shows reflectivity etch profile through the cavity region; whereas, during processing of the sample, the etch is stopped as marked on the profile.....	51
Fig. 5.7. Schematic of selective wet-etch sequence used to land on 10nm GaAs contact layer. Two selective etches are used in the process: 1) Citric acid-based selective etch and 2) BOE-based selective etch.....	52
Fig. 5.8. SEM image of epitaxial layers protruding from mesa edge after selective wet etching. These protrusions must be considered when designing the intracavity contact mask.....	53
Fig. 5.9. SEM image of VCSEL cross-section and via formation. Cured photoresist microstructures provide excellent platforms for vias and metal blocking structures. A via can be seen making contact to the top mesa contact of the VCSEL.....	55
Fig. 6.1. Dark current measured as a function of detector diameter at a detector reverse bias of 5V. Measurements are conducted on low-noise photodetector samples (P222).....	58
Fig. 6.2. Background current of photodetector at 0V bias. At 5V, the detector shows much greater dark current of 2nA. Measurement is conducted on low-noise photodetector samples (P222).....	59
Fig. 6.3. Schematic of experimental setup used to measure the optical characteristics of the photodetectors and optical filters. An optical beam from tunable Ti:Sapphire laser is focused onto the detector/filter.....	60
Fig. 6.4. Measured and simulated responsivity of photodetector/filter module (P763-5). Simulation is performed by assuming the photodetector has a QE = 100% over the entire spectral range.....	61
Fig. 6.5. Measured responsivity of photodetector/filter module at 0, 3, and 5V reverse bias. This measurement is conducted on low-noise photodetector sample (P222).....	62
Fig. 6.6. Measurement of photodetector linearity. Measurement is conducted at $\lambda = 810\text{nm}$ and on the low-noise photodetector sample (P222).....	63
Fig. 6.7. Theoretical and measured transmission spectrum of sensor filter and low-noise photodetector. This measurement is conducted on the sensor sample (P763-5) and low-noise photodetector sample (P222).....	65
Fig. 6.8. Illustration of three possible mechanisms that degrade filter performance: 1) Filter fluorescence, 2) Optical scattering and 3) Carrier diffusion.....	66
Fig. 6.9. Measured filter transmission spectrum in combination with measured fluorescence spectrum of IR-800 dye (LI-COR Inc.) in methanol. Filter measurement is conducted on sensor sample (P763-5).....	68

Fig. 6.10. CW LIV characteristics of 773nm VCSELs with oxide apertures of 4, 7, 14 and 20 μ m. The current-voltage (IV) curve is shown for the 20 μ m aperture VCSEL. Data is collected from the sensor samples (P763-5).....	69
Fig. 6.11. Near-field optical images of single-mode and multimode VCSELs. (Left) Single mode VCSEL with oxide aperture of $a = 4\mu\text{m}$ and $I_{\text{drive}} = 4*I_{\text{th}}$. (Right) Multimode VCSEL with oxide aperture of $a = 14\mu\text{m}$ and $I_{\text{drive}} = 4*I_{\text{th}}$	71
Fig. 6.12. Measured optical spectrum of 14 μ m aperture VCSEL driven at $I_{\text{drive}} = 4*I_{\text{th}}$. The figure shows that the VCSEL lases in one longitudinal mode.....	72
Fig. 6.13. Measured power dependent emission spectrum for a VCSEL with aperture of 14 μ m. The VCSEL transitions from single-mode to multimode operation with increasing input current.....	73
Fig. 6.14. Far-field divergence of 20 μ m aperture VCSEL.....	74
Fig. 7.1. Schematic of the three sources of laser background: 1) Direct spontaneous emission (Internal Source) 2) Indirect spontaneous emission (External) and 3) laser beam reflection (External).....	77
Fig. 7.2. Illustration of how spontaneous emission can directly illuminate the detector active region. Direct illumination avoids the filter and causes an overwhelming laser background.....	78
Fig. 7.3. Near-field optical image of VCSEL emission. Spontaneous emission scatters from the top mesa edges, creating ring shaped patterns.....	78
Fig. 7.4. Measured laser background in a proximity architecture with no optical interface located above the sensor. Corresponding VCSEL L-I characteristics are also provided.....	79
Fig. 7.5. Measured and simulated laser background in an imaging configuration as a function of the distance between the VCSEL and photodetector. Simulation conducted with ASAP.....	80
Fig. 7.6. Schematic of metal blocking layers to prevent spontaneous emission from directly illuminating the photodetector. An improved metal blocking layer is fabricated to eliminate all optical paths between the VCSEL and photodetector.....	82
Fig. 7.7. Measured laser background as a function of laser drive current. Metal blocking layers significantly reduce the laser background from spontaneous emission. Sensor is in a proximity architecture.....	83
Fig. 7.8. Measured laser background as a function of laser drive current. A thin glass coverslip is placed 1mm above the sensor to illustrate the dramatic increase in background due to optical reflections. Sensor architecture is proximity.....	84
Fig. 7.9. Measured laser background as a function of laser drive current with coverslip placed above. The experiment is conducted for two separations (100 μ m and 500 μ m) between the sensor and coverslip.....	85

Fig. 7.10. Measured laser background contribution from spontaneous emission and laser beam reflection as a function of glass separation. Experiment is conducted with uncoated and AR coated slide.....	86
Fig. 7.11. Measured and simulated values of total laser background versus separation distance from uncoated coverslip. Simulation is generated with ASAP (Breault Research Organization).....	87
Fig. 8.1. Schematic of experimental setup used to simulate microarray detection format. IR-800 Dye is spun onto a glass substrate in a PMMA film. The sensor is placed 500 μ m from the glass slide. Detector inner and outer diameters are 200 μ m and 1mm, respectively.....	90
Fig. 8.2. Detection of IR-800 (LI-COR, Inc.) in microarray format. Measurement is conducted with 20 μ m aperture VCSEL at an output power of 2mW.....	91
Fig. 8.3. Schematic of sensor architecture for microfluidic detection. A lens is used to both focus the laser beam into the channel and collect emitted fluorescence. Relevant system dimensions are shown in the figure. Inner and outer detector diameters are 200 μ m and 1mm, respectively.....	93
Fig. 8.4. Schematic of experimental setup used to align components of microfluidic sensor.....	94
Fig. 8.5. Optical images of microfluidic experimental setup illustrated in Fig. 8.4. (Left) Image of GaAs optoelectronic chip packaged in a 32-dip package and inserted into a PCB. (Right) Close-up image of microfluidic setup during sensing experiment.....	94
Fig. 8.6. Optical simulation of laser beam propagation in microfluidic channel. (Left) Geometric sensor model and simulation of laser beam propagation. (Right) Laser spot at the microfluidic channel.....	95
Fig. 8.7. Measured absorption and emission spectra of IR-800 dye in methanol buffer.....	96
Fig. 8.8. Sensor sensitivity measurement in microfluidic format. Sensor response due to IR-800 (LI-COR, Inc.) in methanol under continuous flow (100 μ L/hr.). Laser output power is 1.9mW at a wavelength of 773nm.....	98
Fig. 8.9. Simulation of fluorescence sensing with ASAP. (Left) Geometric ASAP model of sensor with fluorescence signal propagation. (Right) Simulated sensor response together with measurement.....	100
Fig. 8.10. Sensitivity comparison to well known approaches towards integrated fluorescence sensors for microfluidic applications found in the literature [28, 58, 60, 63, 65].....	101

CHAPTER 1

INTRODUCTION

1.1 MINIATURIZED AND TOTAL ANALYSIS SYSTEMS

Miniaturized and total analysis systems (μ TAS) have received much attention from the scientific research community due to their potential application to high throughput biological analysis and portable medical diagnostics. For research applications, μ TAS promises reduced cost through less reagent and sample consumption and increased speed and parallelism for high throughput analysis [1]. In medical diagnostics, μ TAS can provide immediate point-of-care services that could facilitate detection of common diseases, pathogens, and early-stage cancer [2].

Microfabrication technologies have had a tremendous impact on the development of μ TAS. The integration of microfluidic systems (e.g., channels, mixers, pumps, particulate filters, etc.) with chemical processing and analysis (e.g., Polymerase Chain Reaction (PCR), fluorescence-based DNA hybridization assays, capillary electrophoresis (CE), etc.) enables the realization of miniaturized chemical and biological analysis systems [1-7]. Fig. 1.1 shows an illustration of a hypothetical μ TAS. The example implementation involves a sample input chamber for inserting the sample. Then, the sample can be labeled in the reaction chamber for fluorescence detection. Particulate filters can be important for filtering contaminants and collecting the molecules of interest. As discussed below, a variety of analysis techniques, such as CE, chromatography or microarrays, can be used to physically separate and organize the molecules for subsequent identification. Finally, a sensing system must be used to detect the presence of molecules for readout of experimental results.

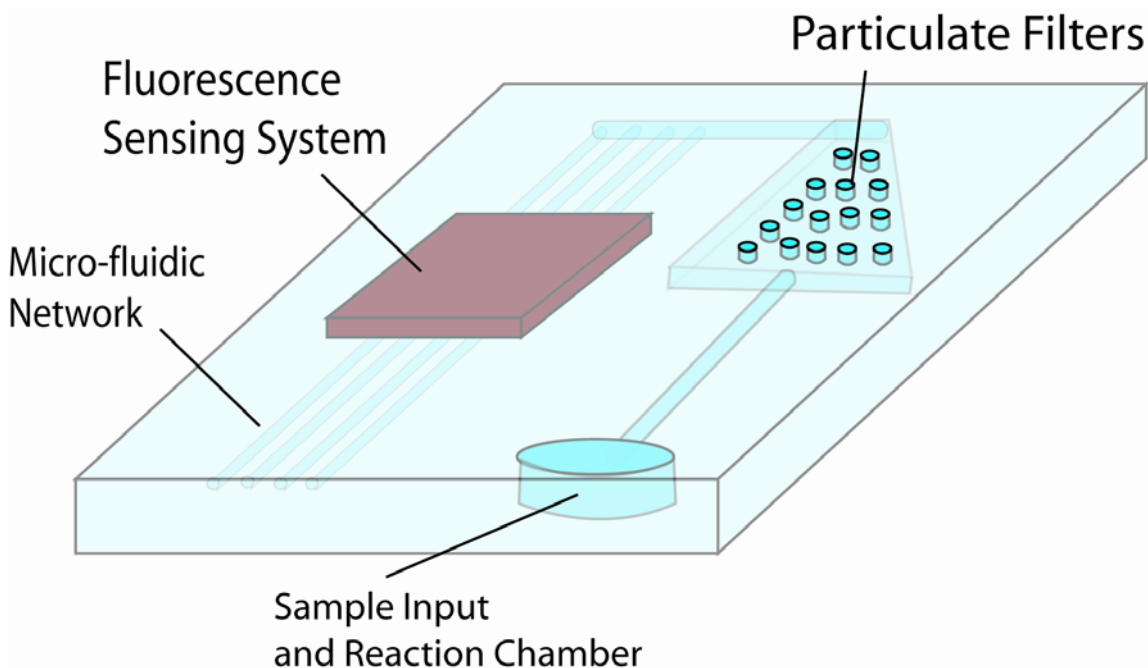


Fig. 1.1. Schematic of hypothetical μ TAS. Microfluidic channels, sample reaction chambers, particulate filters and fluorescence sensing can be integrated and used to perform biological analysis for diagnostic purposes or scientific research.

Much of analytical chemistry and analysis is based on the physical separation of molecules. For example, most of the commonly used analysis techniques, such as CE, chromatography, mass spectroscopy (MS) and microarrays, are all based on physical separation [1,8,9]. The separation is a function of the molecule's properties. This functional dependence allows the experimentalist to determine the molecular type or characteristics based on measurement of the physical separation. Fig. 1.2 shows a general schematic of how CE and microarrays work. CE separates molecules, such as DNA, by applying an electric field in a channel [1]. Different chemical species have different charge-to-mass ratios. Therefore, the molecules move at different speeds in response to an applied electric field and spatial separation is achieved. For microarrays, probe molecules are immobilized on a substrate surface and are used to specifically bind to the molecules of interest [9]. Therefore, the location of binding identifies the molecular species because the probe element location is known.

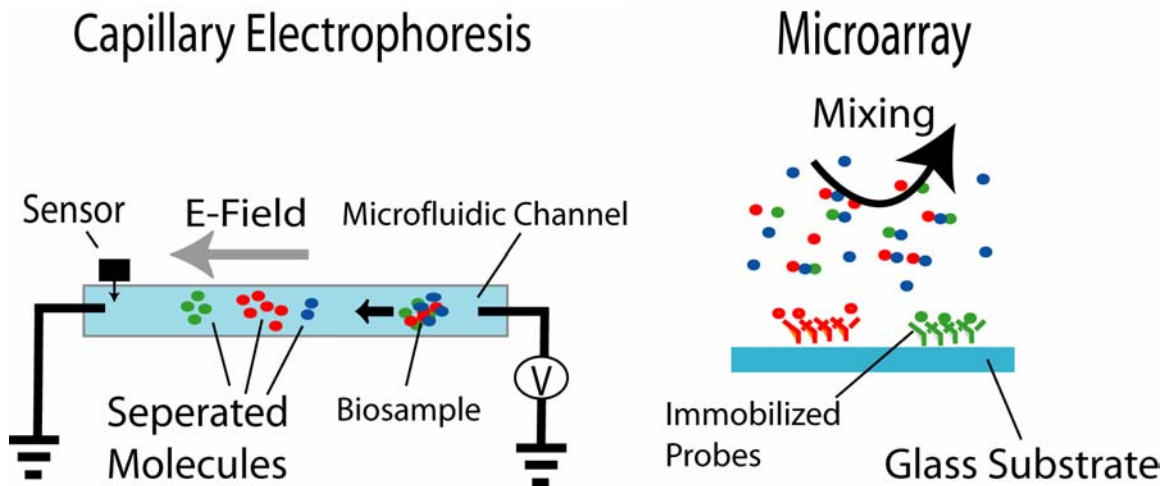


Fig. 1.2. Schematic of typical analytical analysis based on spatial separation. (Left) Example of capillary electrophoresis (CE). Molecules are separated based on their charge-to-mass ratio. (Right) Example of microarray technology. Molecules are separated based on their binding properties to immobilized probes.

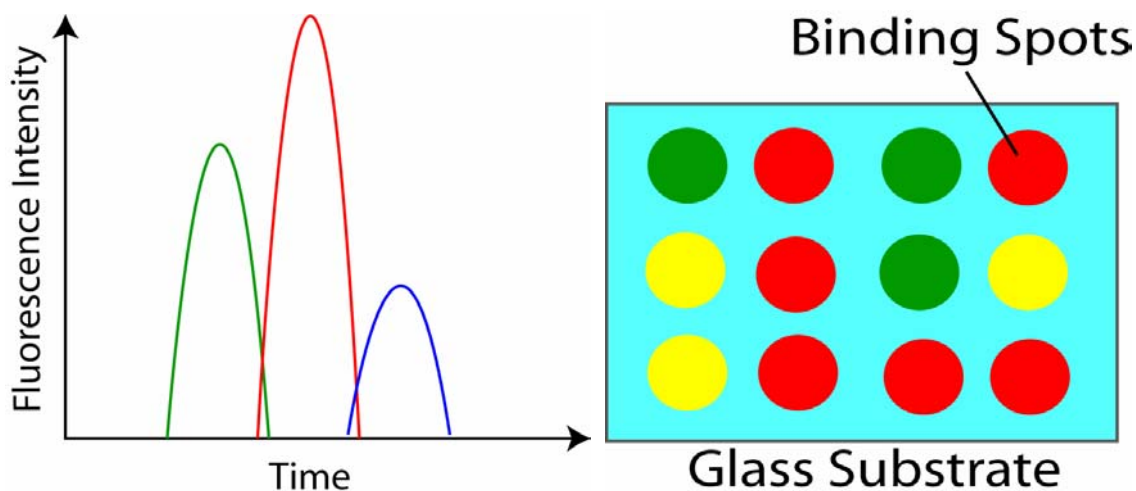


Fig. 1.3. Example measurements from CE and microarray experiments. (Left) Schematic of CE readout. Peak vs. time signature allows readout of spatial distribution of separated molecules. (Right): Schematic readout of microarray experiment. The two dimensional spot pattern identifies binding properties.

1.2 MOLECULAR SENSING

After chemical analysis has taken place, the result must be measured to provide useful information. Usually, this involves sensing for the molecules of interest and measuring the spatial distribution of these interesting molecules. For the CE example shown above, a point sensor can be used to readout the separated molecules by flowing the molecules

under the sensor. In this manner, a peak vs. time signature can be obtained, where the peak is representative of a group of molecules that have similar charge-to-mass ratios, see Fig. 1.3. In the microarray example, the immobilized molecules are measured after binding, yielding a two-dimensional spot pattern that identifies the molecule's binding properties, see Fig. 1.3.

A variety of sensing schemes have been developed to detect the presence of molecules and/or their properties. Comparing these various techniques is a daunting task due to the number of techniques combined with the number of applications and the fact that the success of each technique can be highly dependent on the application and sample preparation techniques used. Mass spectroscopy, fluorescence labeling, magnetic bead labeling, electrochemical, Raman spectroscopy, interferometry, surface plasmon resonance and optical absorption are the more commonly used methodologies [10-13].

Perhaps the largest challenge facing μ TAS is the analysis of complex samples for medical diagnostics and field-based applications [14,15]. The analysis of complex field samples such as blood, urine or soil is plagued with difficulties such as interference from unwanted molecules and low sample concentration. When analyzing complex field samples, it is difficult to make the detection method specific to the agent of interest and avoid interference from other molecules, which is commonly referred to as achieving specificity. In addition, many relevant biological or chemical agents occur in such low abundance that there is little probability of detecting these molecules with current detection methods and sensitivity [7]. Agent concentration methods, such as PCR amplification, together with exquisite detection sensitivity and specificity are needed for the successful implementation of μ TAS in the field.

As discussed above, successful analysis of complex biosamples requires a high degree of specificity and sensitivity. Therefore, a detection technology which is based upon a typical or common molecular property will reduce specificity and sensitivity. For example, developing detection technologies based on mass, electrochemistry, index of refraction, Raman scattering and optical absorption will result in reduced specificity because most molecules have these properties. In addition, signals from unwanted

molecules will create large background signals, which will reduce sensitivity as discussed in Section 2.3. Therefore, much preparation chemistry would be needed to filter out unwanted molecules for analysis systems utilizing these unspecific detection technologies. Sample preparation remains a major technical bottleneck for μ TAS so avoiding sample preparation will help overcome these technical hurdles. Fortunately, external labels are a good way to achieve a high level of specificity and sensitivity in complex molecular environments. The label can be designed to have measurable properties which are not an inherent property of the surrounding biological molecules. For example, many types of molecules do not show significant fluorescence or magnetic properties [16]. Therefore, specially designed fluorescence and magnetic tags can drastically increase sample specificity and sensitivity and reduce the need for sample preprocessing in μ TAS.

1.3 INTEGRATED FLUORESCENCE SENSING

Fluorescence labeling will continue to be a leading technology for μ TAS. Fluorescence sensing offers exquisite sensitivity and specificity [1,17]. In addition, fluorescence labeling is compatible with many commonly used chemical protocols such as PCR, which can increase detection limits and improve specificity.

One technical challenge facing the practical application of μ TAS is the size and expense of conventional fluorescence detection systems. Traditional fluorescence-sensing systems use bulky and discrete elements which are expensive and non-portable. The deployment of such optical systems coupled to μ TAS has been cost-prohibitive and impractical. Integrated fluorescence sensing systems are needed to reduce manufacturing expenses and increase portability, allowing for the mass production and implementation of μ TAS.

The goal of this work is to realize a novel integrated fluorescence sensor for μ TAS applications. The approach used capitalizes on optoelectronic technologies developed for the telecommunication industry. The sensor design monolithically integrates all the

components of a conventional fluorescence sensor (laser, photodetector and emission filter) onto one GaAs substrate. By capitalizing on semiconductor technologies, drastic reductions in cost and increased parallelism can be leveraged to open up new applications. For example, cost reductions may allow for a disposable fluorescence sensor, which would be important for portable diagnostic settings. For basic research, sensor units could be made in parallel to allow for large gains in experimental throughput.

1.4 OUTLINE

The following two chapters are provided to give the reader sufficient background to enable understanding of the sensor operation. Chapter 2, entitled “Laser-Induced Fluorescence Sensing”, discusses the physics of fluorescence sensing and general methodology. The chapter also covers the advantages of fluorescence sensing in the near-infrared (NIR) regime, where the integrated sensor is designed to operate. Chapter 3, entitled “Semiconductor Optoelectronic Devices”, gives a brief overview of the basic physics of semiconductor optoelectronics and operation of the optoelectronic devices used in the sensor: vertical-cavity surface-emitting laser (VCSEL), PIN photodetector and distributed Bragg reflector (DBR).

Chapter 4, entitled “Sensor Design”, describes the general optoelectronic design of the integrated fluorescence sensor and discusses design advantages. The design monolithically integrates a VCSEL, PIN photodetector and DBR optical filter to form a complete fluorescence sensor. In addition, other approaches towards integrated fluorescence sensors are reviewed and compared to the design used in this work. Chapter 5, entitled “Fabrication”, details the fabrication of the sensors. More specifically, the exact epitaxial structure is provided in addition to the semiconductor processing steps required to realize the sensors. Appendices A and B are referenced throughout Chapter 5 to provide more fabrication details.

The final chapters of the thesis provide a complete characterization of the sensor. Chapter 6, entitled “Optoelectronic Device Characterization”, characterizes the individual

components of the sensor: VCSEL, PIN Photodetector and DBR optical filter. Then, Chapter 7, entitled “Laser Background Analysis”, describes the interaction of these components in the context of how this interaction causes laser background, which limits the sensor sensitivity. Chapter 8, entitled “Sensitivity”, characterizes the sensor sensitivity in a microarray and microfluidic format and shows how these sensors can be used towards practical applications. Finally, the thesis is concluded with Chapter 9, “Summary and Future Work”, which summarizes the thesis and proposes future directions for this research.

CHAPTER 2

LASER-INDUCED FLUORESCENCE DETECTION

Due its superior sensitivity and selectivity, laser-induced fluorescence (LIF) detection is a preferred detection technique in analytical chemistry and miniaturized and total analysis systems (μ TAS). The integrated sensor developed in this work capitalizes on LIF to perform molecular sensing. Therefore, this chapter is provided for general background into the physics of fluorescence and engineering design of LIF detection systems.

2.1 BASIC PHYSICS OF FLUORESCENCE

Fluorescence is a well understood process and many sources are available that provide a detailed explanation of the physics of fluorescence [18-20]. A brief explanation is provided here. Fig. 2.1 illustrates the basic physics of fluorescence and is known as a Jablonski diagram. A molecule can be excited into a higher energy state by the absorption of incident radiation. This is usually viewed as a valence electron of the molecule in the ground level (G) being excited by a photon into a higher energy state (S2). After a given period of time, the electron will relax back into the energetically favorable ground state. Fluorescence is one possible relaxation mechanism as well as phosphorescence and non-radiative recombination. During fluorescence, a molecule relaxes into the singlet S1 state and finally emits a fluorescence photon at a slightly lower energy than the absorbed photon energy. The energy difference between the absorbed (S2) and emitted (S1) radiation is defined as the Stokes' shift and is caused by energy loss through molecular relaxation.

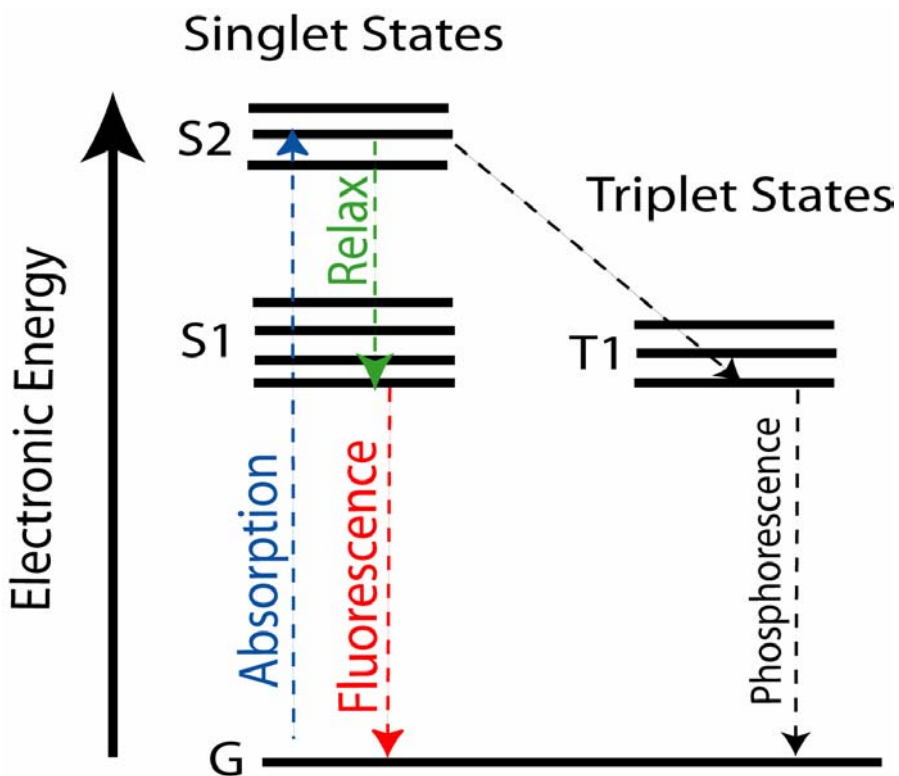


Fig. 2.1. Modified Jablonski diagram. The diagram illustrates the electronic levels of fluorescent molecules and the process of absorption, fluorescence and phosphorescence.

Fluorescent molecules have characteristic absorption and emission spectra. The relationship between the wavelength and energy of a photon is given by

$$\lambda = \frac{hc}{E_{ph}}, \quad (2.1)$$

where λ is the wavelength of the photon, h is Planck's constant (6.63×10^{-34} J s), c is the velocity of light in vacuum (2.998×10^8 m s⁻¹) and E_{ph} is the energy of the photon. As deduced from Eqn. 2.1, the fluorescence emission shifts to longer wavelengths with respect to the absorption spectrum due to the Stokes' shift. Fig. 2.2 shows the measured absorption and emission spectra for IR-800 (LI-COR, Inc.) dye in methanol. The absorption lines are relatively broad due to phonon broadening of the excited states, S1 and S2, see Fig. 2.1. In other words, there are multiple pathways available for fluorescence relaxation, which create a distribution rather than narrow absorption or

emission lines. It is also important to note that the absorption and emission spectra are unique to each fluorescent molecule. Some molecules can fluoresce in the near-infrared (NIR) part of the spectrum as shown in Fig. 2.2, whereas other molecules fluoresce in the visible spectrum [21,22]. From Fig. 2.2, the measured Stokes' shift of IR-800 in methanol is about 18nm. However, the Stokes' shift can vary widely for different fluorescent molecules and range from about 10 – 250nm [22].

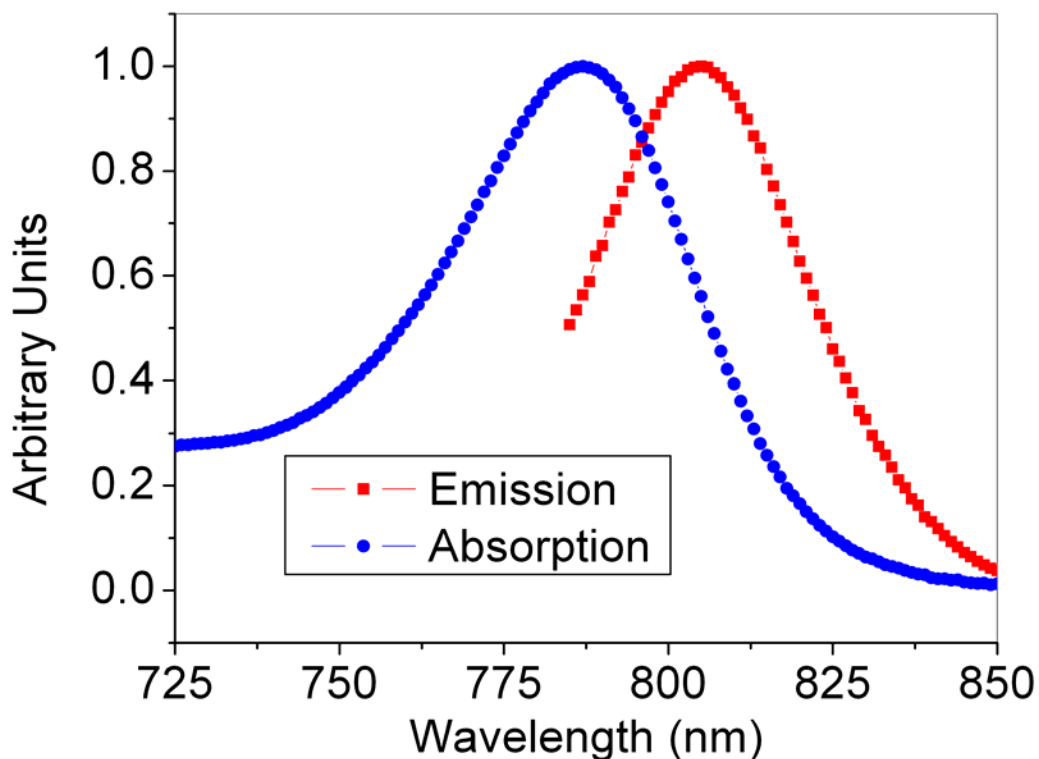


Fig. 2.2. Measured absorption and emission spectra of IR-800 (LI-COR, Inc.) in methanol. Measurement is conducted with a UV/VIS/NIR spectrophotometer (Perkin Elmer-Lambda 19) and fluorimeter (Instruments S.A.- FluoroMax-2).

The brightness of a fluorescent molecule is another important property. Brightness represents how much fluorescence is emitted from a molecule for a given amount of incident radiation. The brightness is proportional to the product of the molar absorptivity, ϵ , and the quantum efficiency, ϕ_{Dye} ,

$$Brightness \propto \epsilon \phi_{Dye}. \quad (2.2)$$

The molar absorptivity coefficient represents the probability of absorption of incident radiation. Typical fluorescent labels have molar absorptivity ranging from 40,000 to 300,000 $M^{-1} \text{ cm}^{-1}$ [21,22]. ϕ_{Dye} is defined as the number of photons emitted divided by the number of photons absorbed. Typical quantum efficiencies of designed fluorescent labels are in the range of 0.1 - 0.9 [21,22]. High quantum efficiency is desirable but less than 1 due to competing relaxation mechanisms.

Besides the spectral characteristics and brightness, fluorescent molecules have other properties that must be considered when designing sensing systems. Assuming the molecules are randomly aligned, the fluorescence signal is emitted isotropically, irrespective of the direction of incident radiation. This has important consequences when considering how to collect the emitted fluorescence with a lens as discussed below in Section 2.2.3. The fluorescent lifetime or characteristic relaxation time from the excited state (S2) to the ground state is another important property. For some of the more commonly used fluorescent labels, fluorescence lifetimes range from 100 ps to 100 ns [21,22].

For many molecules of interest, the fluorescence emission is weak and difficult to measure. Therefore, fluorescent labels are often attached to molecules for detection. Elaborate chemical protocols with high labeling specificity have been developed for a variety of applications. It is possible to label specific molecules in highly complex samples. Often, different types of fluorescent labels are used for spectral and lifetime multiplexing, allowing for the detection of multiple species simultaneously [21-23].

2.2 EXCITATION AND FLUORESCENCE SIGNAL

2.2.1 BASIC DESCRIPTION OF LIF SYSTEM

LIF detection is one of the most commonly used methodologies for biological and chemical analysis systems. Many references offering a detailed description of LIF systems can be found in the literature [19,20,24,25]. A brief description is provided here as background.

Lasers offer significant advantages in the excitation of fluorescent molecules. The high amount of optical power in a narrow spectral line simplifies the use of optical filters and increases fluorescence signal. Fig. 2.3 illustrates how LIF detection works. The laser is used to excite the fluorescent molecules, and the resulting fluorescence signal is collected by the lens and directed onto the photodetector and measured. An optical filter blocks the reflected and scattered laser light from reaching the photodetector because the laser light will cause an overwhelming background, often called laser background, and reduce sensitivity to the smaller fluorescence signals.

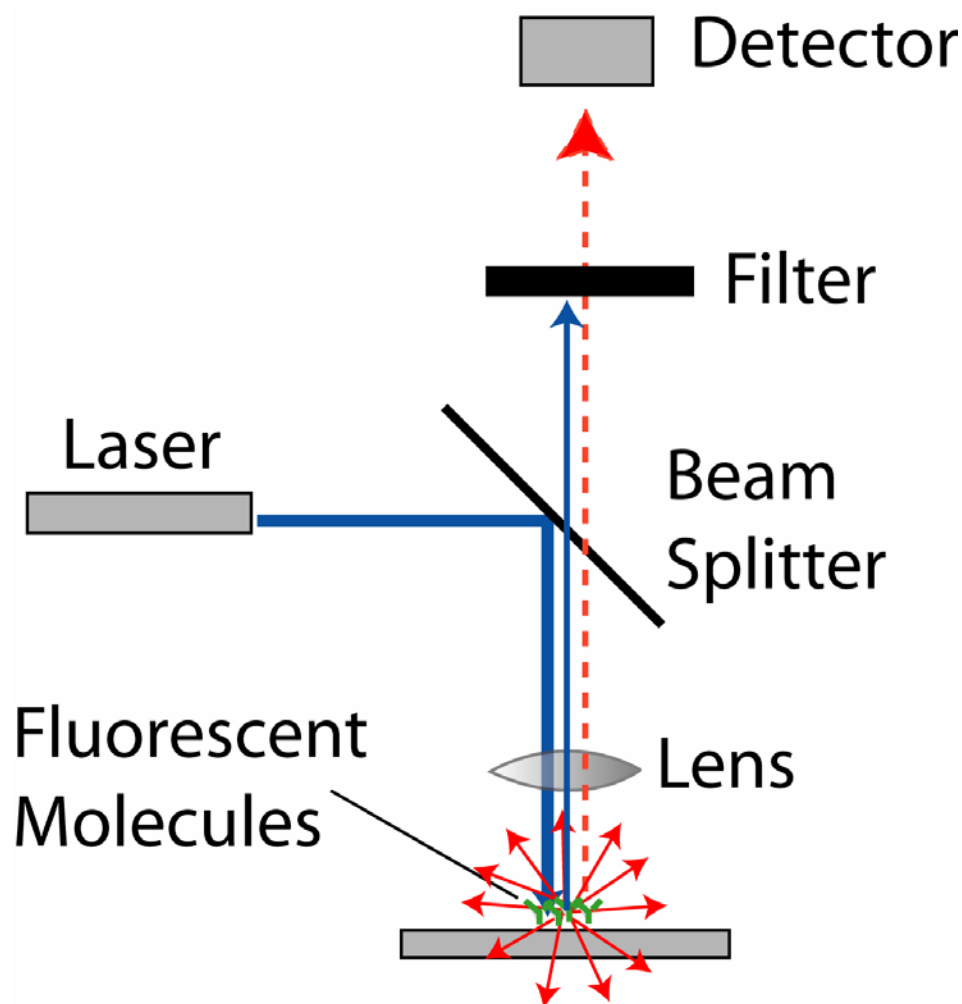


Fig. 2.3. Illustration of LIF system and operation. The lens is used to focus the laser beam (solid line) and collect the emitted photons (dashed line) from the fluorescent molecules. The filter is used to block the reflected and scattered laser light from reaching the photodetector.

2.2.2 ABSORPTION OF THE EXCITATION LIGHT

The Lambert-Beer law is typically used to calculate the amount of absorbed excitation light by a given volume concentration, c , of fluorescent molecules [26]. The Lambert-Beer law is given by the following equation,

$$A = \log \frac{I_o}{I_T} = \log \frac{P_o}{P_T} = \varepsilon lc, \quad (2.3)$$

where I_o and P_o are the excitation intensity and power, I_T and P_T are the transmitted intensity and power, ε is the molar absorptivity, c is the molecular concentration and l is the path length through the sample.

It is desirable to solve for the absorbed laser power, P_A , from Eqn. 2.3. Due to the conservation of energy, the amount of absorbed power is given by the simple equation

$$P_A = P_o - P_T. \quad (2.4)$$

Combining Eqns. 2.3 and 2.4 and solving for P_A yields the following useful expression

$$P_A = P_o(1 - 10^{-\varepsilon lc}). \quad (2.5)$$

2.2.3 EMITTED FLUORESCENCE AND COLLECTION EFFICIENCY

As stated above, ϕ_{Dye} defines the amount of emitted photons divided by the amount of absorbed photons. Therefore, the amount of emitted fluorescence power, P_F , is simply given by

$$P_F = \phi_{Dye} P_A = \phi_{Dye} P_o(1 - 10^{-\varepsilon lc}). \quad (2.6)$$

As discussed above in Section 2.1, the fluorescence emission is emitted isotropically. For maximum detection sensitivity, the optical system should be designed to collect a significant portion of the emitted fluorescence. The fluorescence collection efficiency of

the optical system, C_F , is defined as the amount of collected fluorescence divided by the total fluorescence emitted. Due to the isotropic emission, it is difficult to collect a significant portion of this fluorescence, as described below.

In most LIF detection systems, a high numerical lens is used to collect the emitted fluorescence. Numerical aperture, NA , is defined by

$$NA = n \sin \theta, \quad (2.7)$$

where θ is the half angle of the lens collection cone and n is the optical index of the material in front of the lens [27].

Qualitatively, it is useful to understand how much fluorescence is collected from a lens of a given numerical aperture. In many fluorescence sensing experiments, the specimen is excited by a focused laser spot and the fluorescence is emitted from this spot. Therefore, the fluorescence source can be modeled as a simple point source emitting isotropically. In this example, the lens collection efficiency is simply equal to the number of steradians the lens collects from divided by the total steradians of a sphere, which is 4π . Therefore, the lens collection efficiency is given by

$$C_F = \frac{1 - \cos \theta}{2}. \quad (2.8)$$

Then, by combining Eqns. 2.7 and 2.8, an equation for C_F as a function of NA results,

$$C_F = \frac{1 - \sqrt{1 - \frac{NA^2}{n^2}}}{2}. \quad (2.9)$$

Even for an objective with an unusually high $NA = 0.9$, Eqn. 2.9 predicts a C_F equal to only 0.1 for detection in a buffer with $n = 1.5$. In other words, only 10% of the fluorescence signal is collected. Typical values of NA range from 0.3 – 0.8 and result in collection efficiencies from 0.01 – 0.1. The small fraction of emitted fluorescence that is

collected continues to be a challenge for most systems for the detection of small concentrations of fluorescent molecules.

Beside the fluorescence collection efficiency of the lens, the amount of fluorescence signal transmitted through the optical filter is another important design parameter that determines the total fluorescence collection efficiency of the system. Optical filters have characteristic transmission spectra and may reject a significant portion of the fluorescence signal if not properly designed. The filter transmission and fluorescence spectra both determine how much fluorescence is transmitted, T_F , through the filter. T_F can be calculated by

$$T_F = \frac{\int T(\lambda) \cdot F(\lambda) d\lambda}{\int F(\lambda) d\lambda}, \quad (2.10)$$

where $T(\lambda)$ is the filter transmission spectrum and $F(\lambda)$ is the fluorescence emission spectrum.

Finally, the amount of fluorescence power reaching the detector, P_D , is the amount of emitted fluorescence power, P_F , multiplied by the collection factors, C_F and T_F :

$$P_D = T_F C_F P_F = T_F C_F \phi_{Dye} P_o (1 - 10^{-\epsilon l c}). \quad (2.11)$$

2.2.4 DETECTOR SIGNAL FROM FLUORESCENCE

It is useful to solve for the photodetector current response due to the fluorescence signal reaching the photodetector, P_D . The first step involves converting the incident power into the number of photons reaching the detector per unit time. Eqn. 2.1 gives the relationship between photon energy and wavelength. By dividing the incident power by the photon energy, the number of photons per unit time, N_{ph} , reaching the detector is

$$N_{ph} = \frac{P_D}{E_{ph}} = \frac{\lambda}{hc} T_F C_F \phi_{Dye} P_o (1 - 10^{-\epsilon l c}). \quad (2.12)$$

The quantum efficiency of the photodetector, ϕ_{Det} , is defined as the number of electrons detected divided by the number of incident photons. Therefore, an equation for the amount of detected current from fluorescence, I_F , can be simply found by multiplying Eqn. 2.12 by ϕ_{Det} and q ,

$$I_F = q\phi_{Det}N_{ph} = q\frac{\lambda}{hc}T_F C_F \phi_{Det} \phi_{Dye} P_o (1 - 10^{-\epsilon l c}), \quad (2.13)$$

where q is the amount of charge per electron, -1.602×10^{-19} C.

2.3 LASER BACKGROUND

2.3.1 NOISE FROM BACKGROUND

Background current at the photodetector is a source of noise and determines the noise floor in most fluorescence sensing applications. In fluorescence sensing, there are several possible sources of background detector current, including photodetector dark current, detected laser light and fluorescence from unwanted molecules [20]. The dominant source of background depends on the application and instrumentation. As discussed throughout this work, laser background typically dominates integrated sensors due to the difficulties of achieving high spectral and spatial filtration. Shot noise is the fundamental noise limit that results from laser background [25]. However, random variations in laser background from optical misalignment, mechanical vibrations and laser power fluctuations typically dominate the noise characteristics [28]. Typically, in most fluorescence sensing applications, it is a challenge to detect signals below 1% of the direct current (DC) background level.

2.3.2 LASER BACKGROUND LEVELS AND REDUCTION

Laser background is a major challenge because typical fluorescence signals are many orders of magnitude less than the laser power. As a result, if only a small fraction of the laser emission is detected, then an overwhelming background at the photodetector will be

present and drastically reduce sensitivity to the smaller fluorescence signals. Therefore, laser background must be reduced by employing optical filters and spatial filtration [29].

A qualitative understanding of the challenge to overcome laser background can be obtained by analyzing the ratio of fluorescence signal to laser excitation power. The ratio can be found by dividing Eqn. 2.11 by the incident laser power,

$$\frac{P_D}{P_o} = T_F C_F \phi_{Dye} (1 - 10^{-\epsilon l c}). \quad (2.14)$$

It is useful to plug in some typical values for microfluidic sensing to solve for the ratio of fluorescence signal to laser power: $T_F = 0.8$, $C_F = 0.05$, $\phi_{Dye} = 0.15$, $\epsilon = 270,000 \text{ M}^{-1}\text{cm}^{-1}$, $l = 50\mu\text{m}$ and $c = 1\text{nM}$. Using these values, it is found that the ratio is 1.9×10^{-8} . In other words, the signal from the fluorescence is nearly 8 orders of magnitude lower than the laser power.

From the above analysis, it is obvious that methods must be employed to reject the laser light from being detected or the laser will create an enormous background relative to the fluorescence signal. In conventional fluorescence sensing schemes, optical filters are used to spectrally filter the laser light, see Fig. 2.3. Due to the close spacing between the absorption and emission spectra of most commonly used fluorescent molecules, achieving high spectral filtration can be a challenge. Typically, interferometric-based filters are used; however, these are typically employed in collimated detection configurations due to the angular dependence of these filters and tight spacing between dye absorption and emission. For collimated detection configurations, filters can be made to have greater than 10^5 rejection or optical density (OD) 5. Obtaining spectral filtration above OD 5 can be difficult and expensive. Additional methods are typically used to further reduce laser background. Optical systems must be designed such that the reflected and scattered light does not illuminate the detector. This type of filtration is called spatial filtration. Conventional fluorimeters collect fluorescence light at 90° to the incident excitation beam to achieve a high degree of spatial filtration. The amount of spatial filtration that can be achieved varies widely and depends on the optical scattering

characteristics of the materials used and the detection geometry. Typically, a system can be designed such that less than 1% of the emitted laser illuminates the filter [29].

2.4 NEAR-INFRARED FLUORESCENCE DETECTION

One serious problem with conventional fluorescence detection in the visible spectrum is autofluorescence. Autofluorescence is defined as intrinsic fluorescence of molecules without fluorescent tags. As illustrated in Fig. 2.4, autofluorescence can be quite significant in the visible spectrum because many types of molecules, such as proteins, found in biological systems fluoresce in this region; whereas, there is relatively low autofluorescence in the near-infrared (NIR) regime [19,30]. As discussed below, large gains in sensitivity and specificity are possible by moving into the NIR to avoid autofluorescence, and many researchers have capitalized on the inherent advantages of this spectral range [30-36].

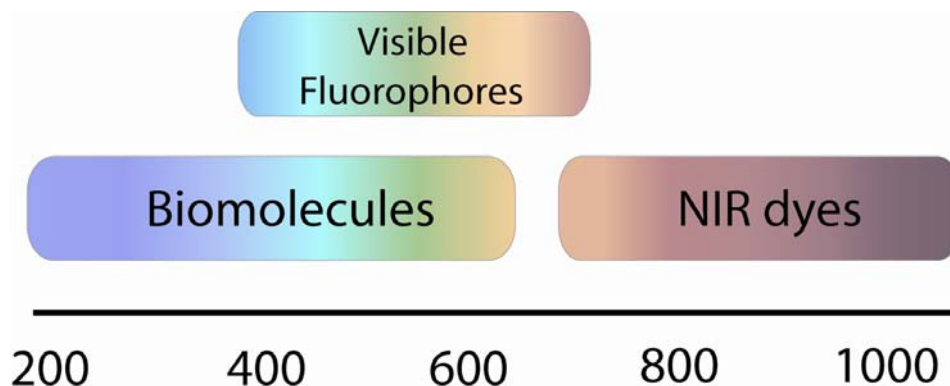


Fig. 2.4. Spectral regions of autofluorescence for biological molecules and typical fluorescent markers. After [30].

As discussed in Section 1.2, maintaining a high degree of specificity and sensitivity is critical for emerging diagnostic applications and the analysis of complex biological fluids. The NIR offers high specificity due to the low autofluorescence in this spectral range [30]. In other words, only the NIR tag fluoresces so the sensing mechanism is specific to the tag and not susceptible to contamination from other molecules or substances. On the other hand, in the visible spectrum, many molecules fluoresce, so information specific to the tag is lost. Another advantage of the NIR is increased

sensitivity. When fluorescence sensing in the visible region, a large background from autofluorescence occurs [19,20,30]. This background will reduce the detection sensitivity as discussed above in Section 2.3.1. In the NIR, one is detecting against a relatively “black” background and sensitivity can be much greater for certain applications. For example, it was found in point-of-care rapid diagnostic assays (Biosite Inc.) that long wavelength dyes (Ex. at 670nm) can be used as fluorescent markers attached to antibodies to increase sensitivity and overcome background fluorescence problems involved with using visible dyes in blood samples [33]. Another advantage of the NIR that is worth noting is lower absorption and scattering within biological tissues. Light in the NIR can penetrate far into tissue and be useful for *in-vivo* imaging and diagnostic purposes [32,35].

Unfortunately, visible fluorescence continues to be the dominant method due to common practice and large availability of dyes in this spectral range. However, researchers and companies have begun to develop acceptable dyes and makers to capitalize on the NIR spectral range [37,38]. As fluorescence sensing and analysis move to more portable diagnostic formats, where the analysis of complex samples is required, the urgency to move into the NIR will become much greater and more markers will be developed to meet this demand.

2.5 CONCLUSIONS

The basic physics of fluorescence is described. Then, relevant equations are derived which form the basis of LIF detection. Important engineering considerations relating to LIF detection are discussed, such as fluorescence collection efficiency and laser background. It is shown that fluorescence signals are much lower than the laser powers used to excite fluorescent molecules, and methods such as spectral and spatial filtration must be used to reduce the amount of laser background. In addition, fluorescence sensing in the NIR offers significant advantages over conventional sensing in the visible due to the low autofluorescence in this spectral range, and NIR sensing will become more important as μ TAS moves towards portable diagnostic settings.

CHAPTER 3

SEMICONDUCTOR

OPTOELECTRONIC DEVICES

Semiconductor optoelectronics is the technological basis for the design and realization of the integrated fluorescence sensor presented in this thesis. Therefore, this chapter provides a general introduction to semiconductor optoelectronic physics and devices so the reader can more thoroughly understand the sensor operation. The devices discussed in this chapter include vertical-cavity surface-emitting lasers (VCSELs), PIN photodetectors and distributed Bragg reflectors (DBRs), which are the major optoelectronic devices used in the integrated fluorescence sensor.

3.1 SEMICONDUCTOR BANDGAP AND OPTICAL TRANSITIONS

Understanding the electronic band structure of semiconductors and optical transitions between bands is essential for understanding semiconductor optoelectronic devices. A brief explanation of this physics is provided here; whereas, the reader can find a much more detailed treatment by S. L. Chuang [39].

Semiconductor materials are typically made from a crystalline lattice of discrete atomic species, such as Silicon (Si) or Gallium Arsenide (GaAs). When located in a tightly spaced crystalline lattice, the discrete electronic transitions typical of individual molecules form an electronic band structure, see Fig. 3.1. Unlike fluorescence or single molecule transitions, the electronic levels in semiconductor crystals are not discrete but continuous bands that extend from energies greater than the conduction band edge ($E > E_c$) and energies less than the valence band edge ($E < E_v$). The forbidden gap between

the conduction and valence band, where no allowable states occur, is often referred to as the energy bandgap.

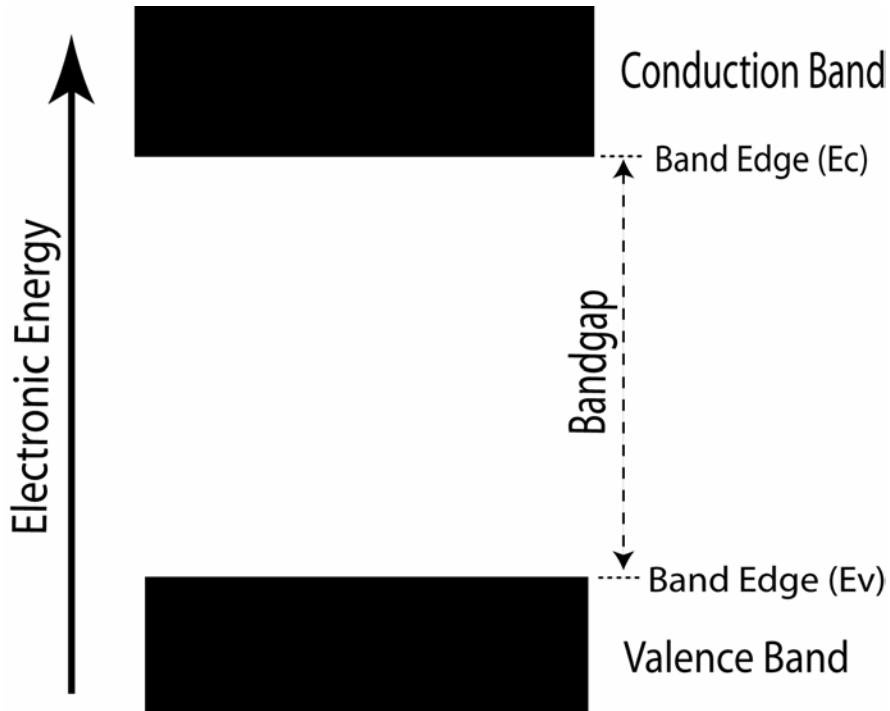


Fig. 3.1. Electronic energy-level diagram of semiconductor material. The difference between the conduction band edge, E_c , and valence band edge, E_v , is often called the energy bandgap.

In the design of the sensor presented in this work, the semiconductor alloy system $\text{Al}_x\text{Ga}_{1-x}\text{As}$ is used. Therefore, it is useful to provide a simplified expression for the direct bandgap of this material system as a function of alloy composition [40],

$$E_g = 1.424 + 1.27x. \quad (3.1)$$

As shown in Fig. 3.2, three types of optical transitions can occur between the valence and conduction bands. In semiconductor physics, it is often convenient to describe the absence of an electron in the valence band as a positively charge particle or hole. If a photon enters the material with an energy, E_{ph} , greater than the bandgap, E_g , then an electron can be excited into the conduction band from the valence band after absorbing the photon. This process is called optical absorption. After absorption, an excited electron is present in the conduction band and an excited hole is present in the valence

band or, in other words, an electron-hole pair has been created. Spontaneous emission occurs when an electron is present in the conduction band and spontaneously recombines with a hole located in the valence band, annihilating the electron-hole pair and creating a photon. The process of stimulated emission is the most complex of the optical processes. Stimulated emission involves a photon interacting with an electron in the conduction band and a hole in the valence band, which causes the electron and hole to recombine and create another photon of equal energy and phase to the incident photon, resulting in two identical photons.

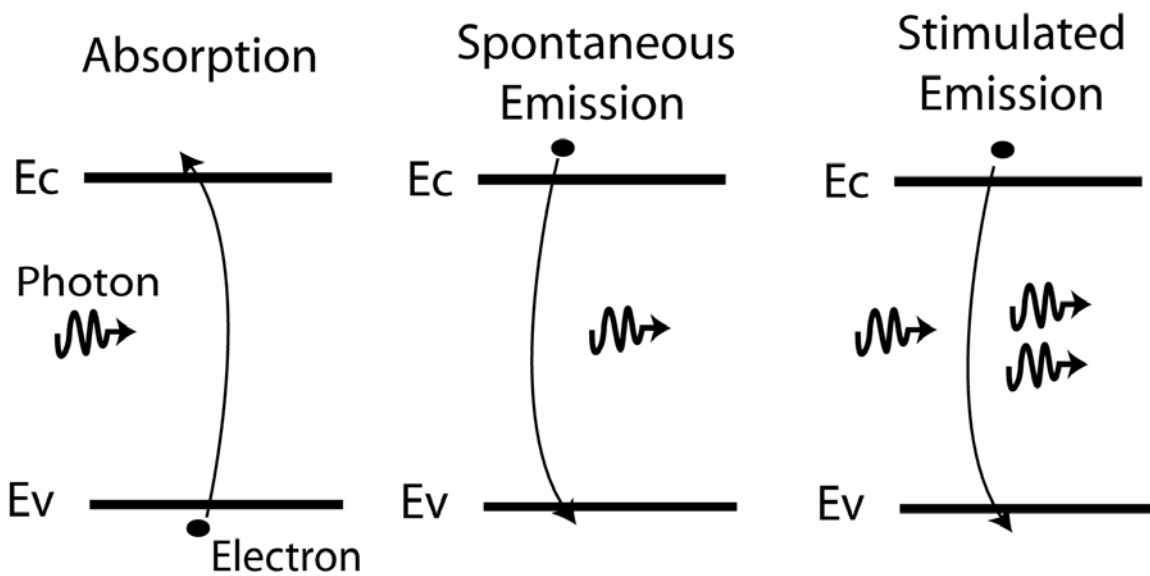


Fig. 3.2. Diagram of possible optical transitions in a semiconductor material. The processes of absorption, spontaneous emission and stimulated emission are three possible ways in which light can interact with semiconductors.

Optical transitions do not occur efficiently or with high probability in some semiconductor materials. When designing optoelectronic devices such as a laser, it is usually desirable to use an optical material where optical transitions are favored. Direct bandgap semiconductors such as GaAs typically favor strong optical interactions; whereas indirect bandgap semiconductors, such as Si, do not. Eqn. 3.1 describes the direct bandgap of $\text{Al}_x\text{Ga}_{1-x}\text{As}$ as a function of alloy composition. It is important to note that $\text{Al}_x\text{Ga}_{1-x}\text{As}$ becomes an indirect bandgap material for alloy compositions greater than approximately 0.4 [40].

3.2 PIN PHOTODETECTORS

In Section 3.1, the simple process of optical absorption is described. PIN Photodetectors capitalize on optical absorption to detect light. As discussed above, after light has been absorbed, an electron-hole pair is created. An applied electric field can be used to separate and transport the electron and hole in opposite directions to create current. This current can be measured external to the detector and allows the detection of the light that is incident on the material.

In PIN photodetectors, the absorbing intrinsic (I) region is placed between N-doped and P-doped semiconductor layers. This causes an internal electric field to develop across the I region when the electron rich material (N) and hole rich material (P) equilibrate by electron and hole diffusion. This internal electric field separates the electron-hole pairs created by absorption and enables the simple readout of current as illustrated in Fig. 3.3. Another advantage of the PIN design is that an external reverse-bias can be simply applied across the diode without increasing the dark current significantly. For a more detailed description of PIN photodetectors, see S. L. Chuang and P. Bhattacharya [39,41].

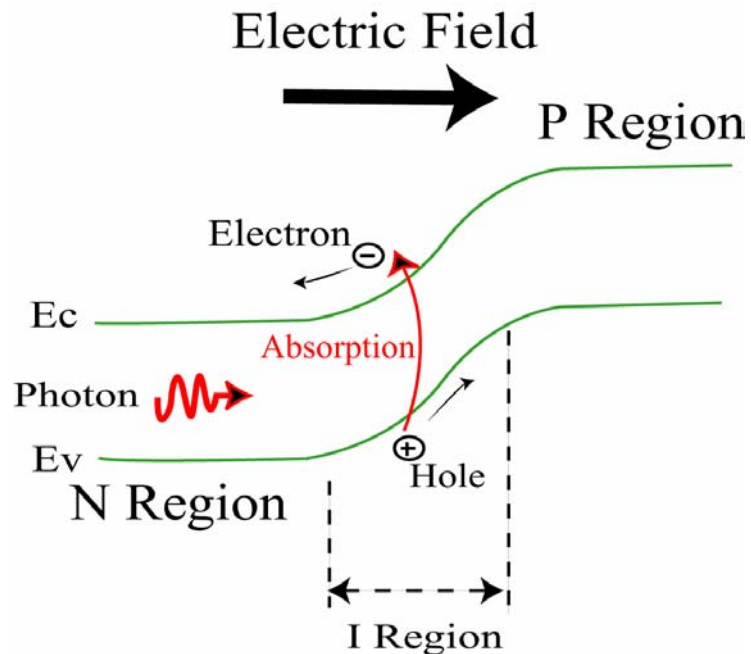


Fig. 3.3. Diagram of PIN photodetector operation. Photon is absorbed in I region, creating an electron-hole pair. The electron-hole pair are separated by the internal electric field and measured as current.

An equation can be derived to calculate the amount of optical absorption occurring in a material. If α is defined as the absorption probability of a photon per unit length, then a simple differential equation can be formed,

$$\frac{dn_p}{dz} = -n_p\alpha, \quad (3.2)$$

where n_p is the number of photons crossing a unit cross-sectional area per unit second. Solving the differential equation yields

$$n_p(z) = n_p(0)e^{-\alpha z}. \quad (3.3)$$

A more useful equation that relates intensity to optical absorption can be inferred from Eqn. 3.3. Since the intensity is proportional to the number of photons crossing a unit area per unit time, then

$$I(z) = I_o e^{-\alpha z}, \quad (3.4)$$

where I_o is the initial intensity at $z = 0$. Following from Eqn. 3.4 and conservation of energy, the fraction of absorbed radiation for a detector with absorbing layer thickness, d , is given by

$$\frac{I_a}{I_o} = 1 - e^{-\alpha d}, \quad (3.5)$$

where I_a is the absorbed intensity.

The absorption coefficient, α , is commonly used when designing photodetectors. For example, it is often desirable to engineer the length of the photodetector to obtain total absorption of incident light. Fig. 3.4 shows the absorption coefficient for GaAs [42]. The bandgap of GaAs is 1.424 eV, which corresponds to a wavelength of 871nm using Eqn. 2.1. In theory, there should be no absorption below the bandgap because there are

no electronic transitions available. However, as seen in Fig. 3.4, there is significant absorption below the bandgap of the material. Absorption effects such as excitons, Urbach tail, free-carrier absorption and material defects can cause significant absorption below the bandgap and must be considered when designing devices [39,43,44]. Above the bandgap, the absorption increases because the density of states in the conduction and valence bands increases with increasing energy. Unless limited by high speed considerations ($>20\text{GHz}$), nearly 100% of the light is absorbed and detector quantum efficiency is generally $> 85\%$.

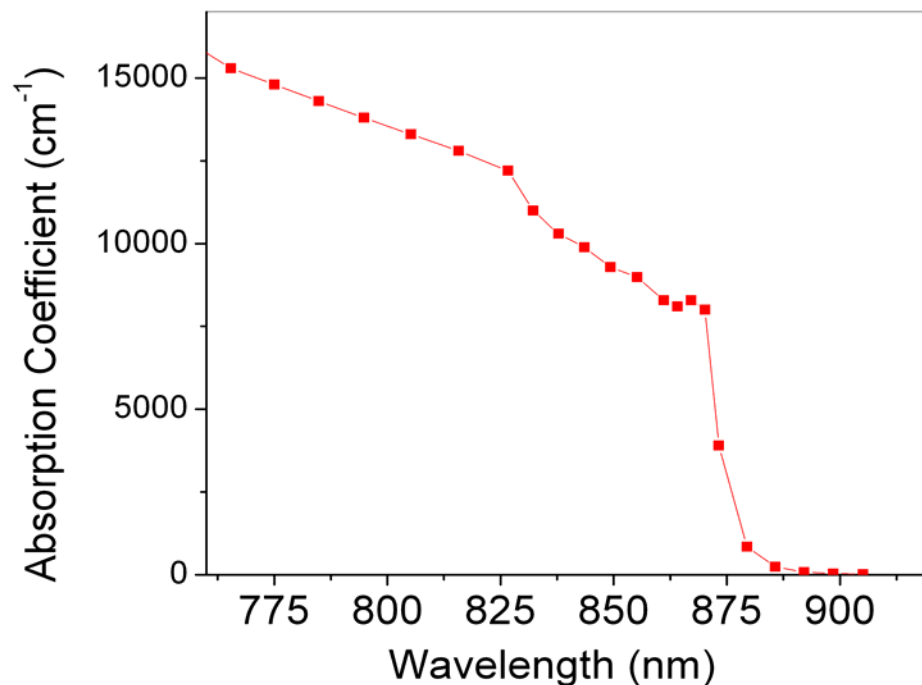


Fig. 3.4. Optical absorption of GaAs. Taken from Palik [42].

3.3 SEMICONDUCTOR LASERS

3.3.1 BASIC LASER PHYSICS

A brief description of laser physics is provided here. A. E. Siegman and Coldren et. al. are excellent sources for a more detailed theory on lasers and semiconductor lasers [45,46].

The inverse process of optical absorption is stimulated emission. An analogous equation to Eqn. 3.4 can be derived for the process of optical gain,

$$I(z) = I_o e^{gz}, \quad (3.6)$$

where g is the gain coefficient of the material. By utilizing stimulated emission, optical gain can be achieved. Fig 3.2 gives an intuitive understanding of how optical gain can be achieved from stimulated emission. During stimulated emission, one photon enters the material to produce an additional photon, resulting in two coherent photons.

Under most conditions, the process of absorption dominates over stimulated emission because there are typically a much greater number of electrons in the valence band than in the conduction band. However, electrical and optical methods can be used to pump electrons into the conduction band and holes into valence band, thereby achieving a greater number of electrons, N_c , in the conduction band than electrons, N_v , in the valence band at a given transition energy. This condition is called population inversion,

$$N_c(E) > N_v(E). \quad (3.7)$$

If population inversion is achieved, then the process of stimulated emission dominates over the process of optical absorption, resulting in net optical gain in the material.

Once optical gain has been achieved, a laser can be formed by placing the optical gain medium inside an optical cavity or between two mirrors to provide optical feedback. Fig 3.5 shows a simple diagram of a laser and illustrates how the mirrors interact with optical gain to create a laser. The gain material in a laser is an optical amplifier. The optical mirrors provide optical feedback for the gain medium. Therefore, an intense circulating optical field develops within the cavity of the laser. The exiting laser beam is the finite loss of the optical field within the cavity due to transmission through Mirror 1.

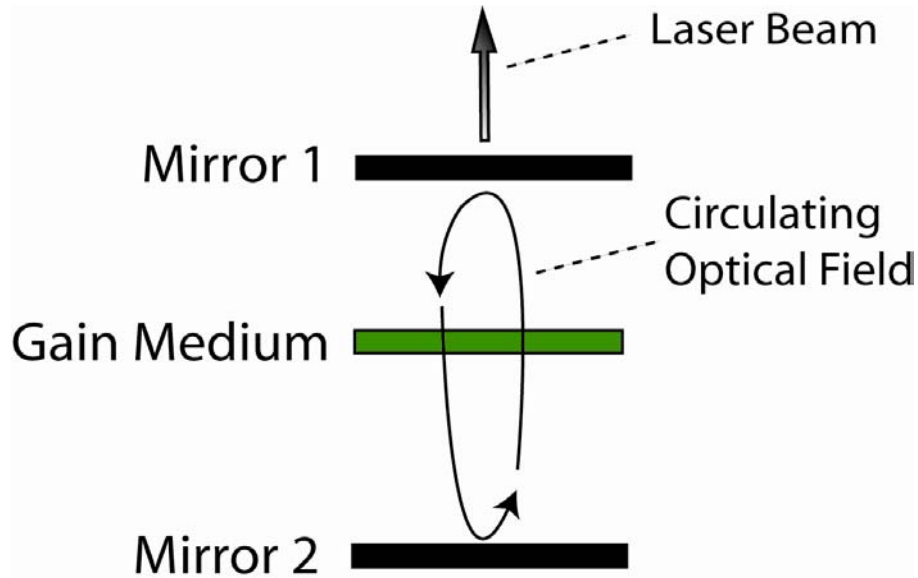


Fig. 3.5. Diagram of laser operation. An optical cavity is formed around an optical gain medium. The light is amplified by the optical gain medium and the optical cavity is used for optical feedback. The laser beam output is the finite optical transmission through Mirror 1.

Another important condition for lasing neglected in the discussion above involves the cavity length. The round trip cavity length must be an integer of the lasing wavelength,

$$L_c = k \frac{\lambda}{2n}, \quad (3.8)$$

where L_c is the cavity length, λ is the lasing wavelength, n is the optical index within the cavity and k is an integer. As the optical field circulates around the cavity of the laser, this phase condition allows the photons to interfere constructively and enables the optical field to build up in intensity.

3.3.2 DISTRIBUTED BRAGG REFLECTORS

Distributed Bragg reflectors (DBRs) are one of the most important elements used to realize vertical-cavity surface-emitting lasers (VCSELs). Also, in the design of the integrated fluorescence sensor, DBRs are used as an effective optical filter. DBRs are typically made of two alternating materials with an optical thickness equal to $\lambda_{\text{Bragg}}/4$, where λ_{Bragg} is called the Bragg wavelength, see Fig. 3.6. At λ_{Bragg} , the reflectance from

each interface of the DBR interferes constructively, which is additive, and results in a large net reflectivity.

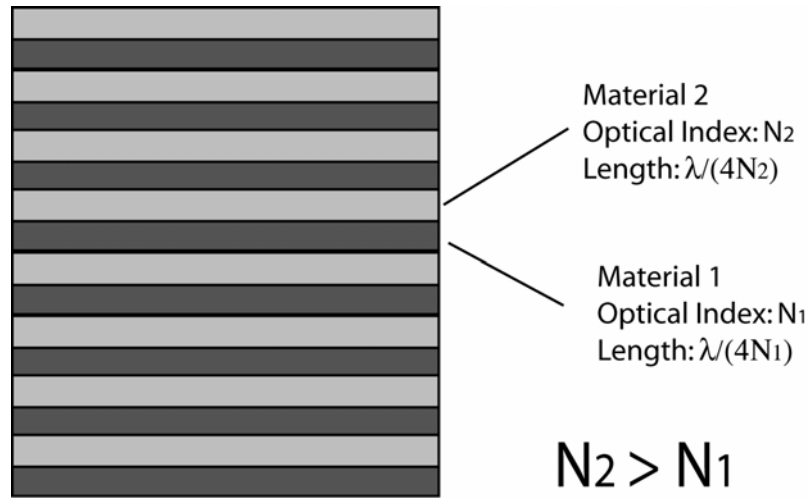


Fig. 3.6. Diagram of DBR. Two alternating materials of optical thickness $\lambda/4$ are used to form a DBR.

From Fresnel's equations for matching the tangential electric fields for a propagating electromagnetic wave at normal incidence, the reflectivity from a single optical interface is given by

$$r = \frac{n_1 - n_2}{n_1 + n_2}, \quad (3.9)$$

where r is the reflectivity of the electric field from a single interface, n_1 and n_2 are the optical indices of the alternating $\lambda_{\text{Bragg}}/4$ material layers. As stated above, the $\lambda_{\text{Bragg}}/4$ optical thickness of the DBR layers causes the reflections from each interface to interfere constructively. The power reflectivity, R , of a DBR with k material pairs at λ_{Bragg} is given by [46]

$$R_{\text{max}} = |r_{\text{max}}|^2 = \left(\frac{1 - \left(\frac{n_1}{n_2}\right)^{2k}}{1 + \left(\frac{n_1}{n_2}\right)^{2k}} \right)^2. \quad (3.10)$$

Typical power reflectance of DBRs used in VCSELs are in the range of 99.9 – 99.999 % [47]. This high reflectance is required to compensate for the small amount of optical gain due to the short cavity length of VCSELs.

Fig. 3.7 shows a power reflectance spectrum for a typical $\text{Al}_x\text{Ga}_{1-x}\text{As}$ DBR used to make VCSELs operating in the near-infrared (NIR). The reflectivity spectrum is generated through a thin film optical simulator based upon a transfer matrix algorithm [48]. The DBR design is centered on $\lambda_{\text{Bragg}} = 780\text{nm}$ with 40-pairs of alternating AlAs and $\text{Al}_{0.3}\text{Ga}_{0.7}\text{As}$ layers.

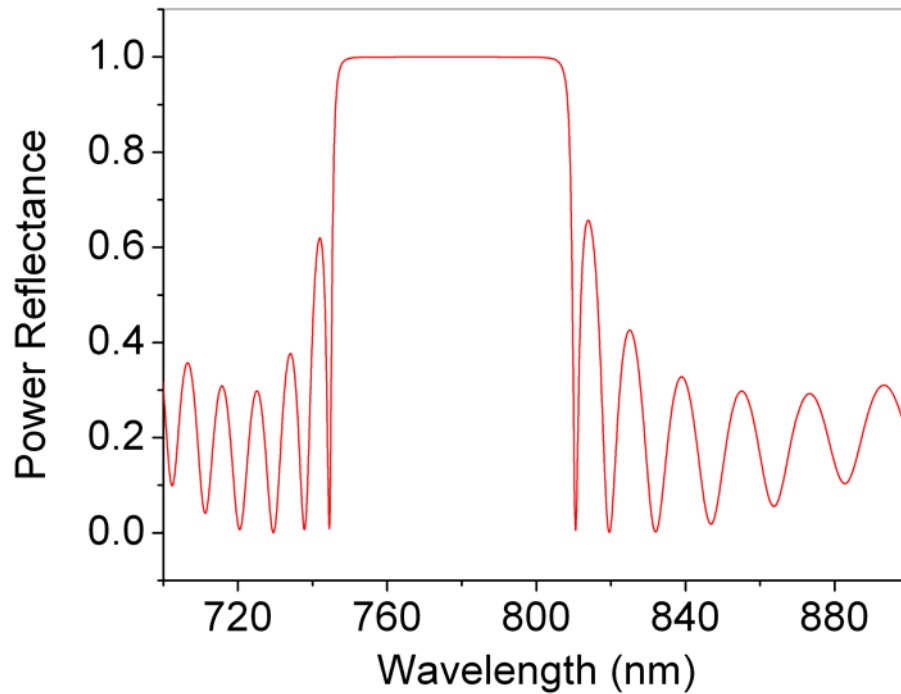


Fig. 3.7. Theoretical power reflectivity spectrum from DBR. DBR design is centered on $\lambda = 780\text{nm}$ and composed of 40 alternating pairs of AlAs and $\text{Al}_{0.3}\text{Ga}_{0.7}\text{As}$ layers.

DBRs have a limited reflectance band. For example, in Fig. 3.7, the high reflectivity band of the DBR ranges from about 745 – 810 nm. The spectral width of the high reflectivity band is given by [49]

$$\Delta\lambda = \frac{2\lambda_{\text{Bragg}} \Delta n}{\pi n_{\text{eff}}}, \quad (3.11)$$

where Δn is the difference in refractive index between the two DBR layers and n_{eff} is the effective refractive index of the mirror. The effective refractive index is given by

$$n_{eff} = 2 \left(\frac{1}{n_1} + \frac{1}{n_2} \right)^{-1} . \quad (3.12)$$

3.3.3 VERTICAL-CAVITY SURFACE-EMITTING LASERS

VCSELs have received much attention from the research community ever since their first realization by Iga in 1979 [50]. VCSELs promise drastically reduced costs over other semiconductor laser technologies. Cost reductions due to wafer-level testing and packaging are possible with surface normal emitting VCSELs. In addition, 2-dimensional and dense parallel arrays can be easily manufactured and used in a variety of new and interesting system architectures. This technology has shown much promise and, as a result, has been highly developed for the telecommunication industry and other sensing applications. An excellent review of VCSEL technology is provided by Wilmsen et. al. [47].

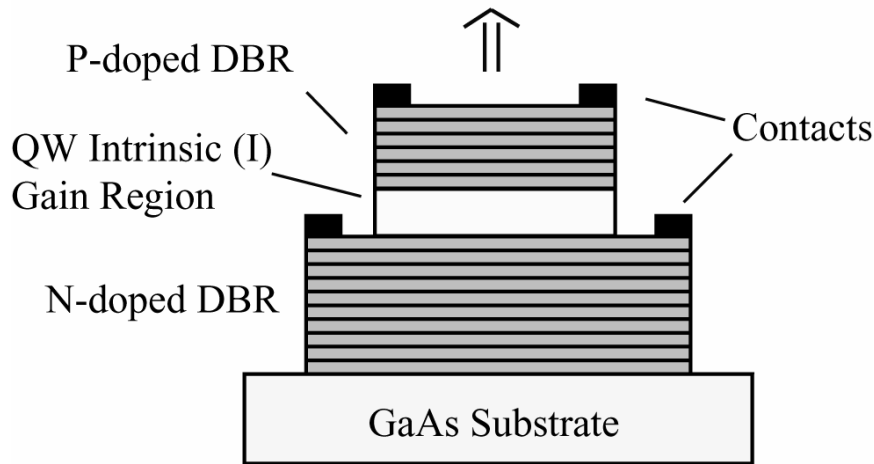


Fig. 3.8. Schematic of VCSEL. Two DBRs surround quantum well (QW) gain region. Electrical contact is made to the PIN diode in order to forward bias the diode and drive the VCSEL.

Fig. 3.8 shows a simplified schematic of a typical VCSEL. The VCSEL depicted in Fig. 3.8 is analogous to Fig 3.5 and the previous discussion regarding laser physics. The two DBR mirrors are used to form the laser cavity around the VCSEL quantum well

(QW) gain region. The basic electrical structure of the VCSEL is a PIN diode. The P and N regions are the top and bottom DBR of the VCSEL, respectively. The laser gain region in between the DBRs is the intrinsic (I) region. In order to achieve population inversion for optical gain, electrons and holes are electrically injected into the gain region by forward biasing the PIN diode.

VCSELs typically utilize quantum wells to achieve optical gain [46,47]. Quantum wells are very thin layers, typically between 5 – 10 nm, placed between two materials of higher electronic bandgap. In this manner, quantum wells provide an energy well for electrons and holes, see Fig. 3.9. In other words, the holes and electrons fall into the quantum well because this is energetically favorable. In order to achieve optical gain, carriers are pumped into these quantum wells and population inversion is obtained in the thin layers. One of the most useful properties of quantum wells is that population inversion is much easier to achieve in a thin layer of material rather than a bulk layer.

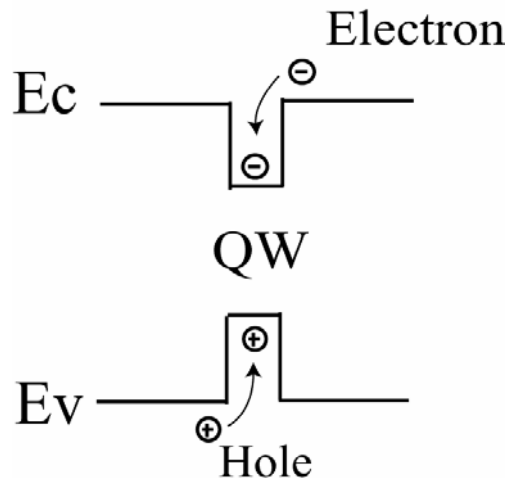


Fig. 3.9. Diagram of quantum well. A thin (5-10nm) material is placed between two materials of larger bandgap, creating an energy well to which electrons and holes are attracted.

An appropriate material system must be chosen to enable VCSELs. As seen in Fig. 3.8., a VCSEL is made from many thin material layers needed to form DBRs and quantum wells [47]. The active region of the laser must be a high quality crystalline material so that non-radiative recombination mechanisms are suppressed, increasing the rate of stimulated emission or laser gain. Achieving such complex and large material

stacks while maintaining good material quality is a significant challenge. The $\text{Al}_x\text{Ga}_{1-x}\text{As}$ material system is ideal for growing such crystalline layer structures. Over the entire alloy range, there is a relatively small lattice mismatch so many different high quality crystalline materials can be grown by epitaxial growth methods, such as molecular beam epitaxy (MBE) or metal organic chemical vapor deposition (MOCVD). In addition, the index contrast is large between GaAs and AlAs, which is useful for making DBR structures.

The spectral range of VCSELs is limited due to a variety of material and design limitations [47]. VCSELs lasing at 980 and 850nm have become a standard technology. Moving towards shorter wavelengths becomes increasingly difficult, and useful VCSELs below 600nm have not been successful [51,52]. However, promising work continues in the area of visible VCSEL fabrication [53]. Much research has been invested to push VCSELs towards longer wavelengths in order to be compatible with optical fiber communications. VCSELs which lase at 1.3 and 1.5 μm have been successful; however, more research is needed to bring these devices to mass market [54,55].

3.4 CONCLUSIONS

Some basic concepts and physics of common optoelectronic devices are reviewed as background for understanding the sensor operation detailed in the rest of this thesis. The discussion focused on VCSELs, PIN photodetectors and DBRs which are the key elements used in the design of the integrated fluorescence sensor.

CHAPTER 4

SENSOR DESIGN

As discussed in Chapter 1, an integrated fluorescence sensing solution is needed to enable the true potential of miniaturized and total analysis systems (μ TAS) and other sensing applications. Several technologies could be used to fabricate an integrated fluorescence sensor. Leveraging optoelectronic technologies developed for telecommunications will result in drastically reduced costs and mass production and could enable a disposable fluorescence sensing solution. The design of the integrated sensor presented in this work capitalizes on well developed vertical-cavity surface-emitting laser (VCSEL) technology by achieving a complete fluorescence sensor through a few simple modifications to a typical VCSEL design used for telecommunications.

4.1 LITERATURE REVIEW

There are numerous attempts found in literature towards the goal of an integrated biosensor. A complete overview of the literature is a daunting task due to the many sensing technologies, numerous applications and the fact that the success of each technique is highly dependent on the particular sensing application. Several good reviews are available that discuss various integrated sensing approaches and technologies [10,12,13].

The literature reviewed here focuses on some of the more well known approaches towards integrated fluorescence sensors [56-65]. All of these previous methods have severe limitations. For example, the use of integrated waveguides and optical gratings to excite fluorescent molecules has been proposed [56,57]. The integration of waveguides adds additional complexity to biochip fabrication and may be difficult to implement with a large number of channels. In addition, these waveguide-based sensors typically use discrete light sources, filters and photodetectors, complicating packaging and alignment.

Several groups have proposed the integration of photodetectors directly onto the biochip [58-60] but have not shown an integrated excitation source. The integration of optoelectronic devices such as photodetectors directly onto the biochip may be cost-prohibitive to disposable applications. Other integrated optical solutions have been proposed [61,62] but, once again, these systems use non-integrated and discrete optical components. Some progress towards a compact integrated sensor has been made by clever packaging of discrete optical components (semiconductor lasers or light emitting diodes (LEDs), photodetectors, optics and emission filters) for on-chip detection [63-65]. Again, the complex packaging of discrete optical components will dramatically increase costs.

4.2 NOVEL APPROACH

The approach used in this work capitalizes on telecommunication technology and monolithically integrates lasers, photodetectors and optical filters on the same substrate. The cost-effectiveness of this approach could enable the development of applications with disposable fluorescence sensors that may be cost-prohibitive with systems that use discrete optical components. In addition to inexpensive, high-quality optoelectronic components such as lasers, photodetectors and optical filters, capitalizing on telecommunications technology will enable packaging and integration benefits, such as easy integration with avalanche photodetectors (APDs), CMOS electronics and micro-optics [47,66-70]. Also, these optoelectronic devices allow for high speed operation of greater than 10Ghz, which would be useful for fluorescence lifetime detection [68,71,72]. Fig. 4.1 illustrates the general goal and theme of this research. Shown in Fig. 4.1 is a complete integrated sensing system that capitalizes on optoelectronic technologies combined with CMOS electronics, micro-optics and microfluidics. It is important to note that the embodiment shown in Fig. 4.1 is not realized in this work. In other words, the sensor presented in this thesis does not incorporate CMOS electronics and wafer bonding; however, this thesis demonstrates the optoelectronic, optical and microfluidic elements in an identical architecture.

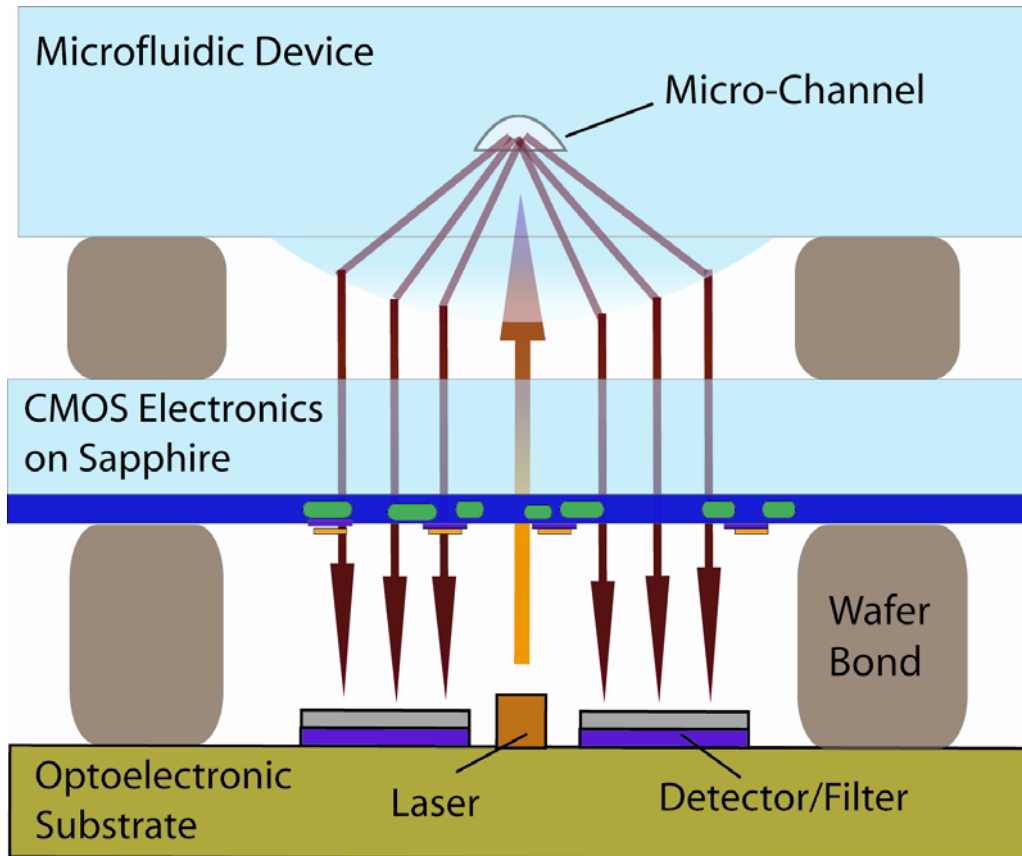


Fig. 4.1. Illustration of ideal sensing system which utilizes state-of-the-art optoelectronic technology, such as VCSELs, photodetectors and optical filters. In addition, CMOS electronics, micro-optics and microfluidics can be easily integrated with the optoelectronic devices to make a complete system. CMOS electronics are not implemented in the sensor presented in this thesis.

4.3 OPTICAL ARCHITECTURES

An integrated sensor is designed to incorporate all modules of a conventional laser-induced fluorescence (LIF) detection system (*i.e.* laser, detector, optics, and optical filter) into a small semiconductor-based device. The optoelectronic design presented below in Section 4.4 capitalizes on VCSELs, which emit normally to the wafer surface. Several general sensor architectures which can be realized with VCSELs are illustrated in Fig. 4.2. The photodetector and VCSEL are integrated side by side. On the side of the detector nearest the fluorescent molecule, an optical filter blocks reflected and scattered laser light from reaching the detector to reduce laser background.

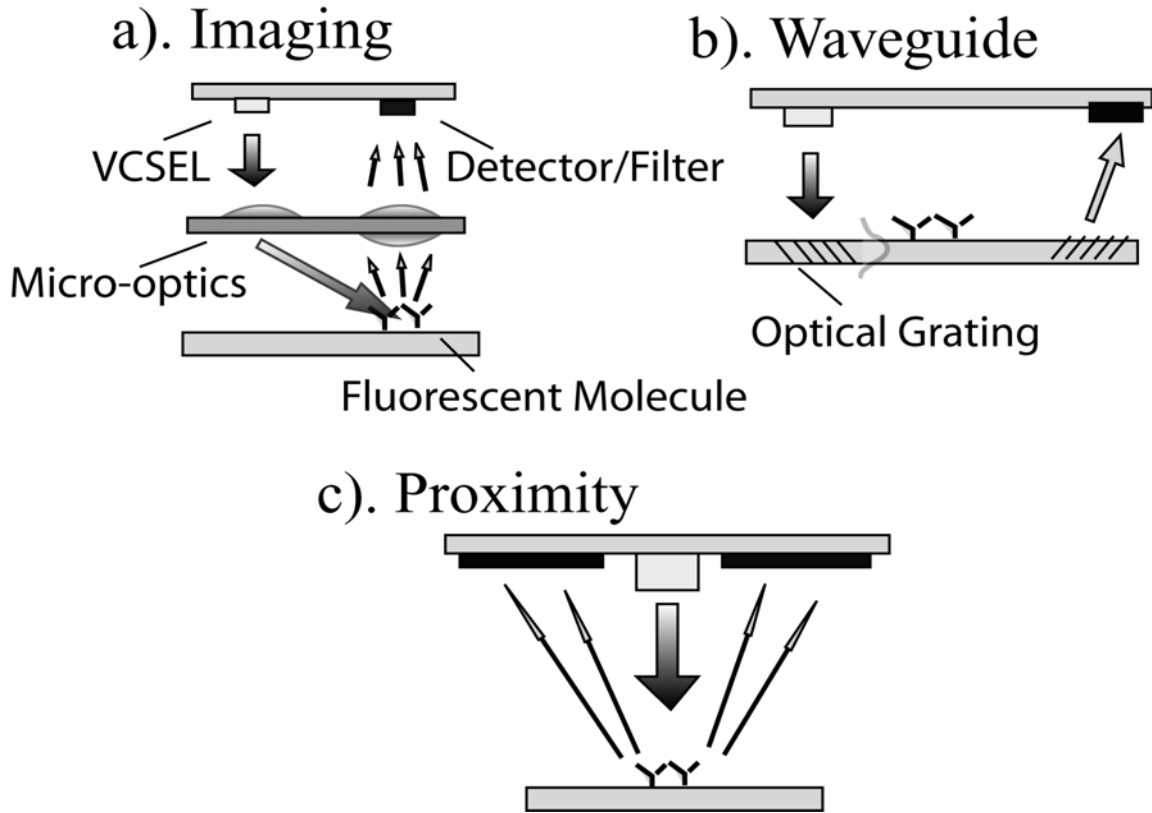


Fig. 4.2. Schematic of general system architectures possible with VCSELs: a) Imaging, b) Waveguide, and c) Proximity.

Fig. 4.2a shows an imaging architecture in which refractive or diffractive optics are used to focus the laser onto the fluorescent molecules and collect their emitted fluorescence. Optically collecting the emitted fluorescence with lenses enables the use of small area photodetectors. Due to the small area photodetector, a large level of spatial filtration can be achieved, which is perhaps the greatest advantage of the imaging architecture. As discussed in Section 2.3.2, spatial filtration in addition to spectral filtration is needed for decreasing the amount of laser background and achieving high sensitivity fluorescence detection. Other advantages of smaller photodetectors are less cross-talk between adjacent sensors, lower photodetector dark current, higher levels of integration, and high speed operation for fluorescence lifetime detection [23]. Unfortunately, obtaining high numerical aperture (NA) microlenses for large fluorescence collection efficiency can be difficult and expensive; however promising work continues in this area [73-76].

Fig. 4.2b shows a waveguide architecture, in which a grating is used to couple the excitation beam into a waveguide. The fluorescent molecules are immobilized to the surface of the waveguide and excited by the evanescent tail of the optical waveguide mode. The emitted fluorescence is collected by the waveguide and diffracted by another grating into the detector. In evanescent waveguide sensors, the evanescent tail senses only the first 100-200 nm from the waveguide surface. As a result, good rejection of volume fluorescence can be obtained and only molecules attached to the surface are detected [56]. Unfortunately, this method requires the use of immobilized probes onto the surface of the waveguide, which makes this method unsuitable for microfluidic separations such as capillary electrophoresis (CE) or chromatography. In addition, fabricating optical gratings and waveguides directly onto the biochip may be cost-prohibitive to disposable biochip applications.

Fig. 4.2c shows a proximity architecture, in which the biochip is located next to the sensor. The excitation light propagates directly onto the fluorescent tags, and their fluorescence is collected by a large-area photodetector that surrounds the light source. The short-distance and large-area photodetector can result in large collection efficiencies of greater than 20%. Unfortunately, due to the large-area photodetector, it can be difficult to achieve a high level of spatial filtration so laser background levels can be problematic. In addition, crosstalk between adjacent sensor channels is significant, and the sensor channel spacing needs to be much larger than that of the imaging architecture. As described in the following chapters, the proximity sensor is implemented. Also, a microfluidic implementation of the proximity architecture is realized to test the sensor on a microfluidic format as described in Section 8.2. The proximity architecture is appealing due to high fluorescence collection efficiency, high alignment tolerance and avoidance of complicated micro-optical fabrication.

When compared with transmission architectures [77], in which the light source and photodetector are located on opposite sides of the biochip, the one-sided architectures shown in Fig. 4.2 have several advantages. The ability to integrate the light source and detector on the same side allows for easy replacement of the biochip for simple usage with disposable biochips. The alignment between the light source and the detector is

obtained as part of device fabrication via microlithography and can easily be better than 2 μ m. Unlike transmission type architectures, the one-sided sensing architecture decouples the biochip design from the optical sensing design so, for example, one can use optically absorbing substrates for the biochip, such as silicon. Perhaps the most important advantage of the one-sided architectures is the significant reduction in laser background level. By not shining the laser directly towards the detector, significant spatial filtration can be achieved, which is extremely important for high-sensitivity applications [24,77].

4.4 OPTOELECTRONIC DESIGN

4.4.1 INTEGRATION

The VCSEL, photodetector and emission filter are monolithically integrated by capitalizing on traditional VCSEL technology and realized using the same material and fabrication technologies [78]. Fig. 4.3 shows a schematic of the optoelectronic design in a proximity architecture. Chapter 5 details the precise epitaxial design of the sensor. The VCSEL includes two distributed Bragg reflectors (DBRs) and a laser gain region. Adjacent to the VCSEL, a simple PIN photodetector is formed by adding an intrinsic GaAs region underneath the standard VCSEL epitaxial structure. The PIN photodetector uses the N-doped DBR as both an optical filter and electrical contact. Section 4.4.2 describes how the N-DBR is utilized as an optical filter.

A design choice is made to utilize an N-doped DBR for the bottom VCSEL mirror, resulting in a P-type GaAs substrate. Whereas, a N-type GaAs substrate could be used by implementing a P-doped DBR for the bottom VCSEL mirror. The N-doped bottom mirror design is chosen because, for the intracavity contact, there is less current crowding around the edge of the VCSEL oxide aperture due to the higher conductivity of N-doped layers [79]. Less current crowding results in more ideal mode behavior and better efficiency for single mode laser designs.

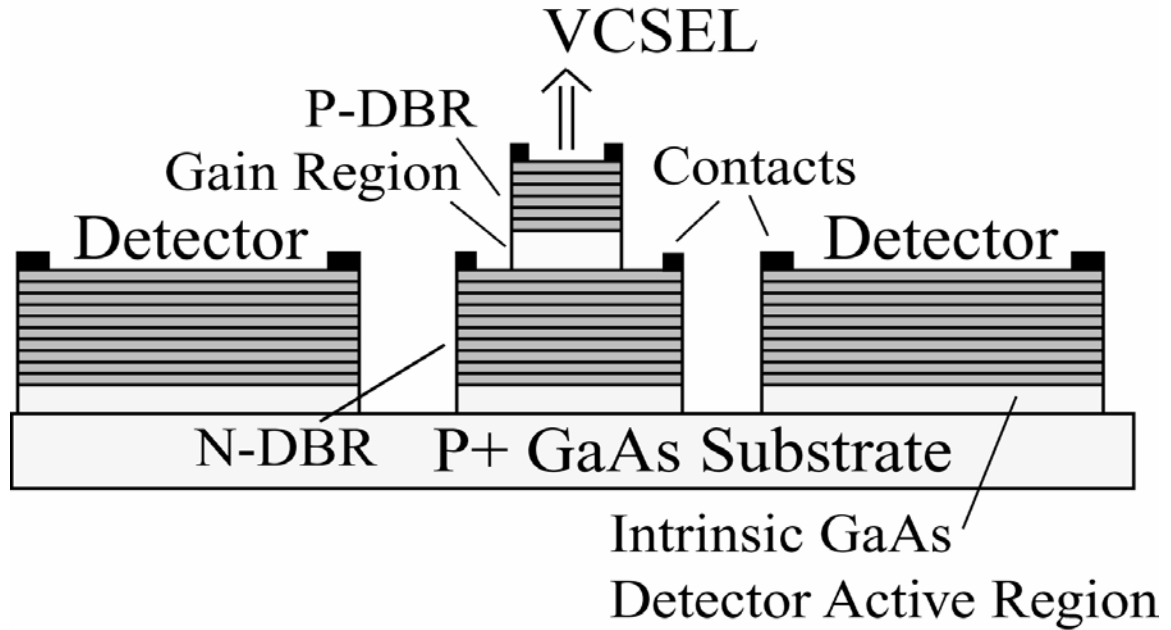


Fig. 4.3. Schematic of optoelectronic design. VCSEL is grown on top of the photodetector. Photodetector uses the bottom N-DBR of the VCSEL as an optical filter. Complete sensor unit is made through one simple modification to a typical VCSEL epitaxial structure.

One major disadvantage of utilizing telecommunication technologies is the limited spectral range. VCSELs operating in the near-infrared (NIR) are commonplace; whereas, visible VCSEL have not been successful [47]. Fortunately, as discussed in Section 2.4, working with NIR fluorescence can be a significant advantage for some applications due to low autofluorescence. Commercially available NIR dyes from a company called LICOR are targeted with this technology. Therefore, the VCSELs are designed to operate at a wavelength of 770nm for successful excitation of these NIR fluorescent markers.

4.4.2 FILTER DESIGN

Fig. 4.4 illustrates how the N-DBR acts as a filter for the photodetector. A simple thin film optical simulator based on a transfer matrix algorithm is used to simulate the theoretical performance of the DBR filter, which includes material dispersion models for $\text{Al}_x\text{Ga}_{1-x}\text{As}$ [48]. The DBR is highly reflecting at the laser wavelength of 770nm ($R > 99.999\%$) and relatively transparent at the Stokes' shifted dye emission. Therefore, laser photons reflected and scattered above the sensor are rejected by the filter before reaching the detector active region; whereas, the fluorescence signal is transmitted through the

DBR and detected. The advantage of the proposed design is that the VCSEL's mirror is used as the optical filter, thereby achieving optical filtration at little additional cost and complexity.

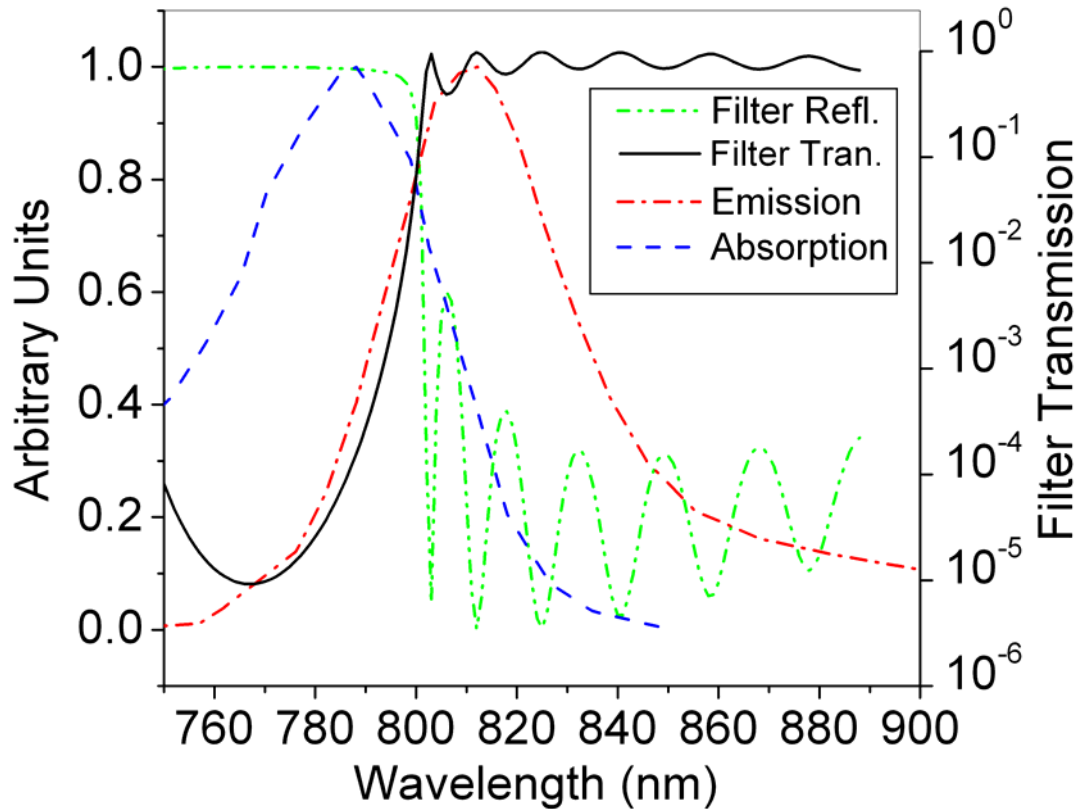


Fig. 4.4. Theoretical reflectivity of DBR plotted together with absorption and emission characteristics of IR-800 dye on a linear (left) scale. Theoretical transmission of DBR is plotted on a log scale (right).

The filter illustrated in Fig. 4.4 and utilized in the final sensor design is not optimal. Due to the reflectivity sidelobes that are characteristic of DBRs, fluorescence signal transmission through the DBR is low as described in Section 6.2.2. This non-optimal design is pursued in order to follow standard VCSEL design and growth procedures. However, the mirror design can be modified to give more ideal filtering behavior and eliminate the reflectivity sidelobes [48]. For example, Fig. 4.5 illustrates how the simple addition of a $\lambda/8$ matching layer on top of the filter can significantly reduce the DBR reflectivity sidelobes. Better performance than that shown in Fig. 4.5 can be obtained by a more efficient matching design.

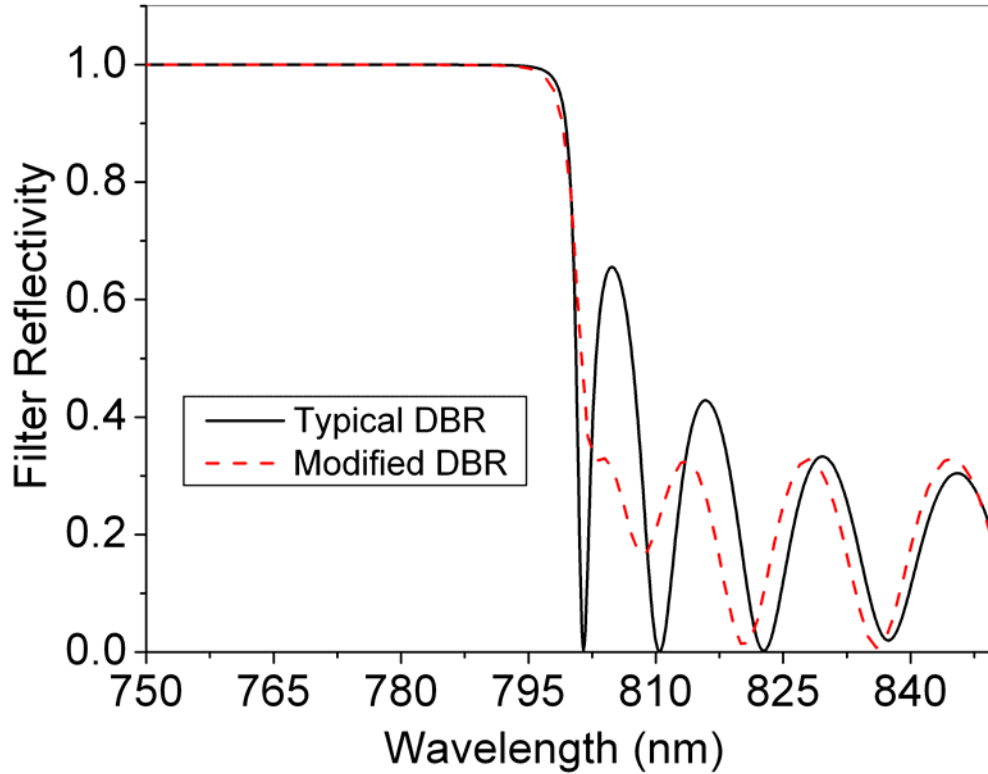


Fig. 4.5. Theoretical reflectivity from modified DBR design compared with a typical DBR design. The addition of a simple $\lambda/8$ matching layer on top of the DBR significantly improves the pass-band performance of the filter.

The above filter design offers another significant advantage other than simplicity of fabrication. Typical interference filters are sensitive to changes in incident angle, whereas the filter presented here is relatively insensitive. The large optical index of the $\text{Al}_x\text{Ga}_{1-x}\text{As}$ material ($n \approx 3.3$) used to make the filter reduces the angular sensitivity due to Snell's law,

$$n_i \sin(\theta_i) = n_t \sin(\theta_t). \quad (4.1)$$

Snell's law describes how a ray passes from one material (n_i) to another material (n_t), where n_i and n_t are the optical indices of the incident and transmitted material at the interface, and θ_i and θ_t are the incident and transmitted angle to the normal of the interface. Due to the relatively high optical index of $\text{Al}_x\text{Ga}_{1-x}\text{As}$, highly off-normal rays are strongly refracted towards the normal inside the DBR, effectively reducing the angle of incidence or collimating the light. Simulations show that filtration of optical density

(OD) 4 or 10^{-4} transmission is possible for light rays incident at highly off normal angles ($\theta < 60^\circ$) as shown in Fig. 4.6. In an integrated system, where scattered laser light may be incident over a wide range of angles, maintaining filtration over a large range of angles is critical.

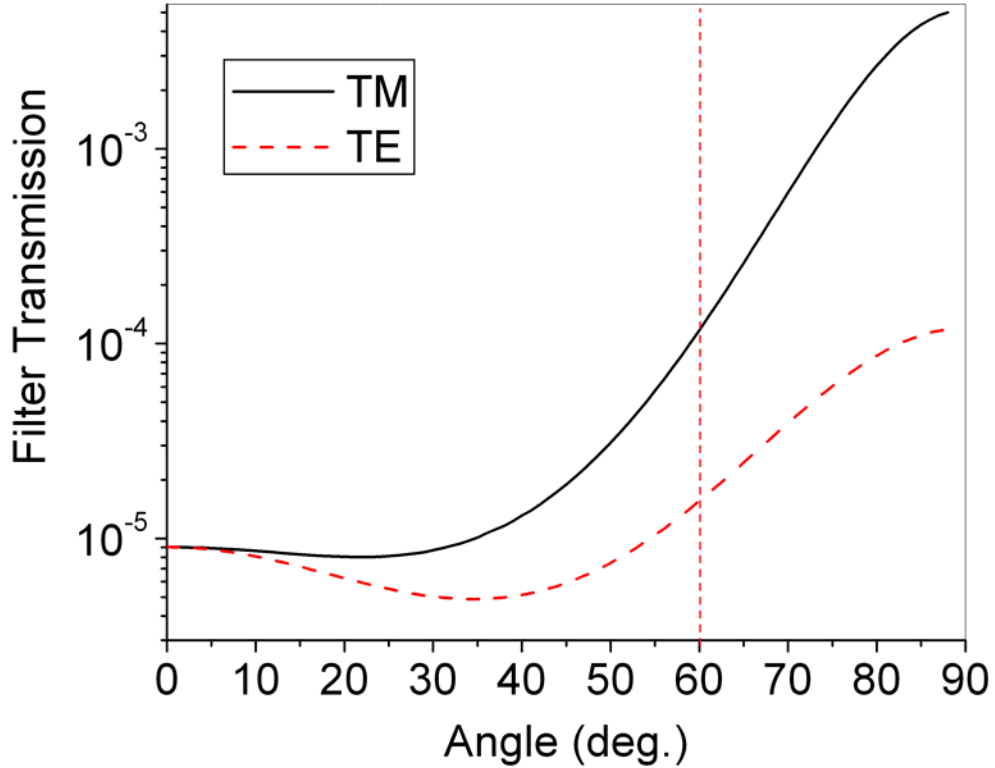


Fig. 4.6. Theoretical angular dependence of $\text{Al}_x\text{Ga}_{1-x}\text{As}$ filter for TE and TM modes. Good filtration of OD 4 is maintained up to $\theta = 60^\circ$ at $\lambda = 770\text{nm}$.

Another advantage of the $\text{Al}_x\text{Ga}_{1-x}\text{As}$ material system for optical filter design is the ability to control the material absorption edge by varying alloy composition. In this manner, absorption based filters could be implemented along with an interference filter in the current design. Care must be taken to make sure that the absorption filter does affect the laser by decreasing the cavity quality factor. Placing the absorption filter underneath the current interference filter would be a reasonable design choice. The advantage of absorption-based filters is that these filters do not degrade for highly off-normal angles [65].

4.5 CONCLUSIONS

The optoelectronic design of the sensor capitalizes on convention VCSEL technology for drastically reduced cost and size and the potential for highly parallel architectures. Through one simple modification to a typical VCSEL, all the modules (laser, photodetector and optical filter) required for a fluorescence sensor are achieved. The $\text{Al}_x\text{Ga}_{1-x}\text{As}$ DBR filters offer interesting design capabilities when compared to conventional dielectric materials due to the high optical index of $\text{Al}_x\text{Ga}_{1-x}\text{As}$ and ability to the control the material bandgap. The following chapters detail the fabrication and implementation of the design presented here.

CHAPTER 5

FABRICATION

In Chapter 4, the general sensor design is introduced and described. The design integrates a vertical-cavity surface-emitting laser (VCSEL), photodetector and optical filter to create a complete fluorescence sensor. This chapter describes how these sensors are realized, which involves the fabrication of low-noise PIN photodetectors, distributed Bragg reflector (DBR) optical filters, intracavity contacted 773nm VCSELs and metal optical isolation elements. The detailed epitaxial design of the optoelectronic components is provided here. In addition, a general description of the semiconductor processing procedures is provided that illuminates some of the more difficult fabrication procedures needed to realize the sensors. Appendices A and B provide exact details of the epitaxial structure and processing recipes and are referenced throughout the overview provided by this chapter.

5.1 LOW-NOISE PHOTODETECTOR FABRICATION

Low-noise photodetectors are extremely important to enable high sensitivity fluorescence detection. As described in Section 6.1.1, photodetector dark current creates a background which can limit sensitivity due to shot noise. A goal of this research is to realize photodetectors with low dark current. Therefore, simple photodetector structures are made in order to optimize fabrication procedures for low dark current. Fig. 5.1 shows the PIN photodetector epitaxial structure that is grown by molecular beam epitaxy (MBE) and a scanning electron microscope (SEM) image of a processed mesa photodetector. These low-noise photodetectors are referenced in this thesis as sample number P222. The integrated DBR is designed for $\lambda_{\text{Bragg}} = 770\text{nm}$. The exact growth recipe or epitaxial structure is given in Appendix A.1. For more information on MBE growth procedures, A. Cho provides an excellent reference [80]. Simple processing steps are followed to

realize the mesa photodetector. A standard bilayer liftoff process (Appendix B.1.1) is used to define the top ring contact. After N-metal deposition (Appendix B.1.4) and metal liftoff, thermal annealing (Appendix B.1.5) is used to make an ohmic contact to the GaAs capping layer. P-metal is deposited on the backside of the substrate following Appendix B.1.3. Then, the photodetector mesa is defined by simple lithography (Appendix B.2.2) and electron cyclotron resonance-reactive ion etching (ECR-RIE) (Appendix B.2.3). After dry etching 1 μ m into the P+ substrate, the detectors are electrically isolated. For the reader's aid, much more detail of general fabrication methods can be found in the literature by R. Williams and S. K. Ghandhi [81,82].



Fig. 5.1. Low-noise PIN photodetectors (Wafer #P222). (Left) Epitaxial design for low-noise detector sample. See Appendix A.1 for exact epitaxial structure. (Right) SEM image of processed mesa photodetectors.

Section 6.1.1 details the electrical characterization of the low-noise photodetectors shown in Fig. 5.1. The photodetectors exhibit very low dark current of 500fA/mm detector diameter (note this is limited by surface generation, hence proportional to surface length rather than bulk generation). It is important to note that this dark current is highly sensitive to subsequent processing steps. High temperature processes, oxidation, and reactive polymers such as BCB should be avoided in order to maintain low detector dark current [83-85].

5.2 INTEGRATED SENSOR FABRICATION

5.2.1 EPITAXIAL STRUCTURE

The general epitaxial design and operation of the integrated sensor are discussed in Section 4.4. A detailed epitaxial structure is shown in Fig. 5.2 and is grown by metal-organic chemical vapor deposition (MOCVD) at Novalux, Inc. For more information on the general methods of MOCVD, G. B. Stringfellow provides an excellent resource [86]. Appendix A.2 gives the precise epitaxial structure for the integrated sensor. This sensor growth is referenced as wafer or sample #P763-5. The VCSEL is designed to lase at $\lambda = 770\text{nm}$. The VCSEL's top P-DBR consists of 26 $\lambda/4$ pairs of $\text{Al}_{0.25}\text{Ga}_{0.75}\text{As}$ and $\text{Al}_{0.95}\text{Ga}_{0.05}\text{As}$, and the bottom N-DBR consists of 40 $\lambda/4$ pairs. Compositional grading is used to decrease the electrical resistance of the top P-DBR, whereas no grading is used on the bottom N-DBR to preserve the detector's emission filter integrity. Moving towards the cavity, the top P-DBR doping is gradually reduced from $6 \times 10^{18} \text{ cm}^{-3}$ to $1 \times 10^{18} \text{ cm}^{-3}$ to reduce free carrier absorption [43,79]. A $5\lambda/4$ current spreading layer N-doped at $n = 1 \times 10^{18} \text{ cm}^{-3}$ is used for the bottom VCSEL intracavity contact. Two $\lambda/4$ $\text{Al}_{0.98}\text{Ga}_{0.02}\text{As}$ oxidation aperture layers surround the VCSEL cavity. The oxide apertures are doped less than the surrounding DBRs in order to reduce current crowding [79]. To allow the use of selective wet etches for making contact with the 10nm GaAs intracavity contact layer, no compositional grading is used from the current spreading layer into the VCSEL cavity. The λ cavity consists of four 7nm $\text{Al}_{0.11}\text{Ga}_{0.89}\text{As}$ quantum wells, separated by 8nm $\text{Al}_{0.3}\text{Ga}_{0.7}\text{As}$ barriers. A simple transfer matrix program is used to find the energy states in the quantum well design. The quantum wells are designed to have a gain offset of 10nm from the Fabry-Perot cavity resonance for high power operation, see [87]. The $2\mu\text{m}$ intrinsic GaAs active layer for the photodetector is located underneath the N-DBR. Many good references can be found in the literature that discuss and detail the epitaxial designs of similar VCSELs operating in this spectral range [51,52,79,88-94].

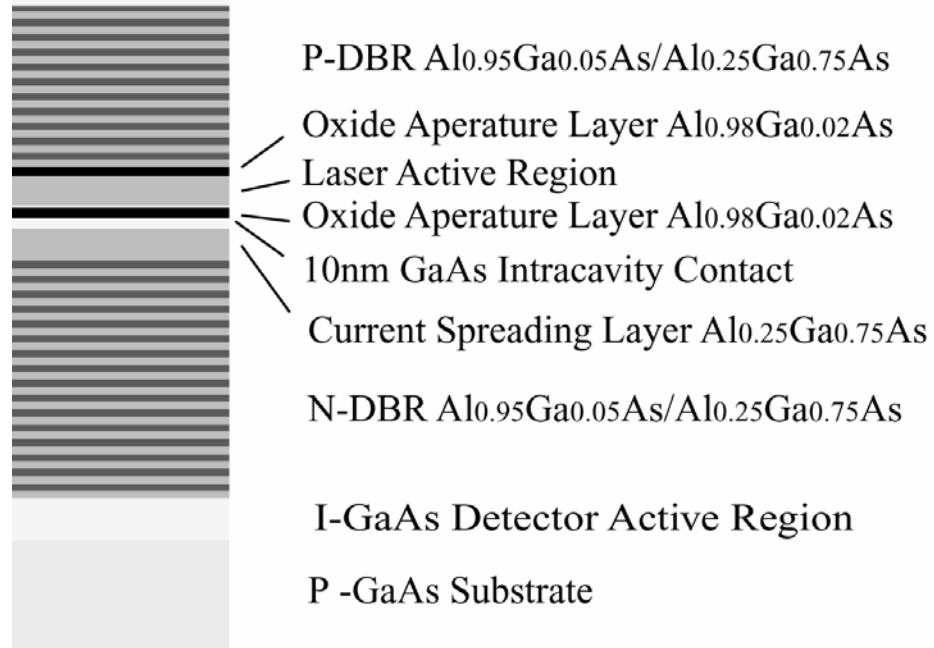


Fig. 5.2. Epitaxial structure for integrated sensor. The VCSEL is grown on top of the photodetector by MOCVD. See Appendix A.2 for exact structure.

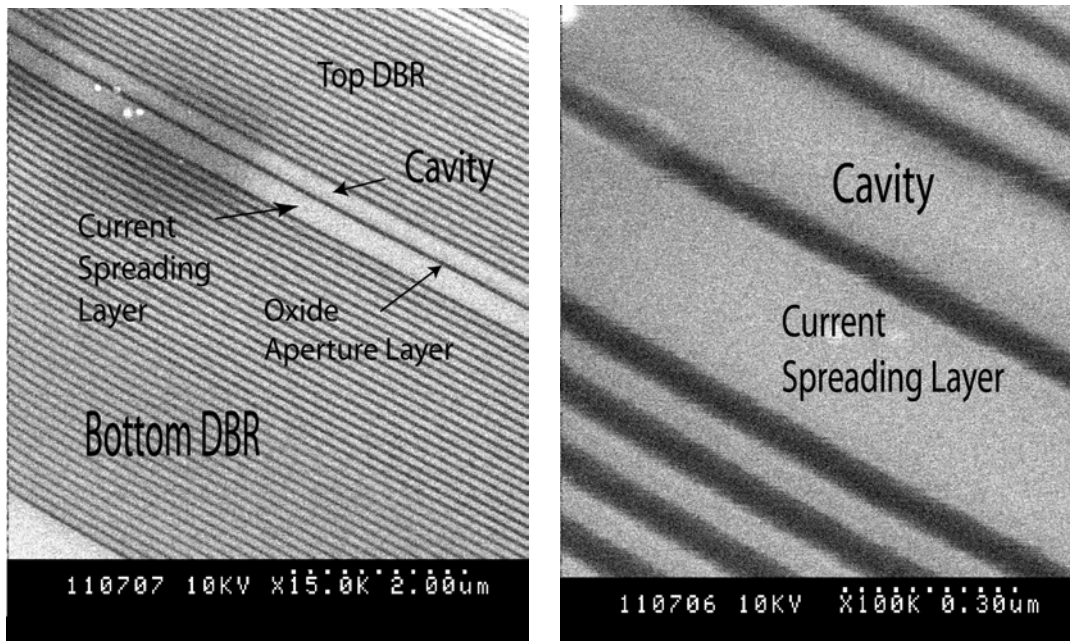


Fig. 5.3. SEM images of the sensor epitaxial structure. (Left) Complete epitaxial structure. (Right) Close-up image of cavity and current spreading layer.

SEM images are taken of the epitaxial structure, see Fig. 5.3. The images show that the structures are grown as designed. In addition, the SEM images show that the growth

is of high quality with smooth interfaces between material layers. The current spreading layer, cavity and DBR mirrors are clearly visible in the images. Unfortunately, the images do not produce enough contrast and resolution to view the quantum well structures within the VCSEL cavity.

5.2.2 SEMICONDUCTOR PROCESSING

There are some unique fabrication challenges associated with realizing the monolithically integrated fluorescence sensors. Much of this thesis work is dedicated to overcoming these challenges and developing robust processes [78,95]. The following section reviews the fabrication procedures used to realize these sensors. Several good references of general fabrication methods can be found in the literature and may be useful to the reader [81,82].

Fig. 5.4 shows SEM images of processed sensors in a proximity configuration. The VCSEL is located in the center of the annular shaped photodetector/filter structure. Two interconnect lines or vias can be seen making contact to the VCSEL structure and one via is made to the photodetector/filter structure. The substrate is the other electrical contact for the photodetector. Cured photoresist formations are used to make the electrical vias as described below. In addition, cured photoresist formations are used to develop metal optical blocking layers for optical isolation purposes as described below.

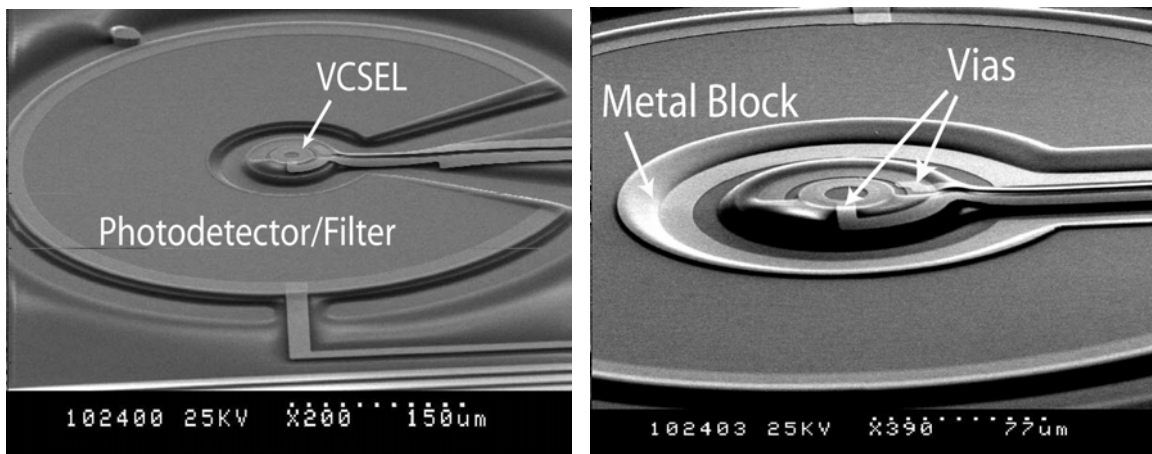


Fig. 5.4. SEM images of processed sensors. (Left) Complete sensor unit in a proximity architecture. (Right) Close-up image of VCSEL showing via formations and metal blocking layers.

Many photolithography steps are required to realize the integrated sensors shown in Fig. 5.4. With each photolithography step, resist beads, often referred to as edge beads, can grow in size along the edge of the wafer piece due to incomplete development from resist film aberrations and tweezer marks. These beads can cause significant problems during contact mask alignment. Edge beads can prevent the mask from getting close to the wafer during alignment so the alignment can be compromised. In addition, diffraction effects can be problematic if the mask and wafer are separated too far during exposure. For example, exposure or diffraction spots can occur in the center of patterned resists circles [27]. Therefore, it is extremely important to remove edge beads with each photolithography step in order to complete the large number of processing steps. Exposure edge bead removal is found to work extremely well and involves exposing the edge bead and subsequent development before mask exposure, see lithography recipes in Appendix B.

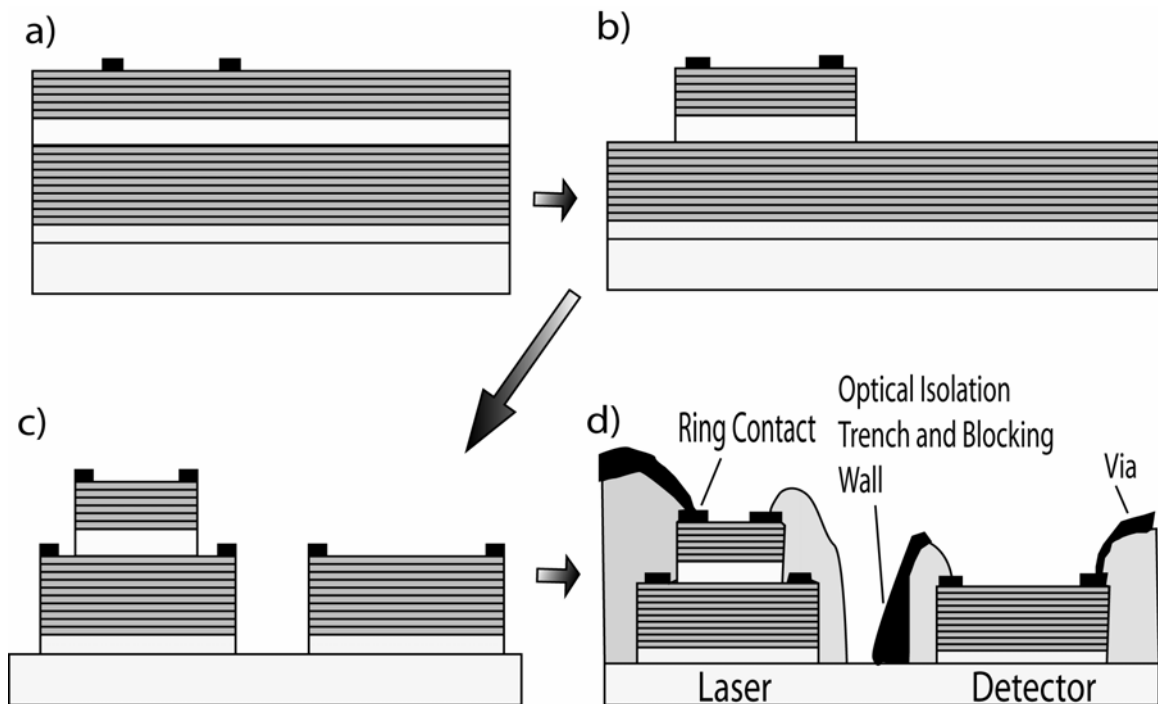


Fig. 5.5. Schematic of semiconductor processing sequence used to realize sensor. See Appendix B for detailed processing recipes.

Fig. 5.5 shows a schematic of the process flow used to create the sensors shown in Fig. 5.4. The process begins with defining the top VCSEL ring contact, see Fig. 5.5a. A

bilayer liftoff process is used to yield an undercut profile. For the small VCSEL contacts, achieving an undercut profile is needed to liftoff the center of the contact rings. Liftoff photolithography (Appendix B.1.1) is used to define the liftoff mask for the top VCSEL ring contact. Then, E-beam evaporation is used to deposit Ti/Pt/Au (Appendix B.1.3) for contact to the P-DBR. The top-contact dimensions are 20 and 40 μm inner and outer diameter, respectively. The next photolithography (Appendix B.2.1) step is used to mask the top mesa etch of the VCSEL. Standard positive photoresist is used to cover the center of the top ring contact while the outside of the metal ring masks the dry etch and defines the top mesa dimensions i.e. a self aligning process.

For VCSELs and other thermally sensitive optoelectronic devices, it is important to use a GaAs contact layer to minimize contact resistance because $\text{Al}_x\text{Ga}_{1-x}\text{As}$ tends to oxidize and increase contact resistance. Unfortunately, GaAs is absorbing at 770nm so the intracavity contact layer must be kept to a minimal thickness and placed at an optical null within the cavity in order to maintain the cavity quality factor required for lasing. Typically, researchers utilize a 10-20 nm GaAs intracavity contact layer for VCSELs operating in this spectral range [90]. Contacting to such a thin layer is a challenge and selective wet etches are used to control the etch depth. The general methodology to control the etch depth is to dry etch into the cavity of the VCSEL and, then, perform selective wet etching to etch down to the thin 10nm GaAs intracavity contact layer, see Fig. 5.5b.

ECR-RIE (Appendix B.2.3) is used to etch halfway into the λ -cavity of the VCSEL. Precise control of the etch depth is important because selective wet etches are used in the subsequent steps. An optical monitor, which uses a laser diode ($\lambda = 670\text{nm}$ and 70° angle of incidence) in a simple reflectivity setup, is used to control the etch depth precisely [96]. Fig. 5.6 shows the etch profile from the reflectivity monitor. The figure shows an etch through the cavity; whereas, during the top mesa formation described below, the etch stop is halfway through the VCSEL cavity as marked in the figure. The reflectivity oscillations from each DBR pair are clearly seen, totaling 26 plus one additional oscillation for the oxide aperture. Immediately following the oxide aperture, attenuation in the oscillation amplitude is observed because the laser diode emission is

strongly absorbed in the cavity, reducing interference effects. The oscillation amplitude increases as the etch proceeds to the next oxide aperture interface due to smaller cavity absorption. Another decrease in oscillation amplitude is observed after the 2nd oxide aperture because the current spreading layer strongly absorbs the diode emission similar to the cavity as discussed before. As seen in Fig. 5.6, good control of the etch depth is possible with the optical monitor. In fact, the limiting parameter during dry etching is the etch non-uniformity across the wafer piece due to the uneven electrical and thermal contact to the carrier wafer. By etching into the cavity of the VCSEL, this non-uniformity problem is alleviated because the cavity length is usually greater than the etch non-uniformities. Nonetheless, considerable care needs to be taken to maintain good etch uniformity over the entire sample. It is found that attaching the sample to the carrier wafer with double-sided copper tape consistently produces good etch uniformity over a majority of the sample.

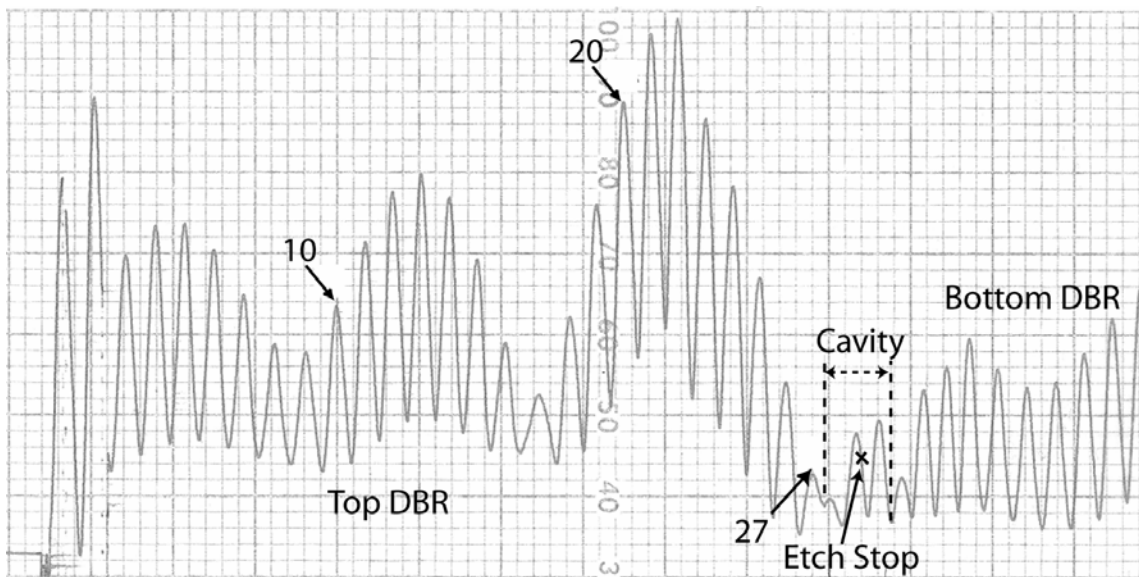


Fig. 5.6. Measured reflectivity profile during dry etching of sensor (P763-5). Image shows reflectivity etch profile through the cavity region; whereas, during processing of the sample, the etch is stopped as marked on the profile.

Having dry etched into the cavity of the VCSEL, a series of selective wet etches (Appendix B.2.4) are used to etch down to the thin 10nm GaAs intracavity contact layer, see Fig. 5.7. The same mask used for the previous dry etch is used for the wet etching. First, a citric acid etch for 2 min is used to remove the rest of the VCSEL cavity

($\text{Al}_{0.3}\text{Ga}_{0.7}\text{As}$) and stop on the oxide aperture layer ($\text{Al}_{0.98}\text{Ga}_{0.02}\text{As}$) [97]. Then, a buffered oxide etch (BOE) for 30s is used to remove the oxide aperture layer and stop on the 10nm GaAs layer [97]. A digital etch that alternates between an ammonium hydroxide based etch and hydrogen peroxide is used to clean and smooth the surface. Usually, one cycle of digital etching is enough to smooth the surface. These etches work well in that they provide reasonable etch selectivity and minimal undercutting of the mesa structures.

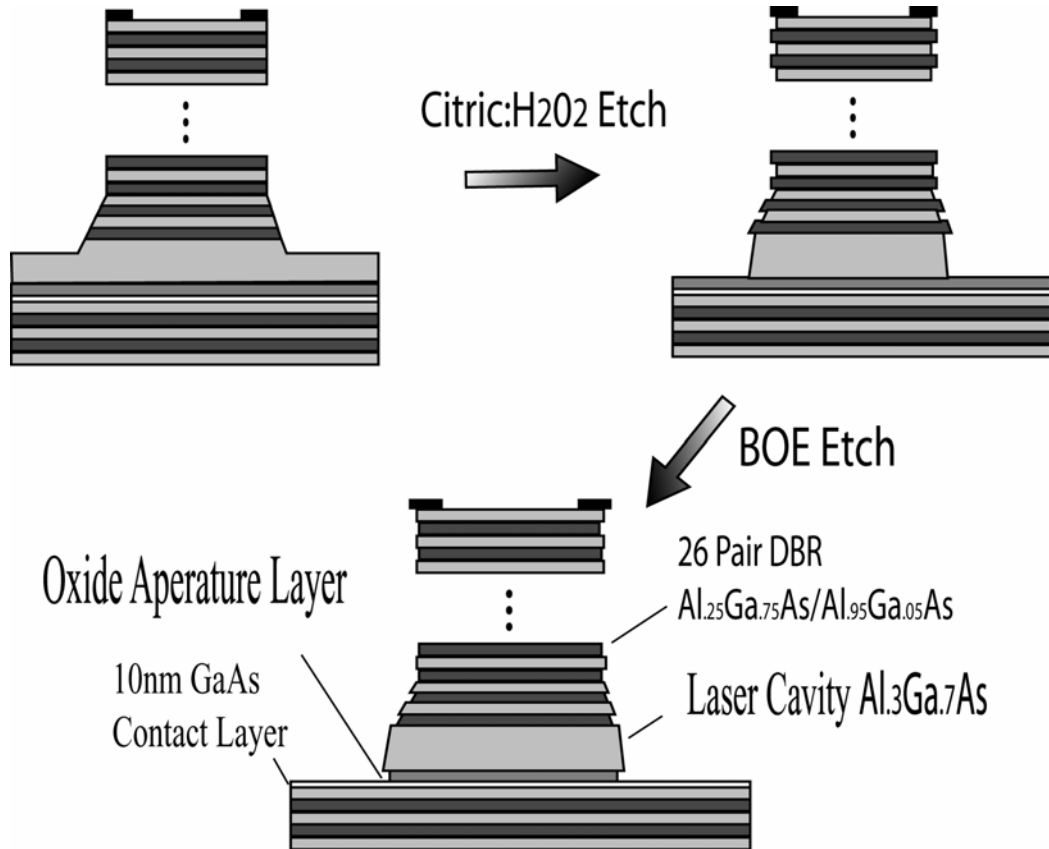


Fig. 5.7. Schematic of selective wet-etch sequence used to land on 10nm GaAs contact layer. Two selective etches are used in the process: 1) Citric acid-based selective etch and 2) BOE-based selective etch.

Mesa curvature at the bottom of the top mesa can create problems for the intracavity contacted structures. As shown in Fig. 5.7, the mesa widens towards the bottom due to dry etching artifacts. After wet etching, the cavity and top DBR layers can be significantly wider than the originally designed top mesa diameter. Fig. 5.8 shows an SEM image of the cavity protruding well beyond the top mesa edge. If intracavity

contacts are made too close to the mesa edge, then the contact can electrically short the VCSEL PIN junction.

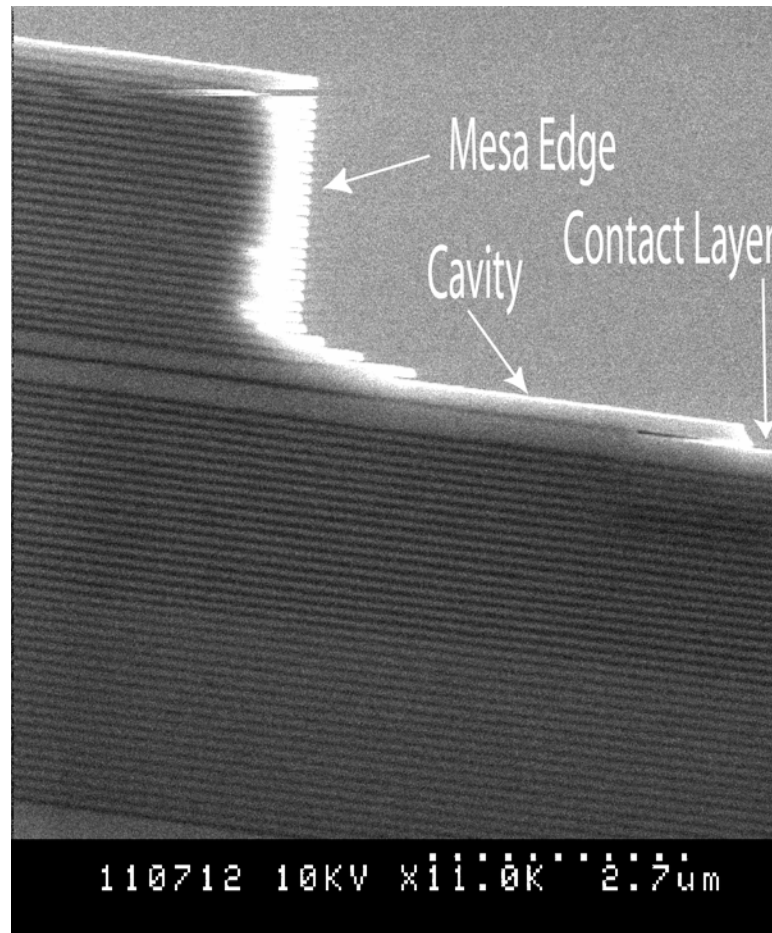


Fig. 5.8. SEM image of epitaxial layers protruding from mesa edge after selective wet etching. These protrusions must be considered when designing the intracavity contact mask.

The intracavity and photodetector contacts are defined during the same bilayer liftoff process (Appendix B.1.2). During photolithography for the intracavity contact, a thick film resist ($3\mu\text{m}$) is used to ensure that the mesa is completely covered. E-beam evaporation is used to deposit Au/Ge/Ni/Au (Appendix B.1.4) for the N-contact. The intracavity contact has inner and outer ring diameters of 50 and $90\mu\text{m}$, respectively. Similar to the VCSEL top mesa etch, the etch mask for the VCSEL bottom mesa and photodetector mesa is done using a self-aligning lithography process, see Appendix B.2.2. The bottom mesas are etched (Appendix B.2.3) by ECR-RIE, see Fig. 5.5c. The bottom mesa etch proceeds through the active layer of the photodetector for a total etch

depth of approximately $8\mu\text{m}$. The photodetector inner and outer diameters are made to be $200\mu\text{m}$ and 1mm , respectively. A thick film photoresist ($7\mu\text{m}$) is used for the mesa dry etch because of the large etch depth. The bottom mesa dry etch step exposes the active perimeter of the photodetector. The photodetector's dark current is highly dependent on subsequent processing steps. To maintain low dark current, it is best to avoid high temperature procedures and oxygen plasmas after exposing the detector active area. Therefore, contact annealing and wet oxidation of the VCSEL current aperture are conducted before the bottom mesa etch. The metal contacts are annealed (See Appendix B.1.5) at 420C for 1min. The oxidation apertures are oxidized (See Appendix B.3) in saturated nitrogen vapor at 395C for approximately 14min in order to oxidize to a $20\mu\text{m}$ oxide aperture diameter from a $40\mu\text{m}$ top mesa diameter [98]. Even though the VCSELs are designed to have two oxidation apertures, the VCSELs effectively only have one due to the uneven oxidation of the two oxidation layers. The top oxidation layer oxidizes to a much smaller diameter due to the edge effects shown in Fig. 5.8.

The next processing step involves making electrical contacts or vias to the VCSEL and photodetector ring contacts and developing metal blocking walls to optically isolate the photodetector from the laser (Fig. 5.5d). Cured positive photoresist provides excellent three-dimensional and insulating microstructures for such purposes [99,100]. A standard positive photoresist (AZ9260, Clariant) is used for this task. The process involves simple photolithography (Appendix B.4.1) and a 2-hour cure step (Appendix B.4.2) at 325C . The resist reflows during the oven cure, providing gradual sloping contours that are ideal for forming vias and blocking structures. Fig. 5.9 illustrates the slopping behavior of the cured resist and how this can be exploited to make electrical vias. Highly controlled reflowing is needed and oven curing profiles need to be optimized. Too much reflowing of the resist can cause the resist to completely cover electrical contacts or fill the optical isolation trench. Slow ramping of oven temperatures reduces the amount of reflow. The highly three dimensional or tall mesa structures of the sensor increase the amount of reflowing. For example, filling of the optical isolation trench is particularly problematic due to the resist flowing down into the trench due to gravity. It is found that the distance between the VCSEL bottom mesa edge and detector side wall needs to be greater than

50 μm to prevent the optical isolation trench from being completely filled, which limits how close the VCSEL and photodetector can be integrated.

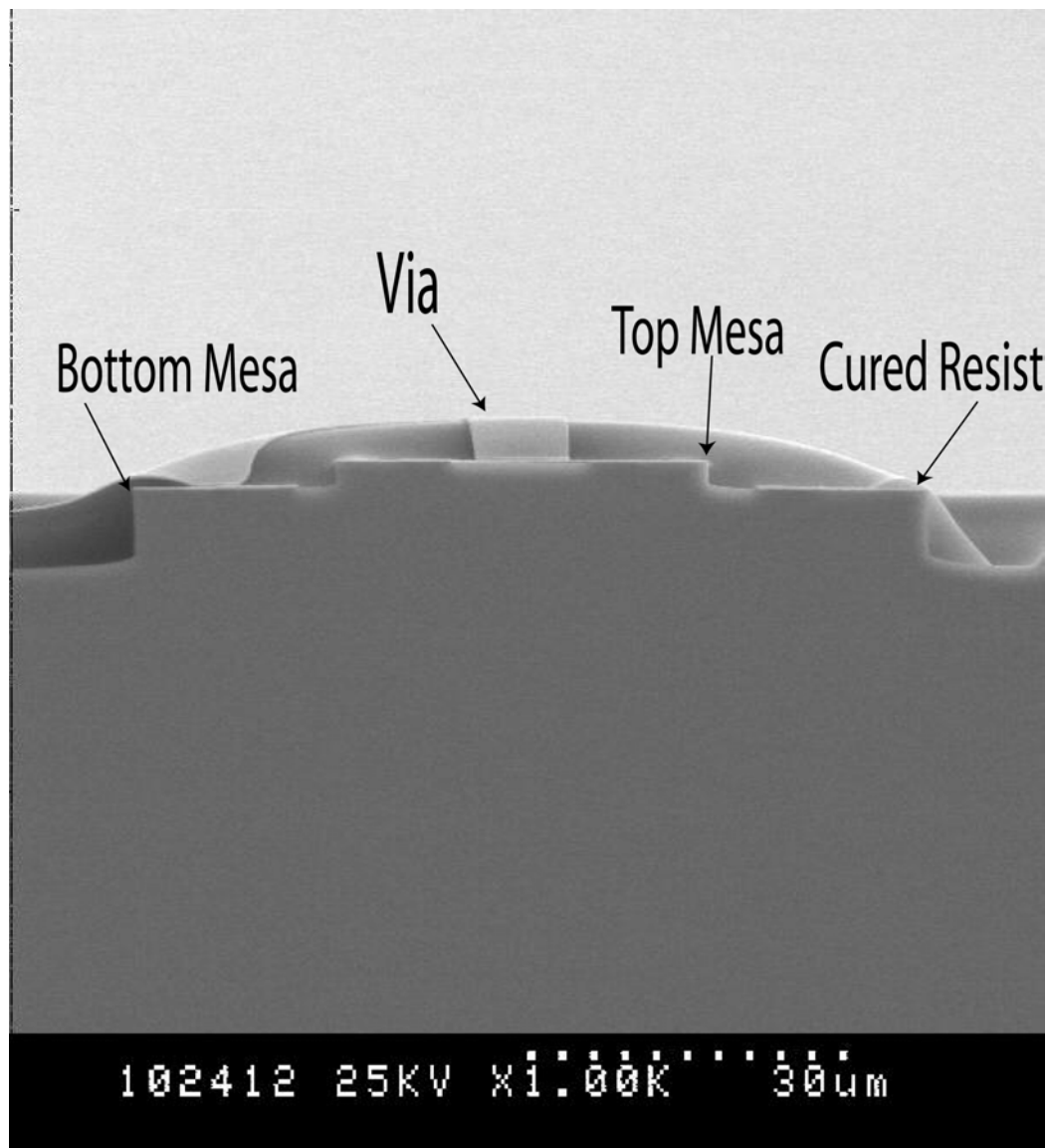


Fig. 5.9. SEM image of VCSEL cross-section and via formation. Cured photoresist microstructures provide excellent platforms for vias and metal blocking structures. A via can be seen making contact to the top mesa contact of the VCSEL.

As describe above, positive resist is patterned and cured to provide insulating 3-dimensional microstructures to support electrical vias and metal optical blocks. Then, thick film bilayer liftoff lithography (Appendix B.4.3) is used to pattern a liftoff mask for

the electrical vias and metal blocking layers. E-beam evaporation (Appendix B.4.4) is used to deposit Ti/Au for via and optical blocking metalization.

One significant problem resulting from the preceding fabrication sequence involves packaging the GaAs chip with wire bonding. Bond pads are formed directly onto the cured photoresist formations. Unfortunately, the bond pads do not adhere well to the cured photoresist and bond pad adhesion difficulties occurred during wire bonding, significantly reducing sensor yield. For next generation devices, it is recommended to use a silicon nitride (Si_3N_4) film for bond pad adhesion and use cured photoresist as a bridge between the optoelectronic contacts and Si_3N_4 films [101].

5.3 CONCLUSIONS

There are some unique fabrication challenges involved in the integrated sensor fabrication. Contacting to the thin GaAs VCSEL intracavity contact layer is a challenge. The deep bottom mesa etch needed to isolate the photodetectors creates highly three dimensional microstructures, which make lithography and via formation a challenge. Cured positive photoresist microstructures prove to be a viable method for enabling via formation and optical isolation blocks between the laser and the photodetector. The processes described here enable the realization of the sensors; however, more process optimization and development is needed to improve yield and decrease integration dimensions.

CHAPTER 6

OPTOELECTRONIC DEVICE CHARACTERIZATION

High performance optoelectronic devices are a prerequisite for high sensitivity fluorescence detection. The initial phase of this research focuses on the fabrication of low-noise photodetectors. Then, these photodetectors are integrated with vertical-cavity surface-emitting lasers (VCSELs) and optical filters to create a complete fluorescence sensor. This chapter evaluates the performance of each optoelectronic component (PIN photodetector, distributed Bragg reflector (DBR) optical filter and VCSEL) of the fluorescence sensor. Then, the following two chapters examine how these components interact to enable fluorescence sensing.

6.1 PHOTODETECTOR MEASUREMENTS

6.1.1 ELECTRICAL MEASUREMENTS

Photodetector dark current causes a host of problems for optical detection, such as shot noise and reduced dynamic range [102]. Dark current is a background signal and can be treated similarly as laser background (see Section 2.3). For the detection of low fluorescence signals, random fluctuations in the dark current background from shot noise can limit sensitivity. The amount of shot noise generated from dark current is given by

$$i_{shot} = \sqrt{2qI_{dark}\Delta f}, \quad (6.1)$$

where q is Coulomb's constant, I_{dark} is the direct-current (DC) value of dark current and Δf is the detection bandwidth. Therefore, especially for high speed applications such as

scanning architectures or fluorescence lifetime sensing, maintaining low dark current is important to reduce shot noise and enable highly sensitive fluorescence detection.

Dark current measurements are performed at 5V reverse bias for circular mesa detectors of varying diameters as shown in Fig. 6.1 [103]. The dark current scales linearly with detector diameter and is measured to be approximately 500fA per μm of detector diameter. These values are extremely low and comparable to some Si detector technologies [102]. This result shows that GaAs photodetector technology is suitable for highly sensitive fluorescence detection. As expected, the fact that the detector dark current scales linearly with detector diameter rather than area suggests that surface states on the detector perimeter are the dominant source of dark current generation. As with most semiconductor devices based on the III-V material system, surface states can be significant and dominate device characteristics [83-85].

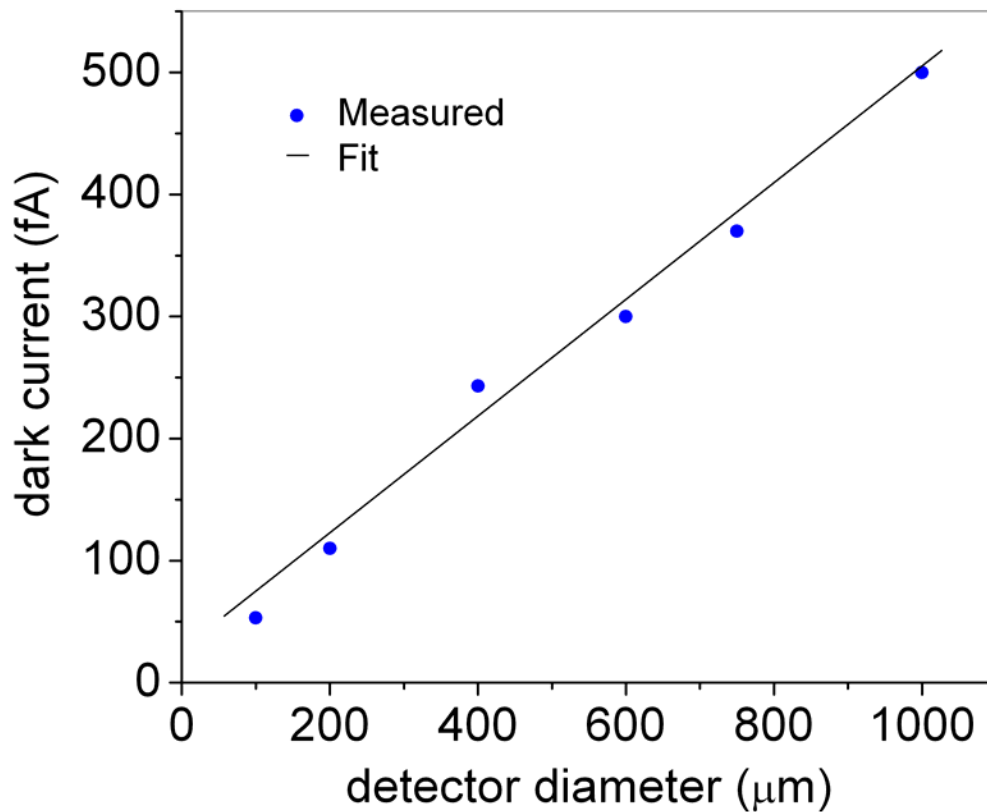


Fig. 6.1. Dark current measured as a function of detector diameter at a detector reverse bias of 5V [103]. Measurements are conducted on low-noise photodetector samples (P222).

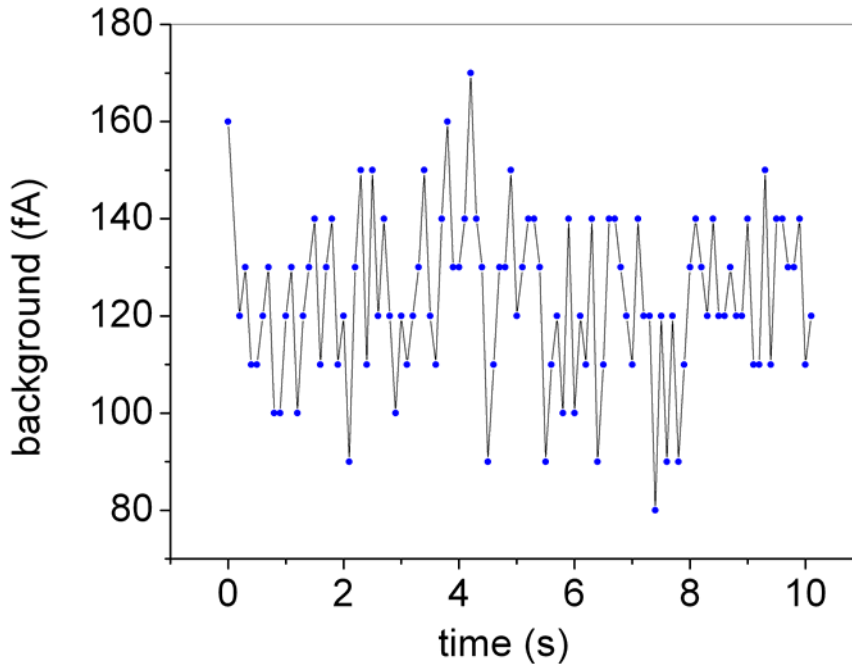


Fig. 6.2. Background current of photodetector at 0V bias. At 5V, the detector shows much greater dark current of 2nA. Measurement is conducted on low-noise photodetector samples (P222).

The measurements reported above are conducted under highly controlled process conditions (see Section 5.1). In practice, the dark current can be much greater than that reported in Fig. 6.1. Epitaxial growth defects, such as oval defects or dislocations, can greatly increase the amount of dark current and be particularly problematic for large area photodetectors because the probability of a defect increases with detector active area [80]. As shown above, surface states dominate the dark current of defect-free photodiodes. Therefore, photodetector dark current is highly dependent on subsequent processing steps. High temperature procedures and oxygen descuming plasmas drastically increase detector dark current. To overcome these difficulties, it is important to note that passivation techniques could be implemented to maintain low detector dark current in a variety of environmental and/or processing conditions [83-85]. In this work, the large detector backgrounds caused by material defects and processing conditions are avoided by operating the photodetectors at 0V reverse bias, where the photodetector dark current should be zero as derived from the ideal diode equation. Fig. 6.2 shows the detector current background ($\approx 120\text{fA}$) at 0V bias. The finite background current is likely due to electronic and/or RF noise from the instrumentation used to measure the diode

current at 0V reverse bias. The same detector shows a dark current of 2nA at 5V reverse bias, so drastic reductions in background can be achieved at 0V operation. Fortunately, as shown in the following section, high detector responsivity can be maintained at 0V operation. However, for high speed applications such as fluorescence lifetime detection, higher reverse bias would be needed to maintain good photodetector responsivity [104,105]. Therefore, maintaining low dark current at high reverse bias would be important for high speed applications.

6.1.2 OPTICAL MEASUREMENTS

A variety of optical measurements are conducted to measure the photodetector and filter performance. Fig. 6.3 shows a schematic of the experimental setup used to measure the optical response of the photodetector/filter modules. A tunable Titanium-Sapphire (Ti:Sapphire) laser beam is focused onto the photodetectors by an objective lens (Numerical Aperture (NA) = 0.1). The photodetector current response is measured with standard probe tips connected to a semiconductor parameter analyzer (Hewlett Packard, 4155B). The Ti:Sapphire output power is monitored with a calibrated silicon photodetector (Newport, 818-SL).

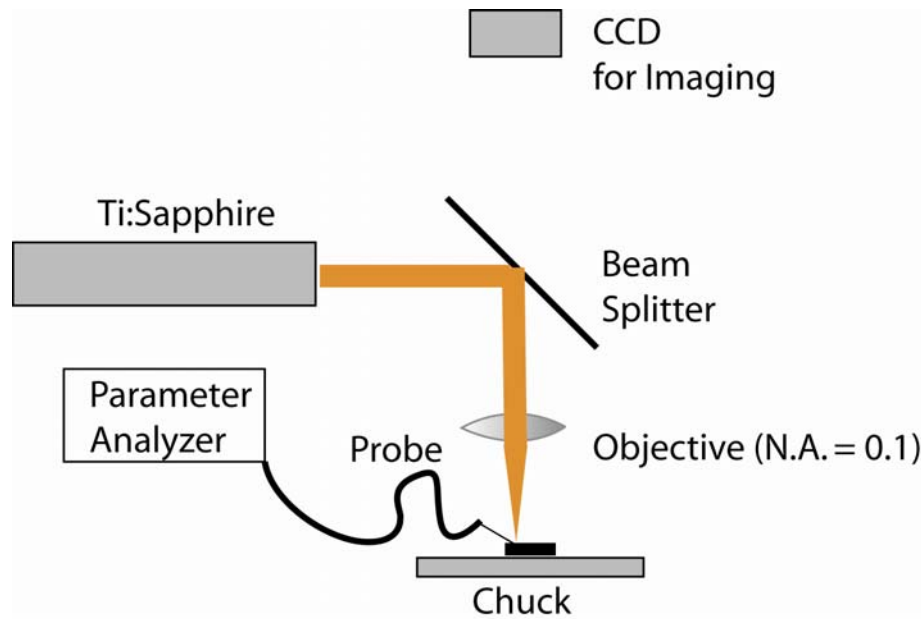


Fig. 6.3. Schematic of experimental setup used to measure the optical characteristics of the photodetectors and optical filters. An optical beam from tunable Ti:Sapphire laser is focused onto the detector/filter.

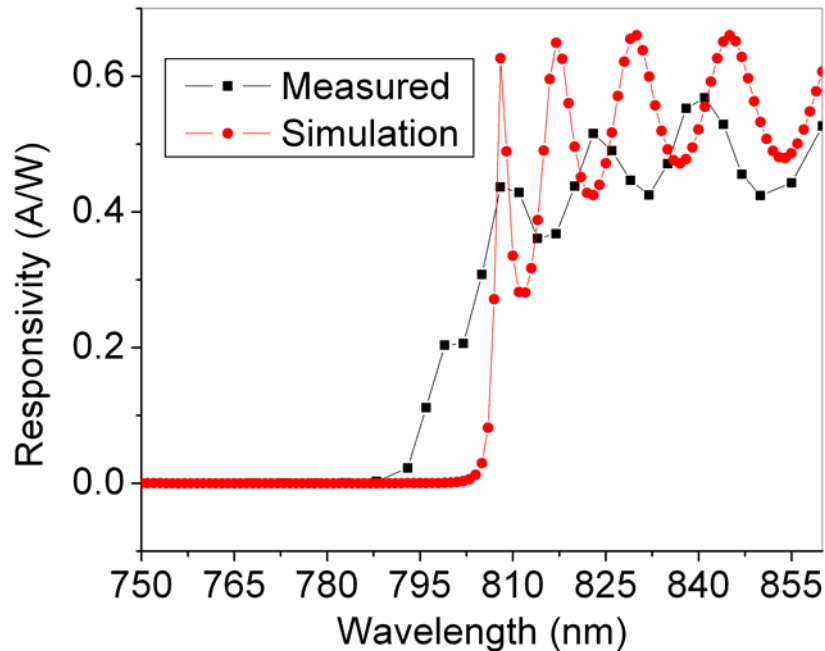


Fig. 6.4. Measured and simulated responsivity of photodetector/filter module (P763-5). Simulation is performed by assuming the photodetector has a QE = 100% over the entire spectral range.

Since fluorescence signals are weak, high photodetector responsivity is required for sensitive detection. The spectral response of the photodetector/filter module is tested as shown in Fig. 6.4. The input laser power used is $10\mu\text{W}$ within a spot size of approximately $20\mu\text{m}$ diameter at the photodetector. The effect of the integrated filter on the photodetector responsivity is clearly observed in the data. It is difficult to measure the photodetector responsivity independently from the optical filter due to the integrated architecture. For wavelengths below the filter cutoff ($\lambda < 795\text{nm}$), the responsivity of the photodetector/filter module is extremely low because the filter rejects these wavelengths. Above the filter cutoff ($\lambda > 795\text{nm}$), the ringing sidelobe behavior of the DBR filter is observed. Over the spectral range from 810-870nm, the average responsivity of the photodetector/filter module is found to be about 0.47 A/W with a peak responsivity of 0.57 A/W at $\lambda = 841\text{nm}$. These values correspond to an average quantum efficiency (QE) of about 70% and a peak QE of 84% at $\lambda = 841\text{nm}$. At $\lambda = 841\text{nm}$, the filter is probably reflecting some power, so the internal QE of the photodetector is probably greater than the measured 84%. A QE of nearly 100% is expected for the heterostructure PIN photodetector with large absorbing region used in this design.

The experimental responsivity from the photodetector/filter module agrees reasonably well with the simulated performance as shown in Fig. 6.4. A thin film optical simulator based on a transfer matrix program is used to determine the theoretical transmission spectrum of the filter [48]. Then, the photodetector is assumed to have a $QE = 100\%$ over the entire spectral range to generate the theoretical responsivity of the photodetector/filter module from the filter transmission simulation. This assumption is realistic as seen from the discussion in the above paragraph. The deviation of the cutoff wavelength and filter sidelobes between the simulation and measurement is due to MOCVD growth errors during the fabrication of the filter structure.

As discussed in Section 6.1.1, operating the detector at 0V reverse bias enables low-noise operation due to negligible background current at 0V. Experimental results show that the responsivity of the photodiode is relatively independent of applied bias as shown in Fig. 6.5. This important result allows for the photodetector to be operated at 0V for low-noise performance without compromising detector responsivity.

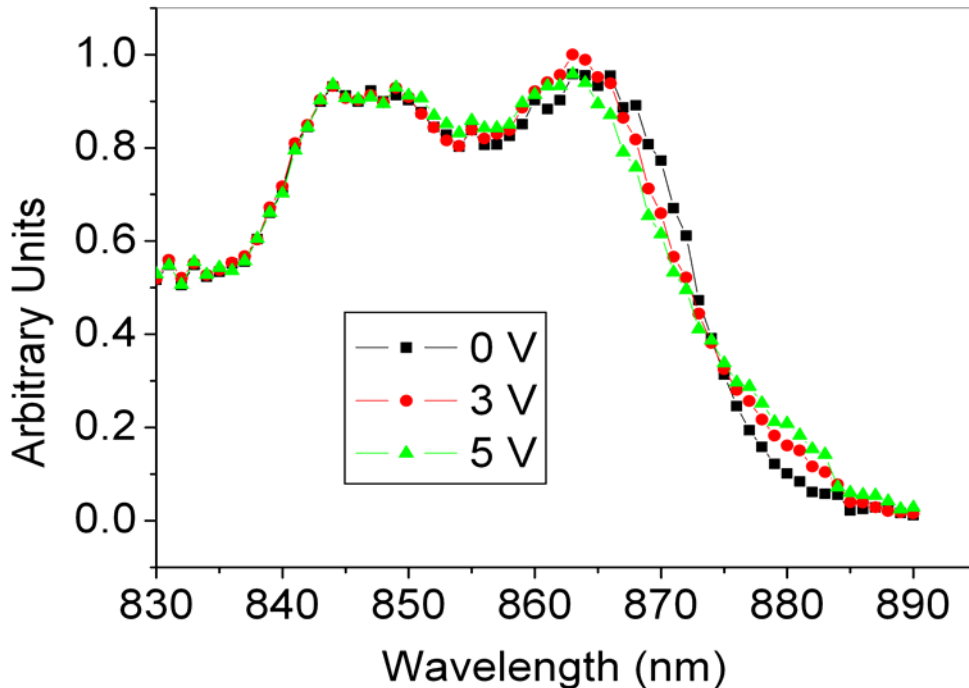


Fig. 6.5. Measured responsivity of photodetector/filter module at 0, 3, and 5V reverse bias. This measurement is conducted on low-noise photodetector sample (P222).

Photodetector linearity is important for fluorescence detection because fluorescence concentration and intensity can vary over many orders of magnitude. To test the photodetector linearity, the photodetector response is measured at $\lambda = 810\text{nm}$ for a variety of input powers as shown in Fig. 6.6 [103]. During this measurement, the photodetector diameter is $200\mu\text{m}$, and the illumination spot diameter is $150\mu\text{m}$. For input powers ranging from 1pW to 1mW , linear detection over nine orders of magnitude is achieved. Saturation effects are not observed, so the dynamic range may even be larger. This dynamic range should be more than adequate for most quantitative fluorescence experiments. In fact, the dynamic range will most likely be limited by the detector readout circuitry instead of the photodetector [102,105,106].

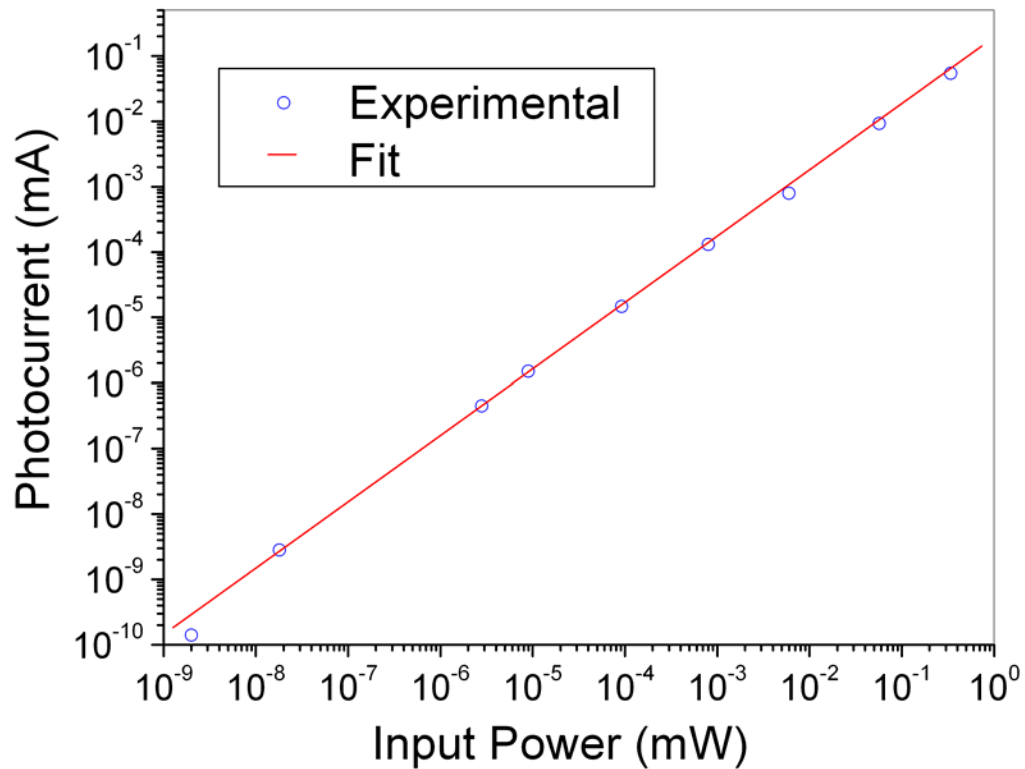


Fig. 6.6. Measurement of photodetector linearity. Measurement is conducted at $\lambda = 810\text{nm}$ and on the low-noise photodetector sample (P222).

6.2 OPTICAL FILTER MEASUREMENTS

6.2.1 ELECTRICAL MEASUREMENTS

As described in Section 4.4.1, the DBR optical filter is used to both reject laser light from reaching the photodetector as well as make electrical contact to the detector active region. Due to the discontinuous valence and conduction band structure, DBRs can add a significant series resistance to the photodetector [107]. This can be problematic because photodetector series resistance will increase the RC time constant and can limit the detection bandwidth. High speed operation would be needed for fluorescence lifetime measurements where over 1 GHz operation may be needed.

A brief characterization of DBR series resistance is conducted. Experiments show that detectors utilizing P-doped DBRs result in much higher values of series resistance than N-doped designs. However, in the future, compositional and dopant grading techniques can be used to reduce the resistance of P-doped DBRs [107,108]. As discussed in Section 4.4.1, a N-doped filter is implemented in the final sensor design due to smaller current crowding effects. With the N-doped filter designs (Sample P222), the detector series resistance is measured to be about 50Ω for a detector with $25\mu\text{m}$ diameter. The series resistance is negligible for detector diameters larger than $100\mu\text{m}$.

6.2.2 OPTICAL MEASUREMENTS

Unfortunately, measuring the filter transmission spectrum independently from the photodetector is difficult due to the integrated architecture. The transmission spectrum of the filter is estimated using the following procedure [109]. As discussed in Section 6.1.2, the responsivity of the photodetector/filter module is measured and it is argued that the photodetector QE is approximately 100%. Due to this 100% QE assumption, the filter performance can be simply extracted from the responsivity data as shown in Fig. 6.7. It is important to note that the measurement requires focusing the input laser beam with an objective lens ($\text{NA} = 0.1$) to a spot onto the photodetector/filter module. Therefore, the

measurement is conducted in a non-collimated regime. This effect is insignificant due to the high optical index of the filter and resulting angular insensitivity, see Section 4.4.2.

Fig. 6.7 shows the theoretical and measured filter transmission spectrum for the sensor samples (P763-5). The filter is designed to have an optical density (OD) greater than 5 or less than 10^{-5} transmission at the excitation wavelength of 773nm. Unfortunately, the filter's optical density is measured to be only OD 3, which causes the sensor to have high levels of laser background from optical reflections. Fortunately, the MBE grown photodetector/filter modules (P222) show much better performance of nearly OD 4 at $\lambda = 773\text{nm}$ (see Fig. 6.7), so much better performance is possible with this technology. However, even the MBE photodetectors/filter modules (P222) do not perform at the theoretically predicted OD 5.

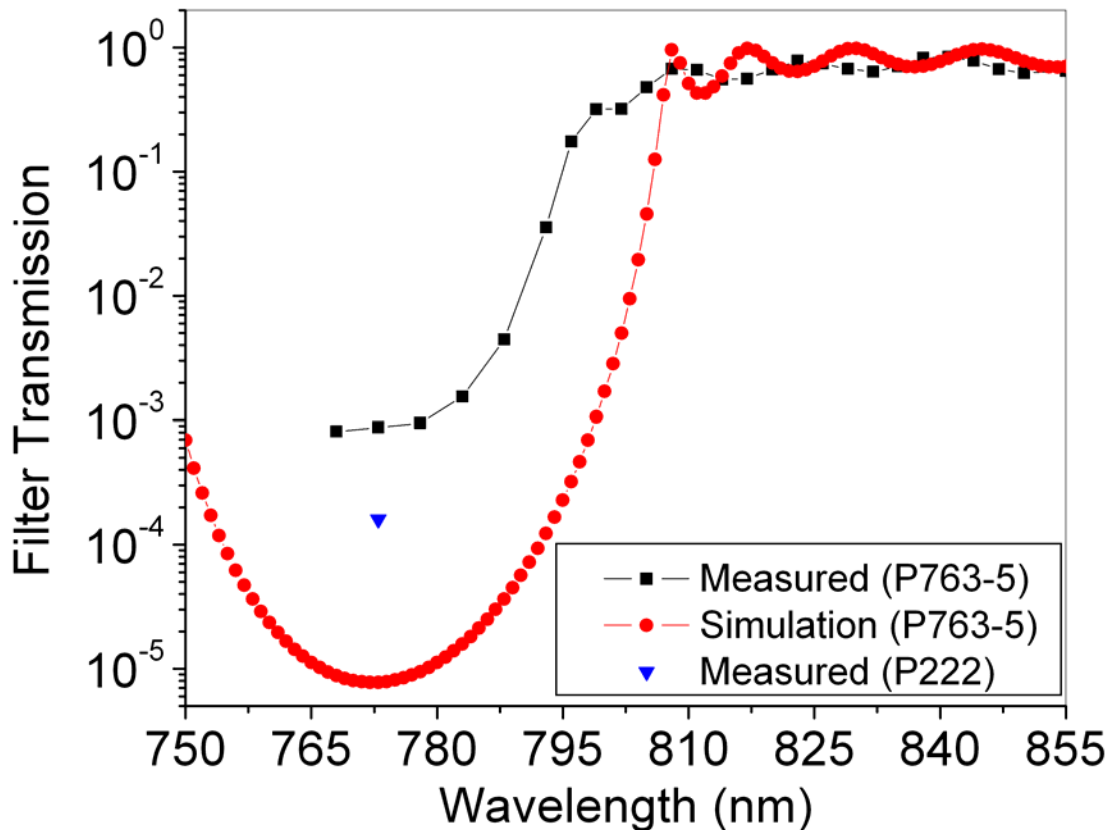


Fig. 6.7. Theoretical and measured transmission spectrum of sensor filter and low-noise photodetector. This measurement is conducted on the sensor sample (P763-5) and low-noise photodetector sample (P222).

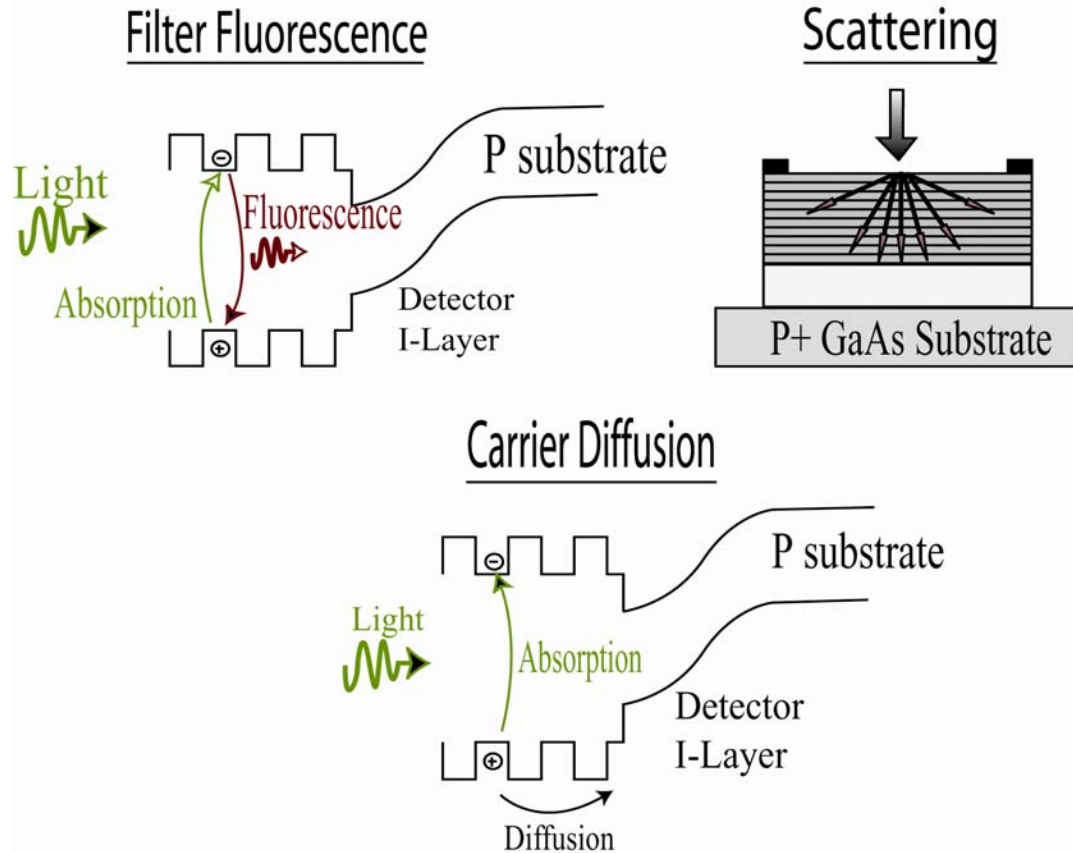


Fig. 6.8. Illustration of three possible mechanisms that degrade filter performance: 1) Filter fluorescence, 2) Optical scattering and 3) Carrier diffusion.

Experiments are currently underway to understand why the filters deviate from theoretical performance. Fig. 6.8 illustrates three possible mechanisms which may be responsible in degrading filter performance. Two of the possible mechanisms, filter fluorescence and carrier diffusion, result from sub-bandgap absorption mechanisms. As discussed in Section 3.2, a small amount of absorption can occur below the material bandgap due to excitons, the Urbach tail, impurity states and/or free carrier absorption [39,43,44]. Some of these absorption processes can result in excited charged carriers. For the case of filter fluorescence, the excited electron-hole pairs recombine at a slightly relaxed energy, releasing a red-shifted photon that can penetrate through the filter and be detected. Also, the broad angular emission of filter fluorescence will be problematic because highly off-normal emission can penetrate through the filter easily. For the carrier diffusion model, the excited holes diffuse into the active junction of the photodetector and create photocurrent. The third possible mechanism that may be responsible for poor

filter performance results from optical scattering. Incident light could be scattered into highly off-normal angles at filter interfaces and penetrate through the filter.

It is believed that filter fluorescence is the mechanism responsible for the poor filter performance. First of all, even with conventional dielectric material systems used for optical filters, filter fluorescence can be problematic and must be considered when designing a filter for a particular application or spectral range. Secondly, the drastic improvement in filter performance in sample P222 compared to the sensor sample (P763-5) suggests that sub-bandgap absorption is responsible for filter degradation. Due to the larger bandgap of sample P222 ($x = 0.3$ or $\lambda_{\text{edge}} = 687\text{nm}$) compared with the sensor sample ($x = 0.25$ or $\lambda_{\text{edge}} = 712\text{nm}$), less sub-bandgap absorption occurs in the P222 filter and this results in drastically improved performance. The influence of sub-bandgap absorption suggests that the filter fluorescence or carrier diffusion models are responsible. The carrier diffusion model is ruled out as a possible mechanism. Carrier diffusion is greatly reduced because the discontinuous valence and conduction band structure of the DBR traps free carriers. Finally, atomic force microscopy (AFM) measurements are conducted to evaluate the filter top surface roughness in order to analyze the effect of optical scattering. Equivalent RMS powers, P_{rms} , of both the P222 and P763-5 samples are between 0.6 - 0.85nm, which show fairly negligible surface roughness compared to the wavelength of light.

As discussed above, filter fluorescence is the likely mechanism responsible for degrading the filter performance. Reducing the sub-bandgap absorption will be effective in reducing the amount of filter fluorescence. As shown above, reducing absorption by increasing the material bandgap from $\lambda_{\text{edge}} = 712\text{nm}$ ($x = 0.25$) to $\lambda_{\text{edge}} = 687\text{nm}$ ($x = 0.3$) improves the filter performance by nearly an order of magnitude. It is believed that further increases in material bandgap will continue to increase filter performance. At an alloy composition of approximately $x = 0.4$, the $\text{Al}_x\text{Ga}_{1-x}\text{As}$ bandgap becomes indirect, which may further reduce filter fluorescence due to less efficient radiative recombination [39,40]. Finally, a large degree of freedom exists in the design of these semiconductor filters and it is believed that $\text{Al}_x\text{Ga}_{1-x}\text{As}$ filter technology can yield much better performance than that reported in Fig. 6.7. However, if future experiments show that

$\text{Al}_x\text{Ga}_{1-x}\text{As}$ can not deliver the desired performance, then conventional dielectric filter technology would be a viable option and can be simply deposited onto the current sensor design [59].

The optoelectronic design described in Section 4.4.1 utilizes the VCSEL DBR as an optical filter for the photodetector. Unfortunately, DBRs show characteristic ringing sidelobe behavior that limits the transmission of the fluorescence signal through the filter and reduces sensitivity. Fig. 6.9 shows the measured transmission spectrum in combination with the emission spectrum of IR-800 (LI-COR, Inc.) in methanol. The fluorescence spectrum is measured with a fluorimeter (Instruments S.A.- FluoroMax-2). Eqn. 2.10 is used to calculate the effective signal transmission through the DBR by normalizing the transmission spectrum against the fluorescence spectrum. It is calculated that only 40% of the fluorescence signal is transmitted through the DBR. Large gains in filter transmission are possible by eliminating the reflectivity sidelobes through simple thin film filter designing (see Section 4.4.2).

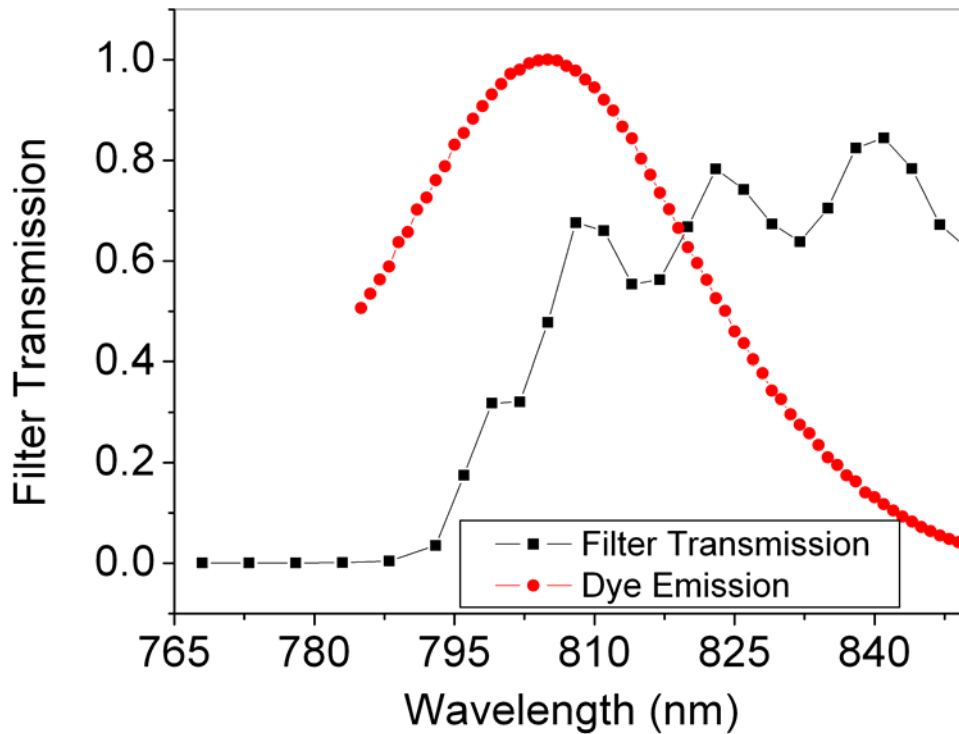


Fig. 6.9. Measured filter transmission spectrum in combination with measured fluorescence spectrum of IR-800 dye (LI-COR Inc.) in methanol. Filter measurement is conducted on sensor sample (P763-5).

6.3 VCSEL MEASUREMENTS

6.3.1 LIV MEASUREMENTS

High performance lasers are a prerequisite for high sensitivity fluorescence detection. The VCSELs used for the sensor (sample P763-5) are characterized and prove to be excellent emission sources for laser-induced fluorescence (LIF) detection. A simple experimental setup is used to characterize the output power-current-voltage (LIV) performance of the VCSELs and involves a probe station, silicon photodiode (Newport, 818-SL), laser driver (ILX, 3744), InGaAs photodetector (Thorlabs, PDA400) and computer interface. The silicon photodiode is used to calibrate output power-current (LI) data generated from the computer controlled InGaAs photodiode.

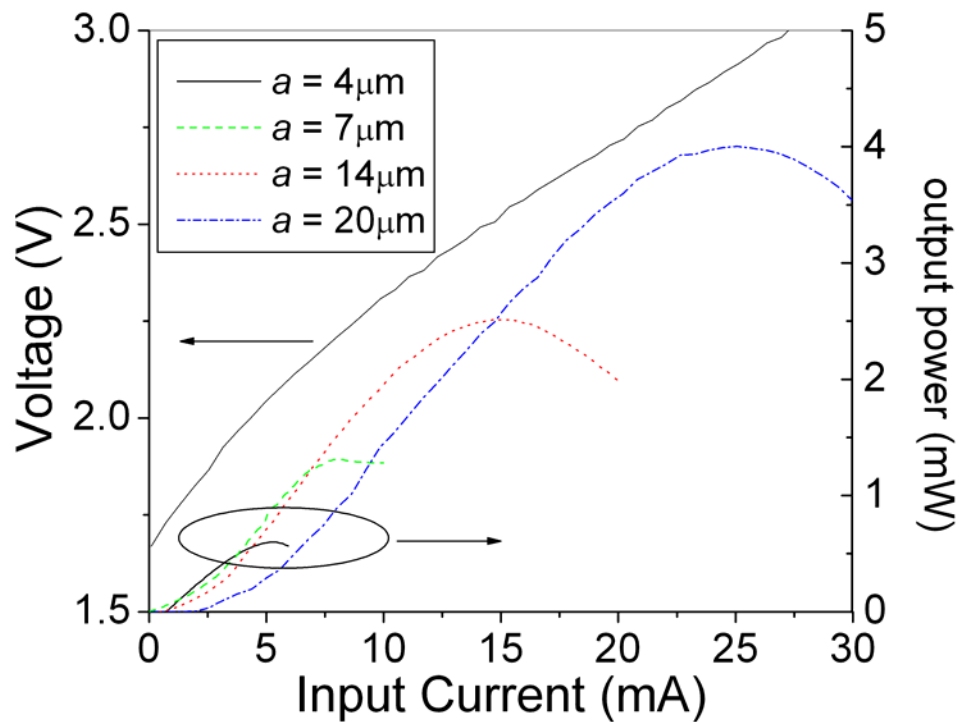


Fig. 6.10. CW LIV characteristics of 773nm VCSELs with oxide apertures of 4, 7, 14 and 20 μm . The current-voltage (IV) curve is shown for the 20 μm aperture VCSEL. Data is collected from the sensor samples (P763-5).

Fig. 6.10 shows power-current characteristics for continuous-wave (CW) operation at 20C for VCSELs with a wavelength of 773nm and oxidation aperture diameters of 4, 7,

14 and 20 μm [78,110]. The VCSELs show characteristic output power roll-off as the gain spectrum is thermally misaligned to the resonant cavity wavelength with increasing input current [47,87].

a	I_{th}	J_{th}	Max. Power	Diff. Eff.	Max. Wallplug	R_{series}
4 μm	0.8 mA	6400 mA/cm ²	0.6 mW	10.5%	12% @ 0.3 mA	210 Ω
7 μm	1.6 mA	4200 mA/cm ²	1.3 mW	16%	5% @ 5.5 mA	55 Ω
14 μm	2.2 mA	1400 mA/cm ²	2.5 mW	16%	7.7% @ 8.5 mA	47 Ω
20 μm	4.1 mA	1300 mA/cm ²	4.0 mW	15%	6.8% @ 17.5mA	38 Ω

Table 6.1. Typical VCSEL operational parameters for oxide diameters of $a = 4, 7, 14$ and $20\mu\text{m}$. Data collected from sensor samples (P763-5).

Typical VCSEL operational parameters for varying oxide diameters, denoted as a , can be found in Table 6.1. The threshold current increases with aperture diameter from 0.8mA ($a = 4\mu\text{m}$) to 4.1mA ($a = 20\mu\text{m}$). These reported values of threshold are determined by using a linear fit of above threshold operation [46]. The actual values of threshold are lower due to the slow turn-on characteristics that are typical of multimode VCSELs (see Figs. 6.10 and 7.4). The threshold current densities decrease from 640A $\cdot\text{cm}^{-2}$ ($a=4\mu\text{m}$) to 1300A $\cdot\text{cm}^{-2}$ ($a=20\mu\text{m}$) with increasing oxide apertures due to decreased optical losses [47,92]. The differential quantum efficiency is about 15% for the large aperture designs. The smaller aperture design has a smaller differential efficiency due to the increased optical losses and less optimal modal overlap with the gain volume [47]. With operating voltages between 2 and 3V, the differential resistances decrease from 55 Ω to 38 Ω for aperture diameters of 7 to 20 μm , respectively. The small aperture design shows a much greater resistance of 210 Ω . The maximum output power scales with aperture diameter from 0.6 to 4.0mW for aperture diameters of 4 and 20 μm ,

respectively. The results reported here are in good agreement with values reported in the literature for VCSELs operating in this spectral range [90,92]. Most importantly, these power levels provide sufficient optical power to achieve high sensitivity fluorescence sensing.

6.3.2 MODAL AND SPECTRAL CHARACTERIZATION

Single-mode (fundamental TEM_{00}) VCSELs are observed for the small aperture design, $a = 4\mu\text{m}$. VCSELs with oxide apertures greater than $7\mu\text{m}$ lase in multiple transverse modes. Fig. 6.11 shows near field images for a single-mode and multimode VCSEL. These images are captured with a Spiricon camera (Model #TC-1122). The single-mode VCSEL shows a fundamental Gaussian shape. Whereas, for the multimode VCSEL, the observed peaks in the optical intensity distribution are indicative of multiple transverse modes. In most quantitative fluorescence sensing applications, extreme resolution is not required. Therefore, single-mode operation does not offer an obvious advantage over multimode operation. However, if low divergence is required, then single-mode operation can offer significant advantages as discussed below.

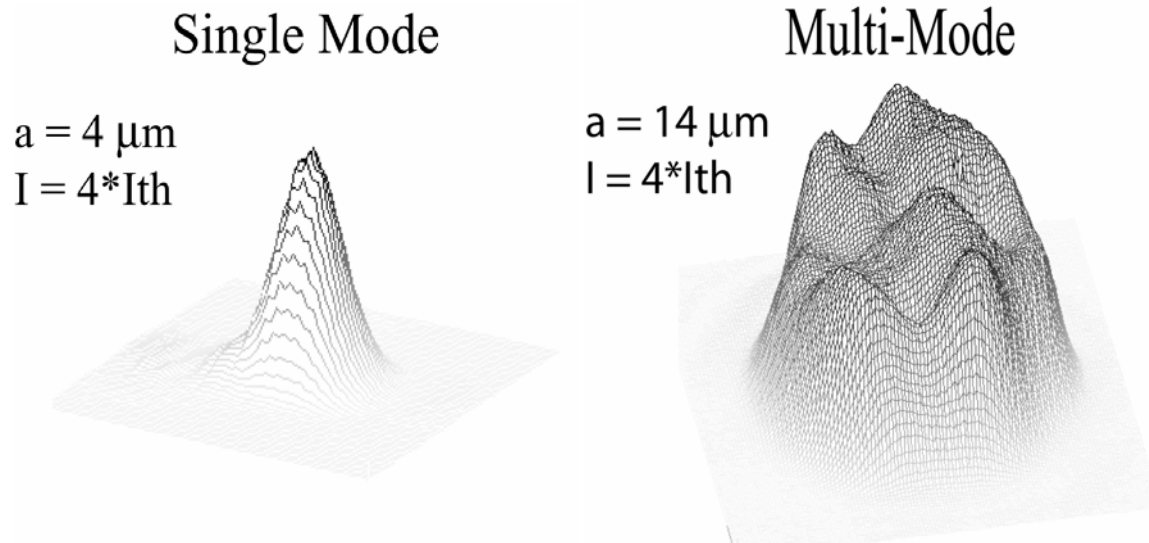


Fig 6.11. Near-field optical images of single-mode and multimode VCSELs. (Left) Single mode VCSEL with oxide aperture of $a = 4\mu\text{m}$ and $I_{drive} = 4 * I_{th}$. (Right) Multimode VCSEL with oxide aperture of $a = 14\mu\text{m}$ and $I_{drive} = 4 * I_{th}$.

Lasers that show broad spectral characteristics can create significant problems due to the laser emission spectrally overlapping the fluorescence emission. When this spectral overlapping occurs, spectral filtration is not possible and large laser background is created. Multiple longitudinal modes can cause significant spectral broadening of laser emission and be problematic for fluorescence sensing [47]. Fig. 6.12 shows the spectrum of a large aperture multimode ($a = 14 \mu\text{m}$) VCSEL driven well above threshold. This spectrum shows the absence of multiple longitudinal modes. Due to the short cavity length of VCSELs and resulting broad spectral spacing between longitudinal modes, VCSELs lase in only one longitudinal mode and show relatively narrow spectral characteristics [47].

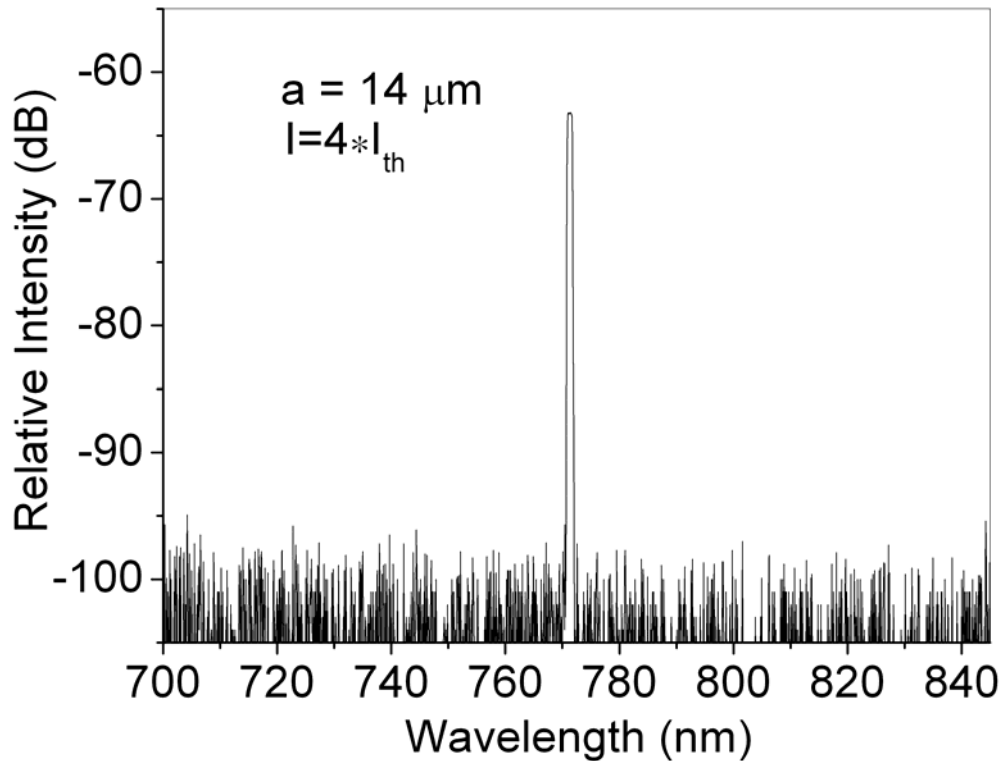


Fig 6.12. Measured optical spectrum of 14 μm aperture VCSEL driven at $I_{\text{drive}} = 4 * I_{\text{th}}$. The figure shows that the VCSEL lases in one longitudinal mode.

The linewidth of the fabricated VCSELs is limited by broadening due to multiple transverse modes. Different transverse modes lase in slightly different spectral regions [45]. Fig. 6.13 shows the optical spectrum of a 14 μm aperture laser as a function of laser

drive current. Near laser threshold, the single spectral peak shows that the VCSEL lases in only one transverse mode. The multiple spectral peaks for above threshold operation show that the VCSEL transitions to multimode operation. In addition, the emission spectra shifts towards slightly longer wavelengths as the VCSEL is driven with larger input current. This red shift is caused by the change in cavity resonant wavelength from thermally induced optical index changes [87]. The linewidths shown in Fig. 6.13 are sufficiently narrow ($\Delta\lambda < 1\text{nm}$) to avoid overlapping with the fluorescence emission spectra and enable high sensitivity fluorescence detection.

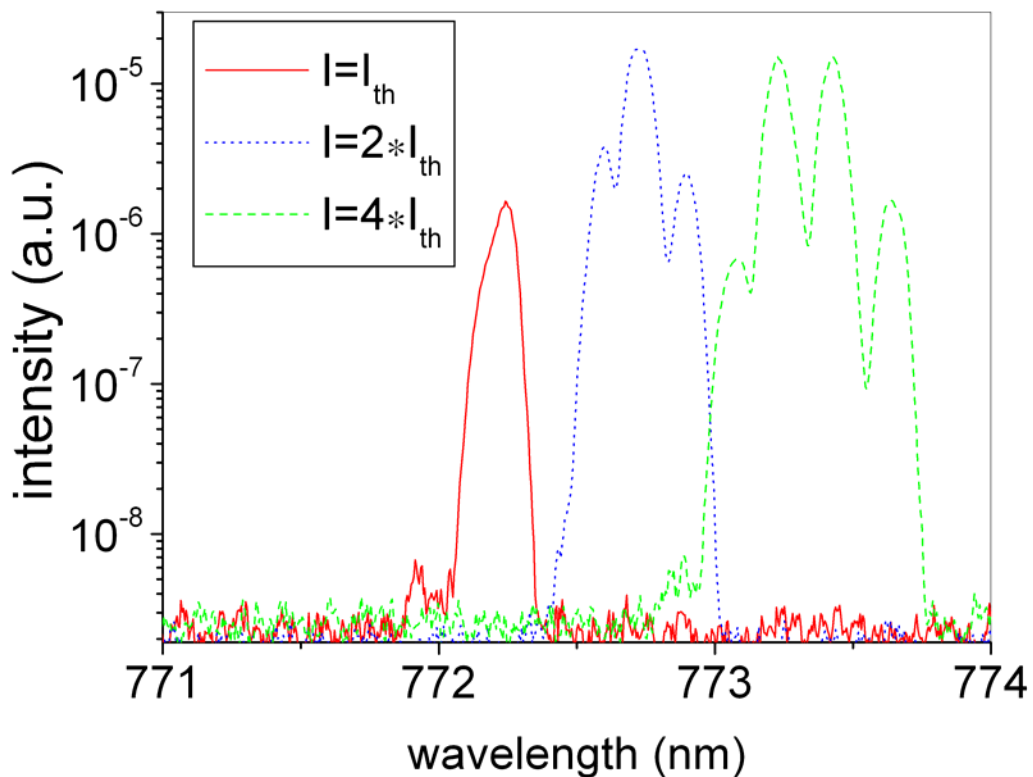


Fig. 6.13. Measured power dependent emission spectrum for a VCSEL with aperture of $14\mu\text{m}$. The VCSEL transitions from single-mode to multimode operation with increasing input current.

Far-field laser divergence is another important parameter in designing an optimized integrated sensor. For most applications, it is desirable to have a small divergence angle. Sources with a broad distribution of divergence angles typically decrease spatial filtration because the light will fill a larger percentage of the optical system. Also, as shown in Section 4.4.2, spectral filtering of light over a wide angular range is challenging due to

the angular dependence of interference filters. The VCSEL far-field divergence is measured with a goniometer and silicon photodiode (Newport, 818-SL). The divergence of the single-mode VCSEL is 14° full-width at half-maximum (FWHM), which agrees well with standard single-mode Gaussian theory. The $20\mu\text{m}$ aperture also shows a divergence of 14° FWHM as shown in Fig. 6.14. The 7 and $14\mu\text{m}$ aperture VCSELs show larger divergences of about 20° FWHM. As expected, the multimode VCSELs deviate significantly from the divergence calculated using single mode Gaussian theory [45]. For the multimode VCSELs, the far-field divergence pattern is toroidal as shown in Fig. 6.14.

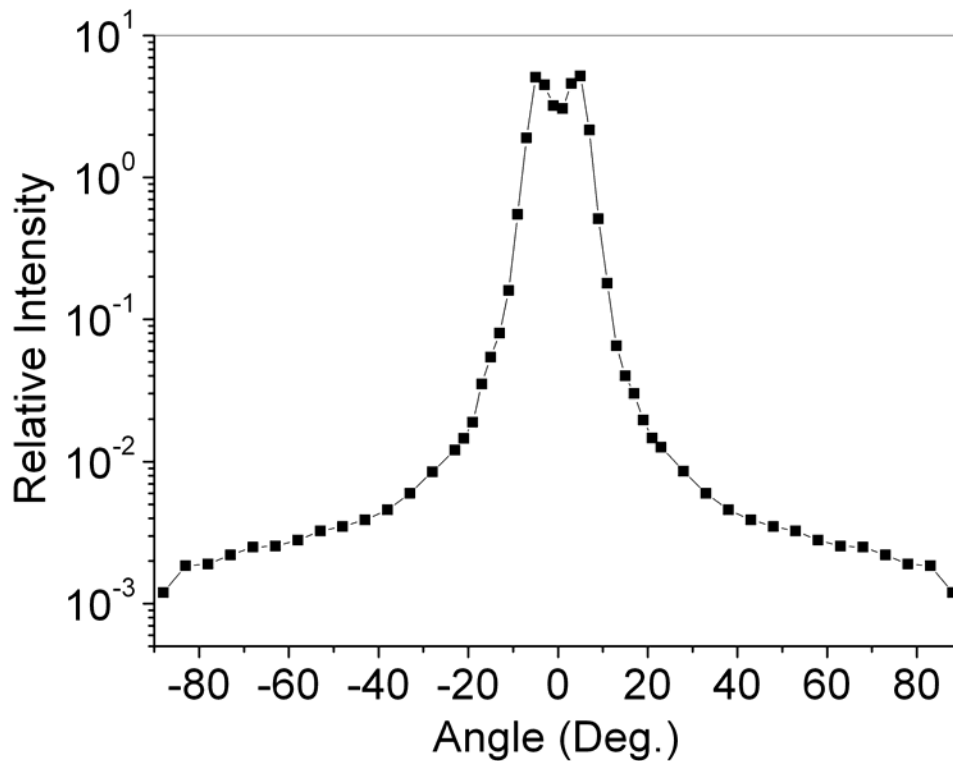


Fig. 6.14. Far-field divergence of $20\mu\text{m}$ aperture VCSEL.

6.4 CONCLUSIONS

This chapter is devoted to the optoelectronic characterization of the individual devices (PIN photodetector, DBR optical filter, and VCSEL) used in the design of the integrated fluorescence sensor. High quality photodetectors are achieved that show low dark current, linear detection and high quantum efficiency. Unfortunately, the integrated semiconductor filters do not perform as theory predicts and limit the sensor sensitivity due to the low rejection of reflected laser light as discussed in the following sections. Finally, high-quality VCSELs are achieved that show high-power operation and narrow spectral characteristics, which are ideal for fluorescence sensing.

CHAPTER 7

LASER BACKGROUND ANALYSIS

In the previous chapter, the individual optoelectronic components (vertical-cavity surface-emitting laser (VCSEL), PIN photodetector and optical filter) that form the basis of the integrated fluorescence sensor are characterized. This chapter examines the interaction of these individual components and how this interaction creates laser background. This study of laser background is important because laser background limits sensor sensitivity as found in Chapter 8. The characterization and understanding of laser background will enable and motivate future design modifications to increase the sensor sensitivity.

7.1 SOURCES OF LASER BACKGROUND

As described in Section 2.3, laser background limits the sensitivity of most fluorescence sensing systems. In the integrated fluorescence sensors studied in this work, three sources of laser background have been identified and are illustrated in Fig. 7.1 [109,111,112]. Spontaneous emission emitted from the side of the VCSEL can directly illuminate the detector sidewall and be detected. This source has been labeled an internal source of laser background because the direct incidence of spontaneous emission acts independently of the environment outside of the optoelectronic sensor. In essence, this internal source of laser background is a more fundamental limitation caused by the close integration of the laser and photodetector. The final two sources are caused by reflection or scattering of laser radiation (spontaneous emission or laser beam) from optical interfaces located above the sensor. These reflections are reduced by the optical filter but nonetheless can create significant background, especially if the filter is performing poorly. Since these sources are caused by reflections outside of the optoelectronic components, they are labeled external sources of laser background.

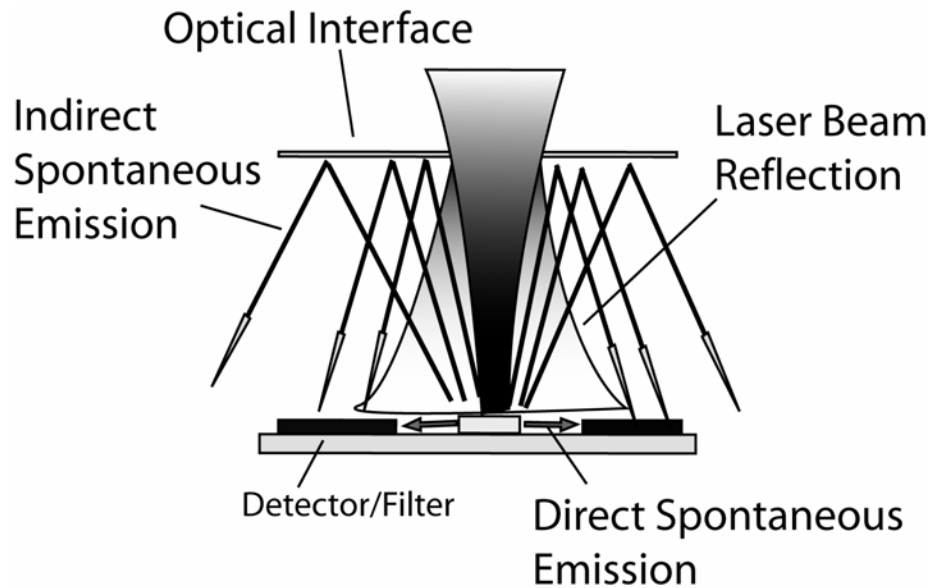


Fig. 7.1. Schematic of the three sources of laser background: 1) Direct spontaneous emission (Internal Source) 2) Indirect spontaneous emission (External) and 3) laser beam reflection (External).

7.2 DIRECT INCIDENCE OF SPONTANEOUS EMISSION

7.2.1 CHARACTERIZATION

All practical lasers are sources of spontaneous emission [45]. Before the laser's threshold current is reached, a laser essentially behaves like a light emitting diode (LED), emitting spontaneous emission in all directions [113,114]. Once the threshold current is reached, additional input current drives the coherent laser beam. The resulting laser beam is superimposed on the background spontaneous emission. Unfortunately, spontaneous emission can be disastrous for miniature fluorescence sensors because it is difficult to filter. Spontaneous emission emits into a broad angular distribution (i.e. like a point source) and is spectrally broad. Broad angular and spectral characteristics are problematic because interferometric filters are optimized for a particular angle and wavelength as discussed in Sections 3.3.2 and 4.4.2. In addition, spectrally broad sources can spectrally overlap the fluorescence emission, making spectral filtration impossible. In the sensor design discussed in this thesis, spontaneous emission can create

overwhelming background levels because it can avoid the interference filter and directly illuminate the detector active region as shown in Fig. 7.2 [115].

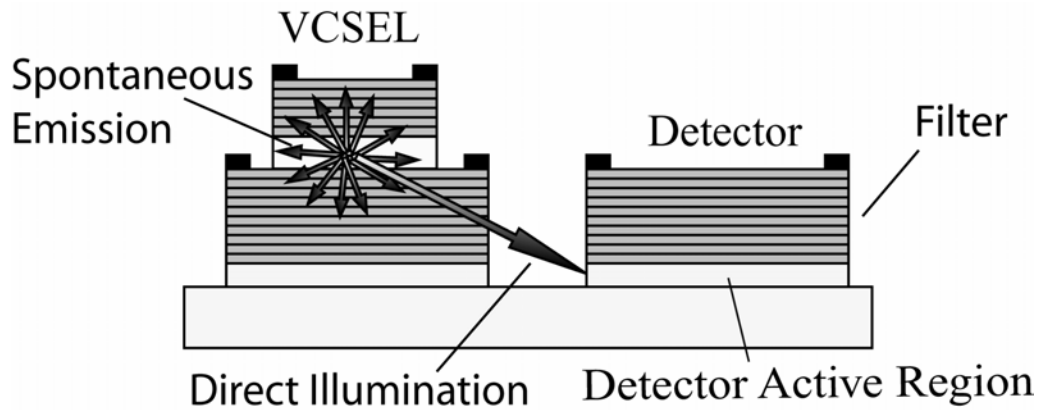


Fig. 7.2. Illustration of how spontaneous emission can directly illuminate the detector active region. Direct illumination avoids the filter and causes an overwhelming laser background.

Fig. 7.3 shows an optical image of the VCSEL during lasing and parasitic spontaneous emission. The image is captured with a Spiricon camera (Model #TC-1122). The ring patterns of spontaneous emission result from scattering at the edge of the VCSEL's circular top mesa. Multiple spontaneous emission rings result from the varying top mesa diameter as shown in Fig. 5.8. The coherent laser beam can be seen in the center of the top mesa.

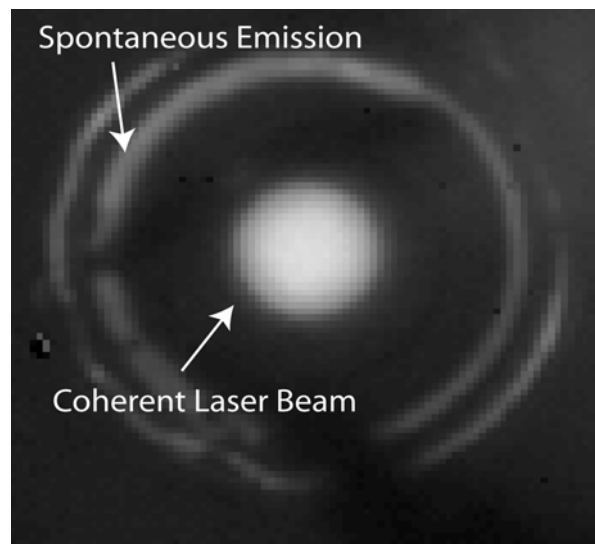


Fig. 7.3. Near-field optical image of VCSEL emission. Spontaneous emission scatters from the top mesa edges, creating ring shaped patterns.

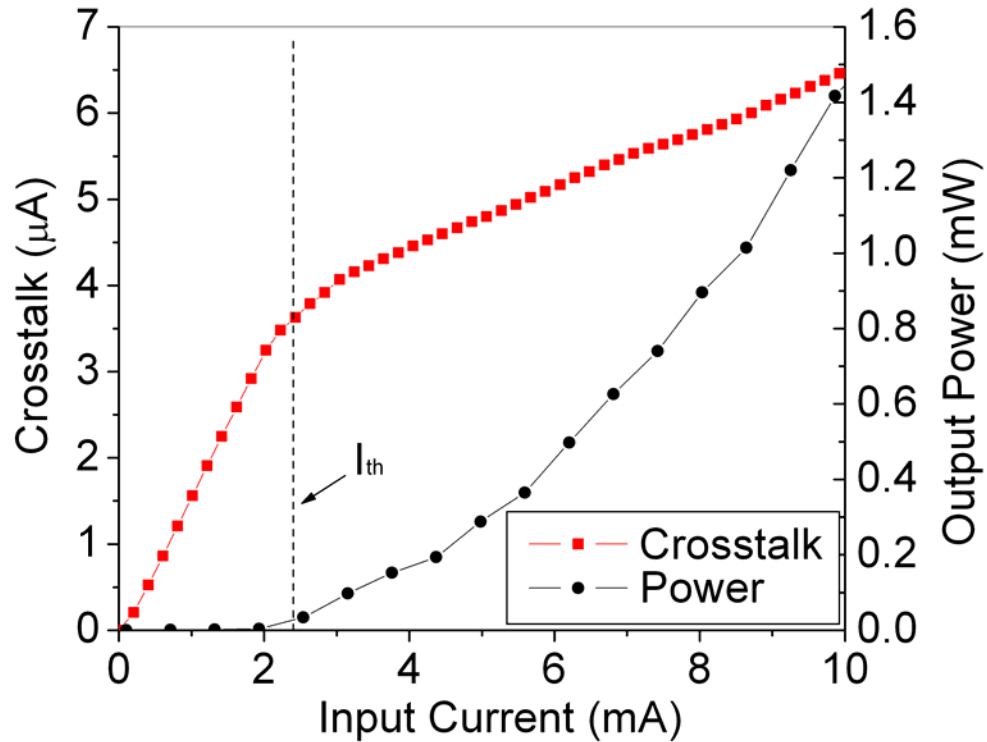


Fig. 7.4. Measured laser background in a proximity architecture with no optical interface located above the sensor. Corresponding VCSEL L-I characteristics are also provided.

For the proximity sensing architecture, Fig. 7.4 plots the measured laser background as a function of laser input current with corresponding output power-current (L-I) characteristics of the laser. The measurement is conducted with no optical interface above the sensor so that the direct illumination of spontaneous emission can be analyzed independently from external reflections. For a sensor with a $20\mu\text{m}$ oxide aperture VCSEL and input drive current of 10mA (1.5mW operation), the measured laser background is $6.5\mu\text{A}$. This marks a total optical system filtration of less than 10^3 . This large laser background relative to the laser power reduces the sensor sensitivity well below practical levels, see Section 2.3.2. It is interesting to note the kink in the laser background curve shown in Fig. 7.4. In theory, after laser threshold, the spontaneous emission does not increase because all additional input current couples into the lasing mode [45,46]. However, in practice, not all input current is converted to coherent lasing radiation and the spontaneous emission does increase after threshold, but at a smaller rate when compared to below threshold operation. As a result, a kink is observed at the

threshold point of the laser and supports the theory that the laser background is caused by spontaneous emission emitted from the VCSEL side. As expected from the preceding argument, the kink in the L-I curve shows excellent agreement to the kink in laser background as shown in Fig. 7.4.

Laser background levels are also measured for sensors in an imaging architecture (See Figure 4.2). The detector diameter used in this experiment is $20\mu\text{m}$, and the laser is driven at an output power of 1mW . Fig 7.5 shows the laser background plotted against separation distance between the laser and small area photodetector without an optical interface in front of the sensor. The laser background is 4nA for a separation distance of $250\mu\text{m}$. It is interesting to note that this value is much smaller than that reported for the proximity sensor above. The imaging architecture shows much less laser background due to the use of a small area photodetector and larger separation between the excitation source and photodetector. The measured data follows a $1/r^2$ dependence, which is expected for a point source producing spontaneous emission.

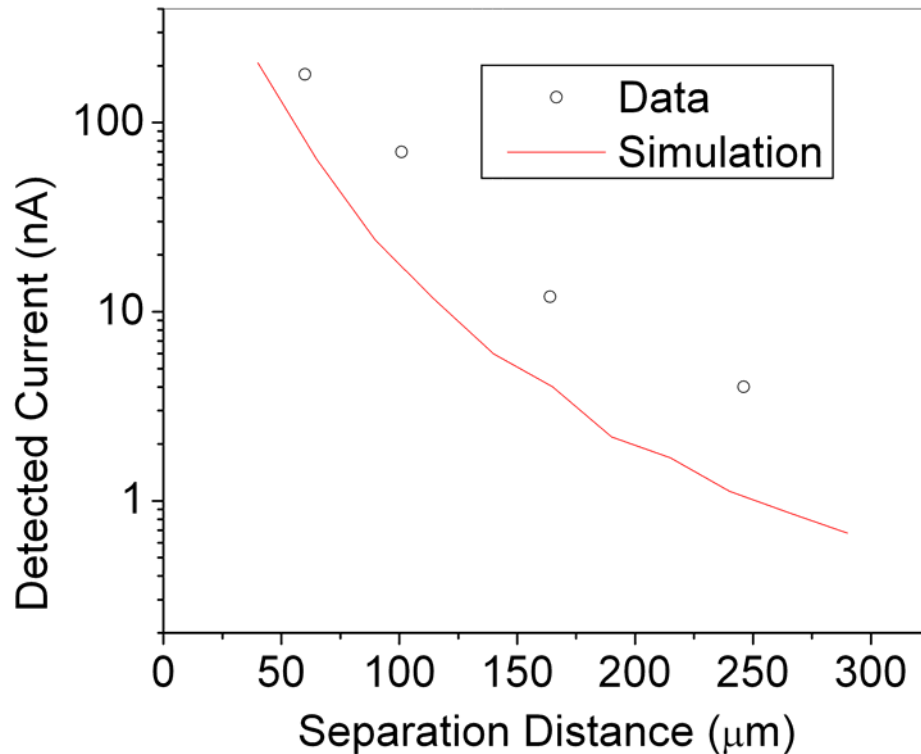


Fig. 7.5. Measured and simulated laser background in an imaging configuration as a function of the distance between the VCSEL and photodetector. Simulation conducted with ASAP.

A non-sequential ray tracing program called ASAP (Breault Research Organization, Tucson, AZ) is used to model the experimental results shown in Fig. 7.5. The angular divergence data of the VCSEL is measured, see Fig. 6.14, and inputted into the optical simulator to model the laser emission. Then, the photodetector is modeled as a simple absorbing region equal to the dimensions of the photodetector active region. The simulation matches experiment to within a factor of 5, which is reasonable. Simulating laser background levels is difficult due to the complex optical environment within the sensor and unknown optical scattering coefficients from the various sensor surfaces. The success of this simulation lends hope that laser background levels can be modeled to within a reasonable degree and be useful for sensor designing/optimization.

7.2.2 METAL BLOCKING WALLS

As discussed above, a large laser background response results from spontaneous emission from the VCSEL side and drastically hinders the practical application of the sensor. Therefore, a design modification is proposed to reduce the laser background by constructing optical blocks between the VCSEL and photodetector. Metal blocking walls are fabricated as described in Section 5.2.2 and prove to significantly reduce laser background levels as discussed below.

Two metal blocking wall structures are fabricated, as shown in Fig. 7.6. The original metal blocking wall is approximately $1.0\mu\text{m}$ taller than the photodetector and about $2.5\mu\text{m}$ less than the top facet of the laser [109,111,112]. This metal blocking wall is not tall enough to eliminate all direct lines of sight between the photodetector and VCSEL. Therefore, an improved wall is constructed to eliminate all possible optical paths between the laser and photodetector by simply increasing the height as shown in Fig. 7.6.

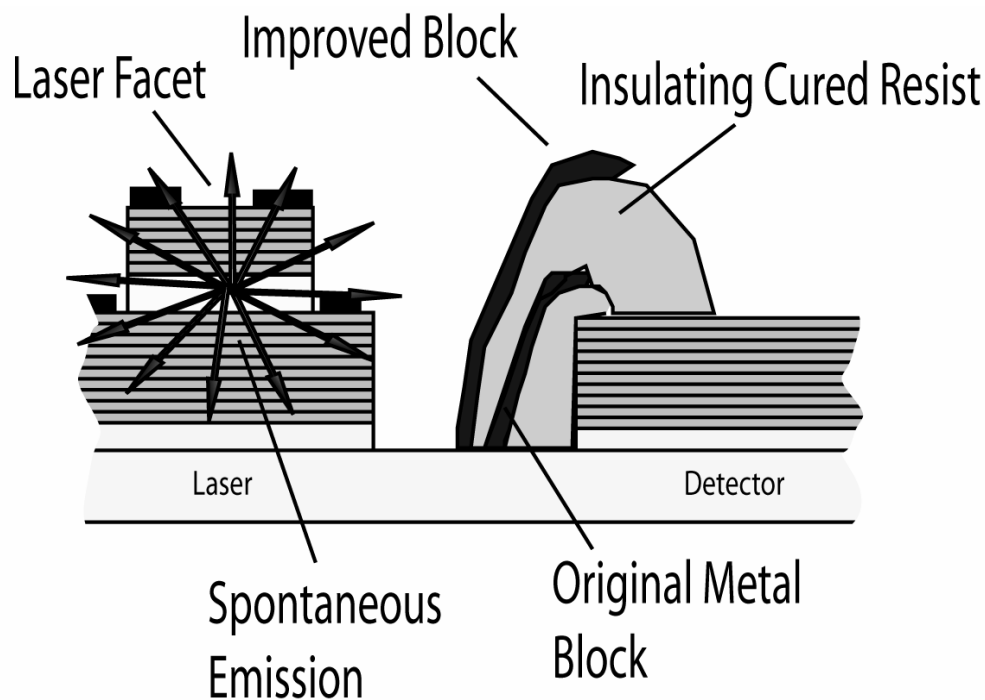


Fig. 7.6. Schematic of metal blocking layers to prevent spontaneous emission from directly illuminating the photodetector. An improved metal blocking layer is fabricated to eliminate all optical paths between the VCSEL and photodetector.

The metal blocking walls drastically reduce the laser background caused by direct incidence of spontaneous emission as shown in Fig. 7.7. The original metal blocking wall reduces the background by a factor of 500. The improved blocking wall further reduces the background by a factor of 100. With the improved blocking walls, the direct coupling between the laser and photodetector is reduced to 700pW at an optical output power of 2mW from the laser. This marks an internal isolation of 3×10^6 between the VCSEL and photodetector [112]. This result is important because it proves that these optoelectronic components can be integrated in close proximity while maintaining adequate internal optical isolation for sensitive fluorescence sensing. In the future, further reduction of internal laser background may be possible. The source of the remaining background has not been determined and may result from a variety of sources, such as pinholes in the metal blocking walls or electrical coupling through the GaAs substrate.

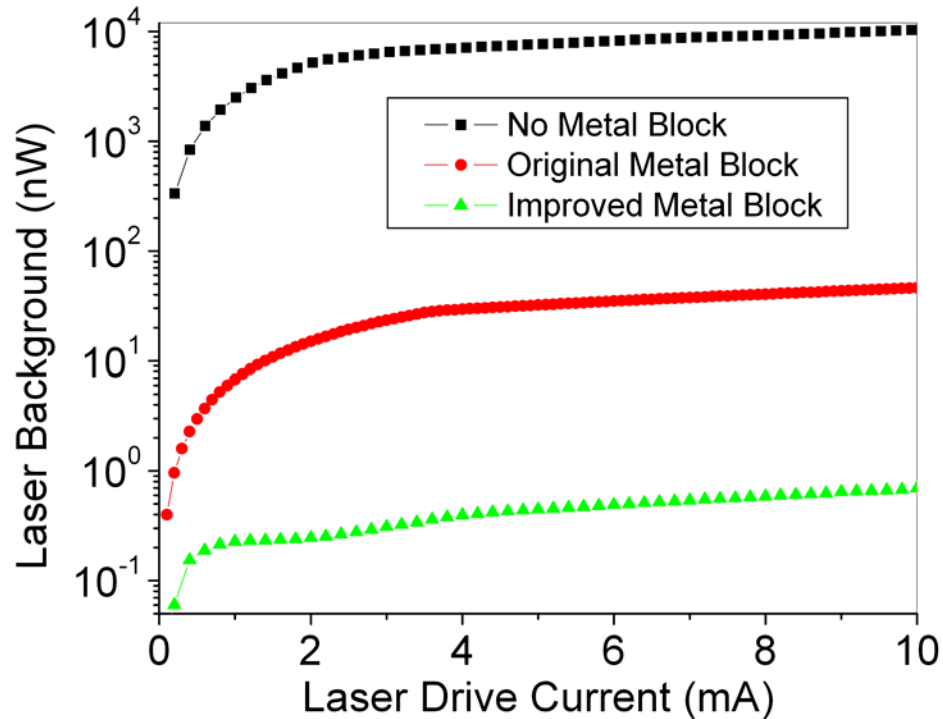


Fig. 7.7. Measured laser background as a function of laser drive current. Metal blocking layers significantly reduce the laser background from spontaneous emission. Sensor is in a proximity architecture.

7.3 LASER BACKGROUND FROM REFLECTIONS

7.3.1 INTRODUCTION

With the metal blocking walls in place, external sources (i.e. reflections) of laser background dominate over internal sources (i.e. direct incidence of spontaneous emission) [112]. For example, with a flat glass coverslip (150 μ m thickness) placed 1mm above the sensor, a dramatic increase in background occurs, as shown in Fig. 7.8. It is clear that the sensor is very susceptible to back reflected laser emission. The relatively large backgrounds due to reflections result from poor filter performance. Better optical filters are needed to reduce the laser background caused by reflections. Nonetheless, it is useful to study this dominant source of laser background because careful study illuminates how spectral and spatial filtration can be employed in future designs towards the reduction of laser background and increases in sensor sensitivity.

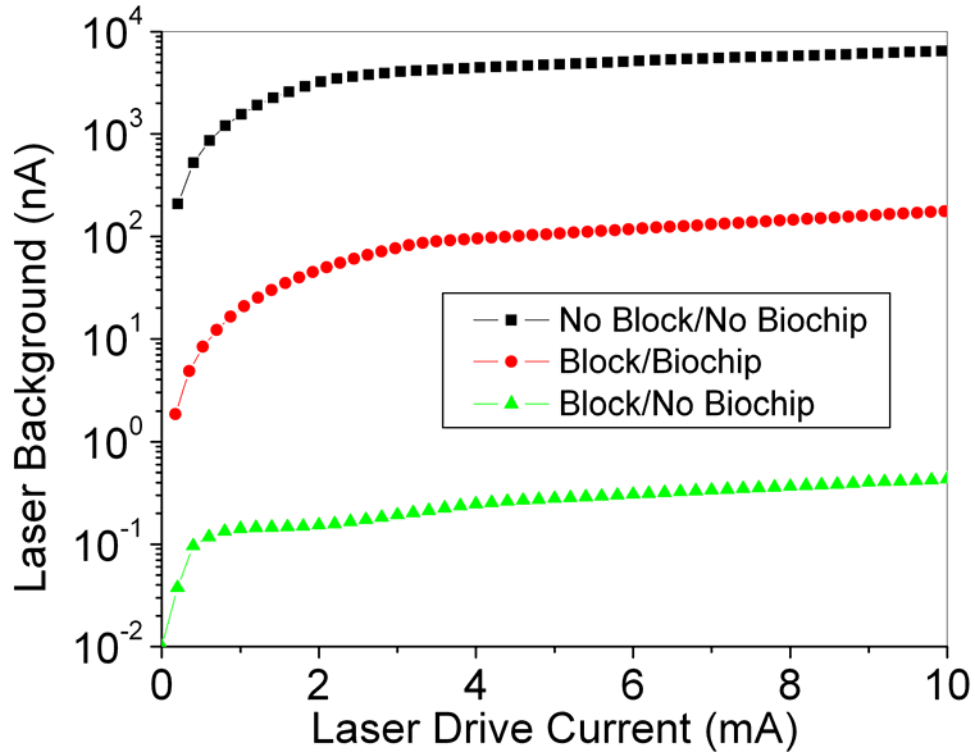


Fig. 7.8. Measured laser background as a function of laser drive current. A thin glass coverslip is placed 1mm above the sensor to illustrate the dramatic increase in background due to optical reflections. Sensor architecture is proximity.

7.3.2 CHARACTERIZATION

Further studies of laser background due to reflections above the sensor are conducted. In particular, background levels as a function of the separation between the sensor and glass components are examined. Also, the relative contributions to background from reflections due to spontaneous emission and the laser beam are examined.

Fig. 7.9 plots the laser background as a function of laser drive current for two separations (100 μ m and 500 μ m) between the sensor and glass slide. A kink in the curves can be seen due to the change in the laser's optical properties at threshold. Below threshold where spontaneous emission dominates, the background for the 100 μ m separation is much greater than the 500 μ m case. This is expected because spatial filtration of spontaneous emission increases as the distance between the sensor and glass slide increases. Above threshold, a much different phenomenon is observed. The laser

background for the 500 μm separation increases rapidly compared to the 100 μm case. For the 100 μm separation, the laser beam specular reflection falls within the inner diameter of the photodetector so this source of laser background is reduced. However, for the 500 μm separation case, the laser beam diverges (laser divergence equal to a full-width at half-maximum (FWHM) of 14 $^\circ$) so that the specular reflection illuminates the photodetector, resulting in a much greater contribution to laser background. In conclusion, background from spontaneous emission is greatly reduced for glass to sensor separations of greater than 100 μm . Also, for larger separations, the laser beam divergence reduces the amount of spatial filtration by failing to fall within the inner diameter of the photodetector.

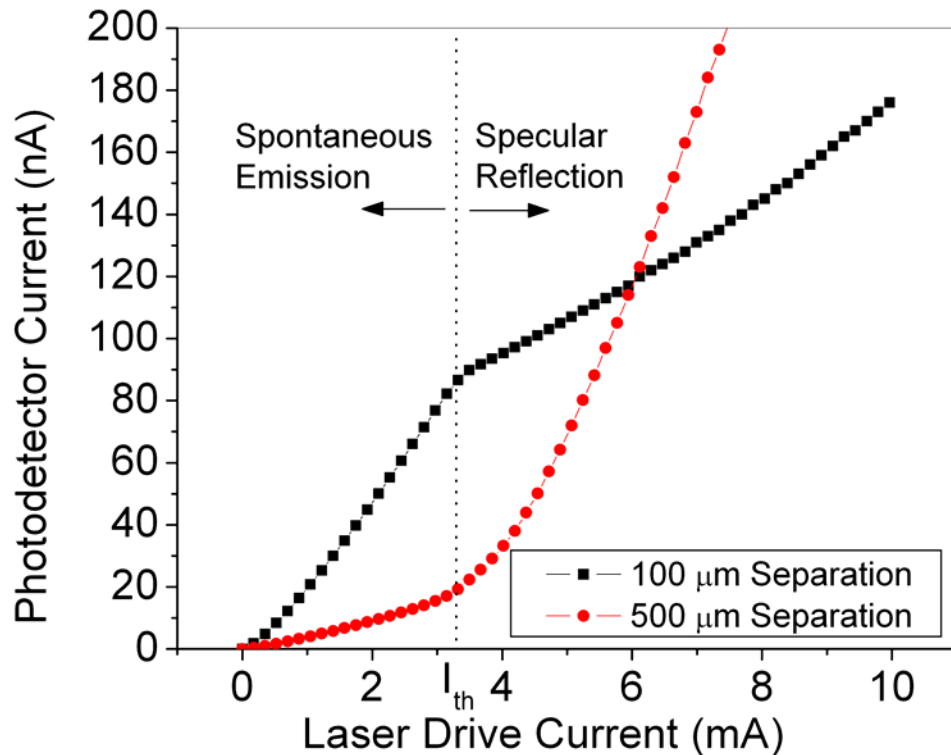


Fig 7.9. Measured laser background as a function of laser drive current with coverslip placed above. The experiment is conducted for two separations (100 μm and 500 μm) between the sensor and coverslip.

The laser background dependence on the separation distance between the sensor and coverslip is examined in more detail as shown in Fig. 7.10. The experiment is conducted with a coverslip without anti-reflection (AR) coating and a coverslip with AR coating on both sides. To analyze the indirect spontaneous emission, the background is measured at

the laser threshold of 3.6mA. To calculate the contribution from the laser beam reflection, the background is measured at a laser drive current of 10mA and the contribution due to indirect spontaneous emission is subtracted out.

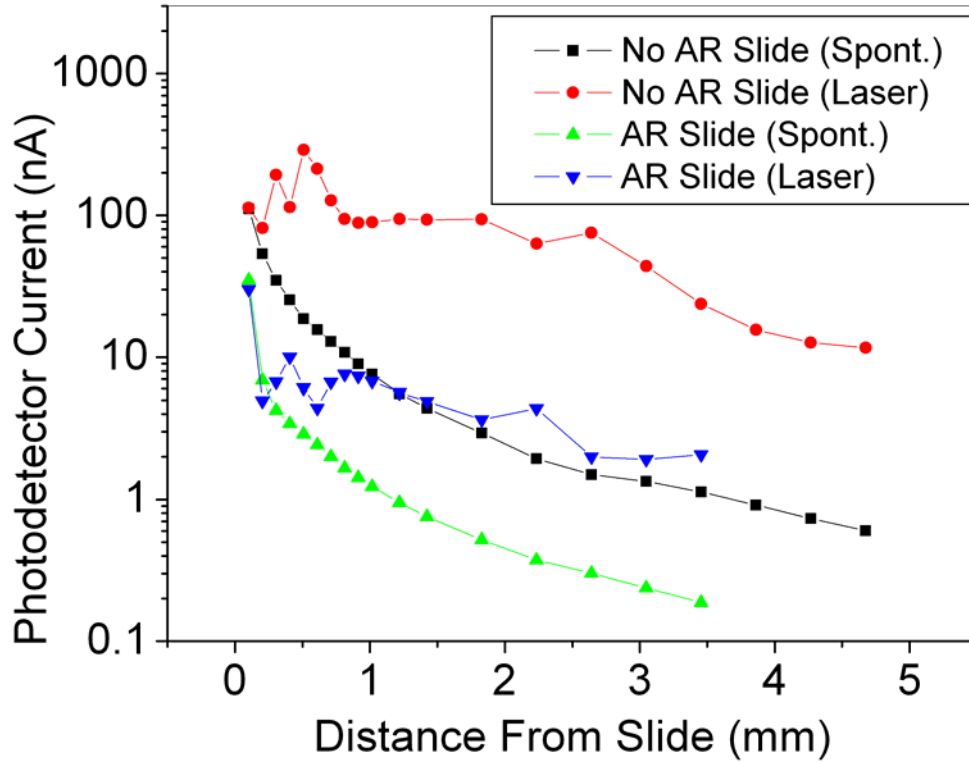


Fig. 7.10. Measured laser background contribution from spontaneous emission and laser beam reflection as a function of glass separation. Experiment is conducted with uncoated and AR coated slide.

Fig. 7.10 shows that large decreases in laser background are possible for large separations between the sensor and optical interfaces above the sensor. The background from spontaneous emission falls off dramatically as the separation between the sensor and glass slide increases. Also, the AR coating reduces the background from both the laser and spontaneous emission. For AR coatings and sensor spacing greater than 3mm, the background contributions from the laser beam and indirect incidence of spontaneous emission are reduced below 2nA, which shows that spatial filtration can be highly effective in reducing laser background.

For larger separations, Fig. 7.10 shows that the laser background from the laser beam is much greater than background from spontaneous emission. Monochromatic laser

radiation should be much easier to optically filter than broadband spontaneous emission as discussed above in Section 7.2.1. This result suggests that improvements in the optical filter performance will be highly effective in reducing laser background.

ASAP is used to simulate the total laser background as function of separation distance between the sensor and coverslip, see Fig. 7.11. The angular divergence data shown in Fig. 6.14 is used to model the VCSEL emission. Also, all radiation emitted from the VCSEL is modeled as monochromatic because ASAP cannot currently simulate broadband sources. The simulation agrees well with measurements for separations greater than 1mm, where specular reflection of the laser beam dominates. The simulation does not agree well for smaller separations because the contribution due to spontaneous emission is more significant. In other words, the monochromatic approximation does not adequately model the spectrally broad spontaneous emission. However, this example illustrates again that ASAP can be a powerful tool for simulating laser background in optoelectronic sensors.

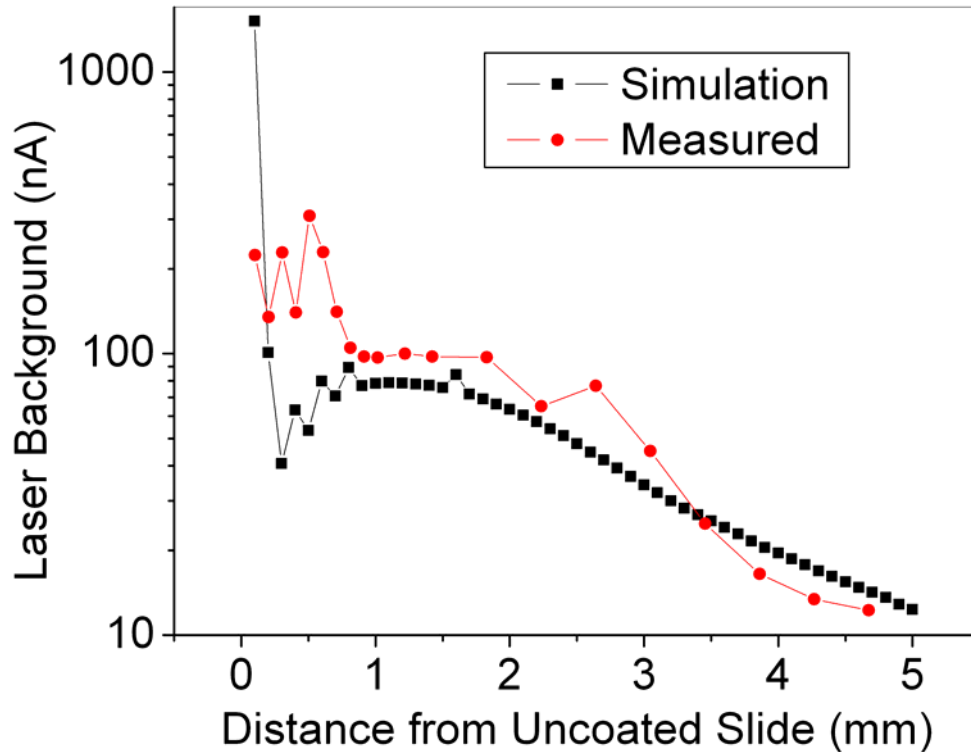


Fig. 7.11. Measured and simulated values of total laser background versus separation distance from uncoated coverslip. Simulation is generated with ASAP (Breault Research Organization).

For the laser beam contribution shown in Fig. 7.11, the oscillations in laser background are attributed to the toroidal far-field divergence of the VCSEL. For close sensor spacing (400 μm –900 μm), an increase in laser background is seen when the VCSEL beam diverges enough to hit the inner diameter of the photodetector (detector inner diameter is 200 μm and laser divergence is 14° FWHM). The two increases in the range of 400 μm –900 μm result from the two optical interfaces of the 150 μm thick slide. Then, the increase in background at about 2.5 -3.0mm is attributed to the laser hitting the outer diameter of the detector (Detector outer diameter is 1mm), where the emission filter is less effective in filtering the excitation light.

7.4 CONCLUSIONS

Several interesting and unique sources of laser background exist in these integrated sensors. Due to the close integration of the optoelectronic components, overwhelming background levels are measured from the direct incidence of spontaneous emission. Metal optical blocks drastically reduce this background from direct spontaneous emission and enables internal optical isolation of greater than 10^6 between the photodetector and filter. This important result shows that these optoelectronic components can be closely integrated together while maintaining high optical isolation between the devices. With the metal blocking walls in place, external sources of laser background from optical reflections above the sensor dominate the laser background characteristics. These sensors are particularly sensitive to reflections above the sensor due to the poorly performing optical filters. It is found that reflection of the laser beam dominates over spontaneous emission for larger separations between the sensor and optical interfaces above. This suggests that improvements in the filter performance should be highly successful in reducing background because the laser beam can be easily filtered. In conclusion, the sources of laser background are well understood. Through systematic engineering, these sources of laser background can be reduced and large increases in sensor sensitivity can be achieved.

CHAPTER 8

SENSITIVITY

Until now, most aspects of the sensor operation have been discussed, characterized and studied. However, the most important merit of any sensor is the actual sensor sensitivity in practical formats. This chapter details the characterization of the sensor sensitivity in several formats that are typically found in miniaturized and total analysis systems (μ TAS). The first brief experiment examines the sensor sensitivity in a microarray detection format. The second more detailed characterization involves implementing the sensor onto a microfluidic platform. Experimental results are compared to theory and other integrated sensing solutions found in the literature. Finally, sensitivity limitations are discussed and future sensitivity values are projected.

8.1 SENSITIVITY IN MICROARRAY FORMAT

8.1.1 EXPERIMENTAL SETUP

Microarrays have received much attention from the research community due to their potential for massively parallel analysis and continue to play an important role in μ TAS [33,116,117]. Microarray detection involves the surface immobilization of probe and target molecules to perform physical separation and analysis as described in Section 1.1. Therefore, microarray detection involves detecting fluorescent molecules on planar substrates. Fig. 8.1 illustrates the experimental architecture designed to simulate microarray detection and test sensor sensitivity. To estimate the sensitivity in a microarray format, IR-800 dye (LI-COR, Inc.) is spun onto a thin glass coverslip in a thin poly(methyl methacrylate) (PMMA) film. The spin solutions are 0.5% PMMA and various molar concentrations (12.5, 6.25, 3.2, 1.56 and 0.78mM) of IR-800 dye in acetonitril buffer. For a spinning speed of 3krpm, the PMMA film thickness is measured

to be about 100nm using a DekTak surface profilometer. The sensor is placed 500 μm from the coverslip for detection. At this distance, the spot size at the biochip is approximately 120 μm in diameter due to the vertical-cavity surface emitting laser (VCSEL) 14° full-width at half-maximum (FWHM) divergence, which is compatible with the feature size of low density microarrays [117]. A sensor with a 20 μm VCSEL aperture is used due to the higher output powers and correspondingly higher fluorescence signal levels. The inner and outer diameters of the photodetector are 200 and 1000 μm respectively.

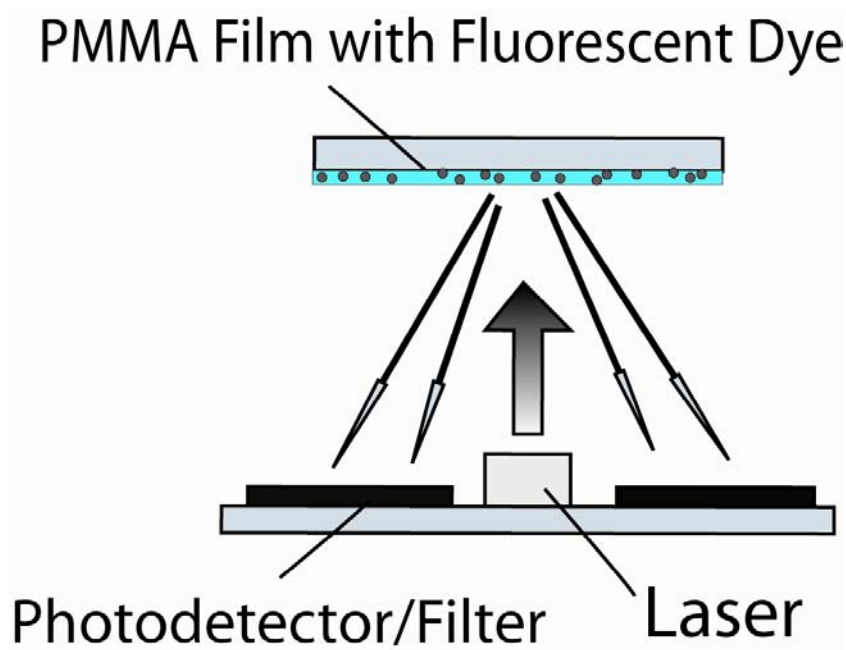


Fig. 8.1. Schematic of experimental setup used to simulate microarray detection format. IR-800 Dye is spun onto a glass substrate in a PMMA film. The sensor is placed 500 μm from the glass slide. Detector inner and outer diameters are 200 μm and 1mm, respectively.

8.1.2 MEASUREMENT OF SENSITIVITY

Slides of varying surface concentrations of IR-800 in PMMA are made to test the sensor sensitivity. The surface concentrations are estimated by measuring the absorbance through the thin PMMA films with an absorption spectrophotometer (Perkin Elmer, Lambda 19) and assuming a molar absorptivity of approximately 260,000 $\text{cm}^{-1}\text{M}^{-1}$ at $\lambda = 773\text{nm}$, which is the manufacturer's reported value in methanol buffer. Calibrated

sample dilutions are used to estimate surface concentrations below the spectrophotometer's detection limit.

The sensor response is measured as function of IR-800 surface concentration as shown in Fig. 8.2. The sensor response is linear with concentration with absorption saturation effects observed at the highest concentration of 10^7 molecules/ μm^2 . The lowest concentration measured is 6.0×10^5 molecules/ μm^2 . The sensor sensitivity is limited by a laser background level of 100nA. Laser background is dominated by optical reflections occurring above the sensor. Variations in optical alignment from switching samples of different surface concentrations causes large and random changes in the laser background, which limits the sensitivity. In experimental configurations allowing for stable optical and mechanical alignment, such as flow channel schemes, better sensitivity should be expected because the stable background level can be subtracted out. Assuming a 1nA response can be detected in the laser background level of 100nA, the sensor should be able to detect 10^5 molecules/ μm^2 .

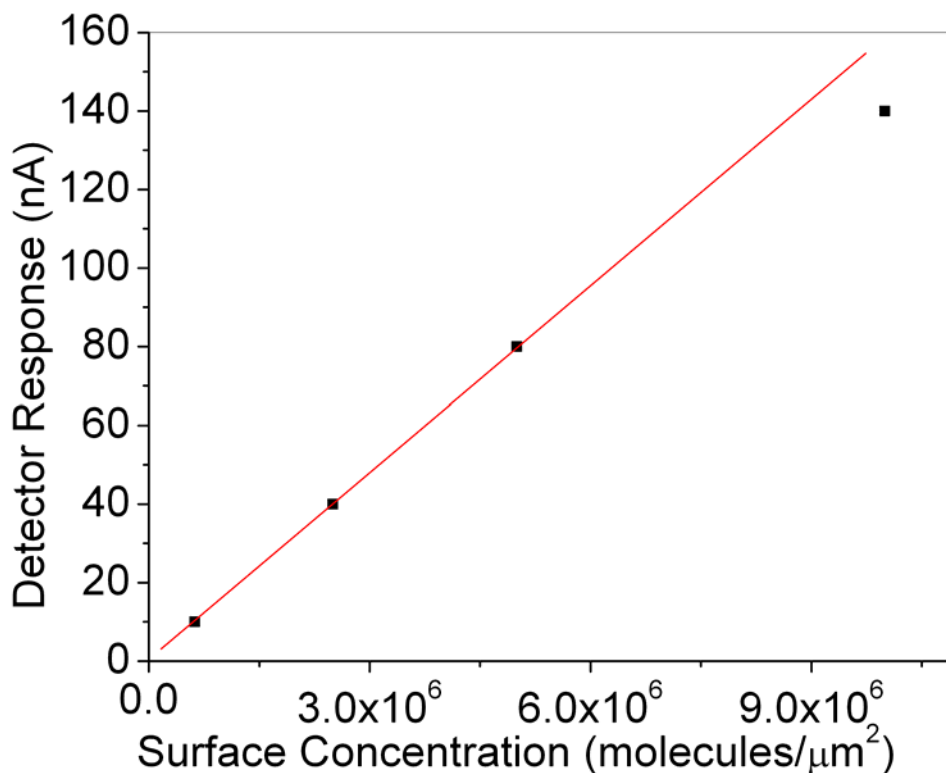


Fig. 8.2. Detection of IR-800 (LI-COR, Inc.) in microarray format. Measurement is conducted with $20\mu\text{m}$ aperture VCSEL at an output power of 2mW.

8.1.3 DISCUSSION

Current state-of-the art bulk optical approaches offer much better performance. Fluorescence detection limits in the range of 1 molecule/ μm^2 are feasible with waveguide and whispering gallery mode sensors [118,119]. Also, conventional scanning confocal architectures used to readout high density microarrays typically have 1 molecule/ μm^2 sensitivity [56,118]. The ability to have discrete bulk optical components allows for better rejection of laser background due to highly optimized spectral filters and the ability to spatially separate the optical components. Also, discrete component systems allow the use of sensitive photodetectors with internal gain, such as a photomultiplier tube (PMT) or avalanche photodiode (APD). Label-free approaches, such as electronic field effect or plasmon resonance imaging, are substantially less sensitive than fluorescence techniques and show sensitivities in the range of 10^3 – 10^4 molecules/ μm^2 [120,121]. Unfortunately, these techniques require the use of a capture element bound to a surface for high sensitivity and specificity and are not compatible with microfluidic separations such as capillary electrophoresis (CE).

Large increases in sensitivity are possible and discussed in more detail below in Section 8.3. Briefly, this approach suffers from poor spatial filtration due to the large area photodetector and poor spectral filtration. As shown below in the microfluidic implementation, the use of a lens allows for greater spacing between the sensor and biological sample, resulting in increased spatial filtration and lower background. In addition, it is believed that large improvements in the optical filter are possible as discussed in Section 6.2.2. It is believed that current sensitivity in this detection format can be improved by at least two orders of magnitude by improving the filter performance and clever optical system design.

8.2 SENSITIVITY IN MICROFLUIDIC FORMAT

8.2.1 SENSOR ARCHITECTURE AND EXPERIMENTAL SETUP

Microfluidic channels and integrated detection are important for μ TAS and emerging applications as discussed in Chapter 1. Therefore, the sensor is integrated onto a microfluidic channel to demonstrate sensitivity in a microfluidic format [122,123]. Fig. 8.3 shows the sensing architecture used for microfluidic detection, including relevant system dimensions. The proximity sensor architecture, with a VCSEL surrounded by a toroidal photodetector/filter module, is implemented in the design. A lens is used to both focus the laser beam into the microfluidic channel and collimate the emitted fluorescence from the channel into the photodetector/filter module.

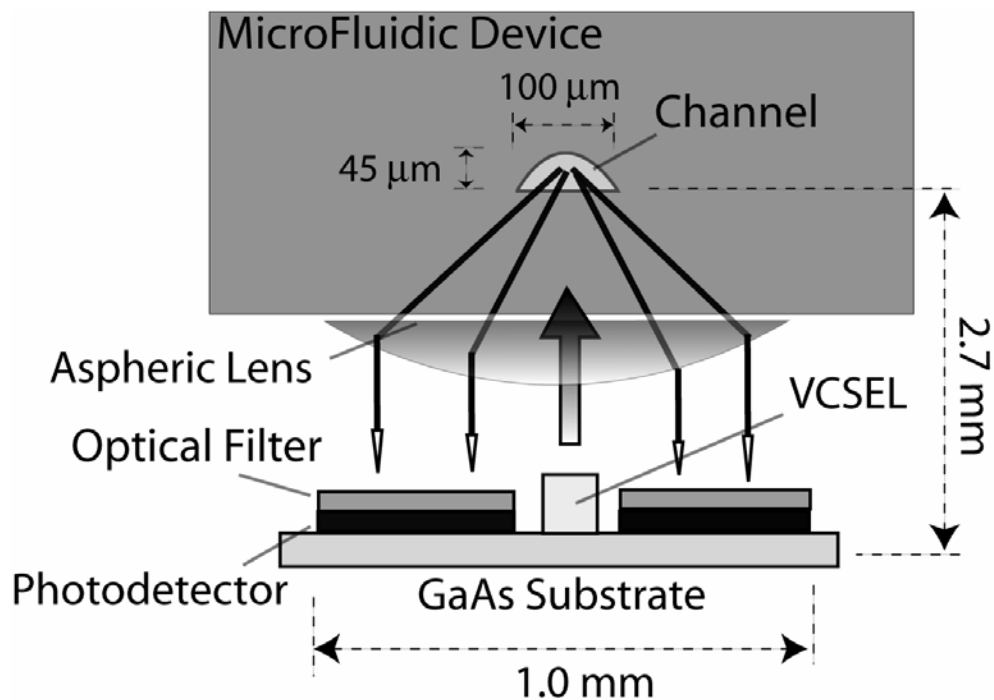


Fig. 8.3. Schematic of sensor architecture for microfluidic detection. A lens is used to both focus the laser beam into the channel and collect emitted fluorescence. Relevant system dimensions are shown in the figure. Inner and outer detector diameters are 200 μm and 1 mm, respectively.

An experimental setup is made to align the components (microfluidic channel, lens and optoelectronic devices) of the microfluidic sensor, see Fig. 8.4. A black anodized aluminum chuck forms the central building block of the setup. The microfluidic chip is

mounted on top of the chuck via vacuum. On top of the chuck, micrometers align the microfluidic channel relative to the lens. The lens is glued into a black anodized aluminum mount which can be screwed into a hole in the center of the chuck. The height of the lens with respect to the chuck is controlled by rotating the threaded lens mount. The optoelectronic elements are diced with a wafer saw and packaged into a 32-dip package with wire bonding and subsequently inserted into a printed circuit board (PCB). The PCB is mounted on a xyz stage underneath the chuck so that the optoelectronic elements can be aligned to the lens. Optical images of the packaged optoelectronic sensor and microfluidic setup can be viewed in Fig. 8.5.

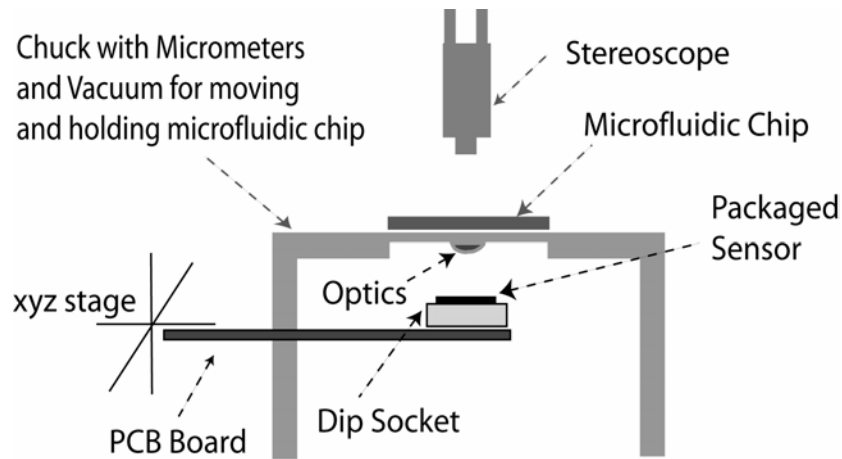


Fig. 8.4. Schematic of experimental setup used to align components of microfluidic sensor.

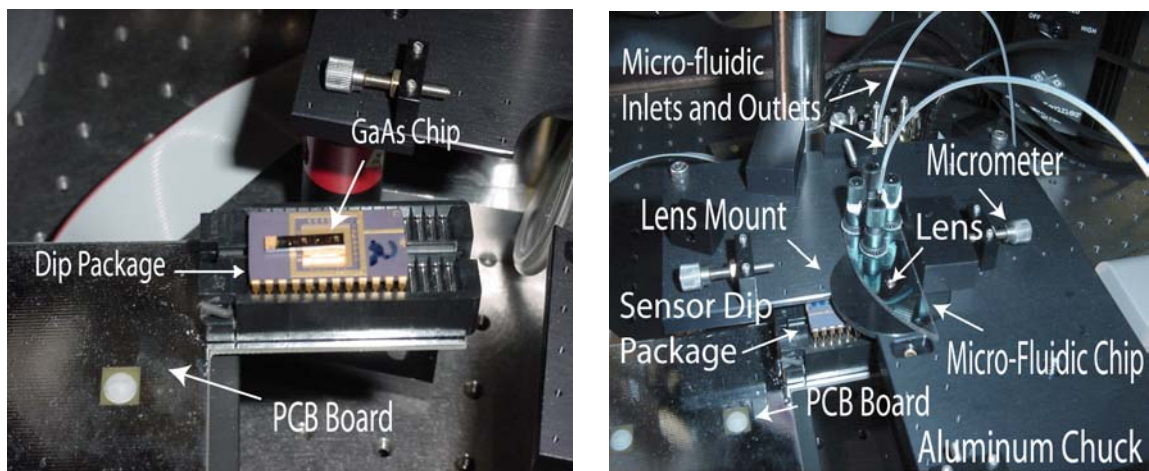


Fig. 8.5. Optical images of microfluidic experimental setup illustrated in Fig. 8.4. (Left) Image of GaAs optoelectronic chip packaged in a 32-dip package and inserted into a PCB. (Right) Close-up image of microfluidic setup during sensing experiment.

A non-sequential ray tracing program called ASAP (Breault Research Organization; Tuscon, AZ) is used during the design of the microfluidic sensor. Fig. 8.6 shows the ASAP geometric model of the microfluidic sensor and laser beam propagation within the microfluidic chip. Due to the far-field toroidal profile of the laser beam, the excitation spot is a ring and has a diameter of about $90\mu\text{m}$ within the flow channel, see Fig. 8.6. Smaller laser divergence angles and excitation spot sizes are possible through redesigning the laser to obtain more ideal beam divergence and mode behavior [124]. For example, Kamei *et. al.* report a spot diameter of $30\mu\text{m}$ in a similar optical architecture using an external laser source [60].

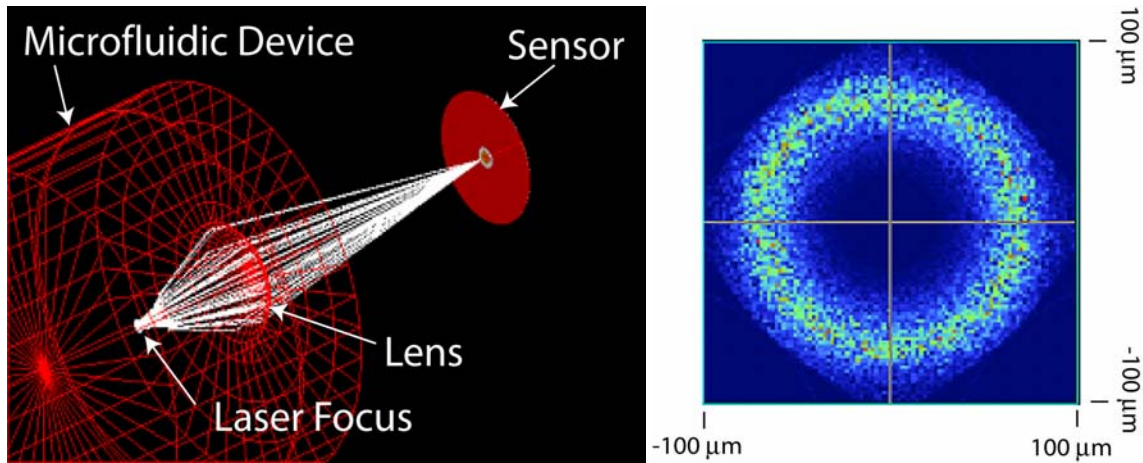


Fig. 8.6. Optical simulation of laser beam propagation in microfluidic channel. (Left) Geometric sensor model and simulation of laser beam propagation. (Right) Laser spot at the microfluidic channel.

The microfluidic chip and lens are anti-reflection (AR) coated on both sides to reduce laser background. The microfluidic chip has a specialized AR coating at 773nm , and the lens has a broadband coating. The lens is separated from the microfluidic chip by a space of approximately $20\mu\text{m}$. The optoelectronic sensor is placed 1.7mm away from the lens. ASAP is used to determine the focal plane of the aspheric lens (Geltech 370060, N.A. = 0.6 , $f = 0.682\text{mm}$) within the microfluidic chip. Then, the microfluidic channel is placed at the focal plane (See Fig. 8.3). With this design, the fluorescence collection efficiency of the lens (C_{lens}) is simulated with ASAP to be about 2.5% , see Table 8.1 below.

The microfluidic channel is made by standard wet-etching and bonding of two glass substrates (Schott D263), detailed elsewhere by Throckmorton *et. al.* [125]. The glass

substrate closest to the lens is thinned from an original thickness of 1.1mm to 300 μ m so that the channel is at the focal point of the lens as designed above. The channel depth, d , and width are 45 μ m and 100 μ m respectively. Inlet and outlet connectors (Upchurch Scientific) are mounted to the microfluidic chip. Standard tubing and syringes are used to interface with the microfluidic connectors. A syringe pump (Kd Scientific, Model #100) adds reagents to the channel at a continuous flow rate of 100 μ L/hr. The channels are cleaned with 200mM Sodium Hydroxide (NaOH) and rinsed with deionized water before use.

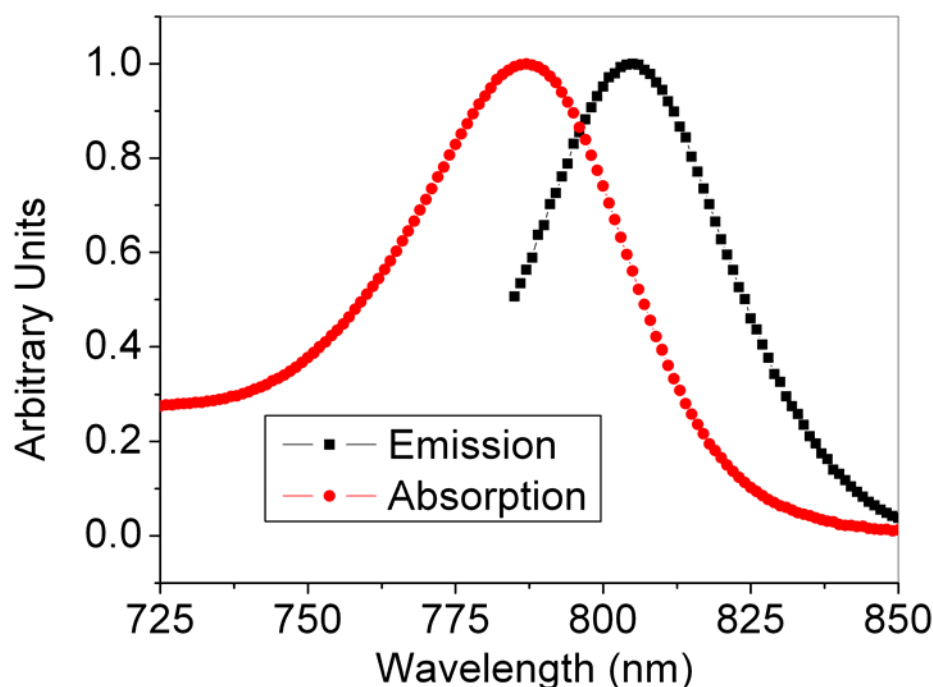


Fig. 8.7. Measured absorption and emission spectra of IR-800 dye in methanol buffer.

IR-800 dye (LICOR, Inc.) is dissolved in methanol, and dilutions are made to generate samples of various concentrations. The absorption and fluorescence characteristics of the dye solutions are measured with a UV/VIS/NIR spectrometer (Perkin Elmer-Lambda 19) and fluorimeter (Instruments S.A.- FluoroMax-2), see Fig. 8.7. The molar absorption coefficient (ϵ) of IR-800 dye in methanol is measured to be 161,000 $\text{cm}^{-1}\text{M}^{-1}$ at 773 nm, see Table 8.1 below. For simplicity, the quantum efficiency (QE_{Dye}) of IR-800 dye in methanol is assumed to be 15%, which is the value reported by

the manufacturer; see Table 8.1 below. As discussed in Section 6.2.2, the transmission of the fluorescence signal through the filter, T_{Filter} , is calculated to be about 40%, see Table 8.1 below.

8.2.2 SENSITIVITY MEASUREMENT

A semiconductor parameter analyzer (HP 4156A) is used to drive the VCSEL and readout the photodetector signal. The intracavity contact of the VCSEL and the backside substrate contact are grounded. The laser is driven through the top mesa contact at 10mA (1.9mW) with a drive voltage of $\sim 3V$. The photodetector readout voltage is set at 0V, and the detector current is measured through the top mesa contact of the photodetector. For the fluorescence measurement, data is collected for 20s with an integration time of 16.7ms and sampling rate of 10Hz.

Dilute concentrations of the fluorescent dye (IR-800 in methanol) are flowed (100 μ L/hr) through the channel with methanol flushes between dilutions to remove any dye adhesion to the sidewalls. Background signals are closely monitored to make sure that the channel had been thoroughly flushed between dilutions, and no problems are observed. For each concentration, the signal is measured to determine the sensor sensitivity as shown in Fig. 8.8. The sensor has a linear response of 1.62nA/ μ M. The laser background signal with running methanol buffer is approximately 63.5nA with a root-mean-square (rms) fluctuation of approximately 20pA. The DC value (63.5nA) is subtracted out from the background, yielding the remaining rms noise of 20pA. Assuming a S/N = 3, the theoretical limit of detection is extrapolated to be 40nM in a peak identification measurement such as capillary electrophoresis (CE). However, the average DC fluctuation of the background from run to run is approximately ± 150 pA. This fluctuation over the timescale of a few minutes limits the detection sensitivity to 250nM in continuous flow. Finally, the sensor response is measured at a range of flow rates (10, 100 and 600 μ L/hr) in order to test sensitivity for typical flow rates used during microfluidic separations. [5]. No change in sensor response is observed for these flow rates.

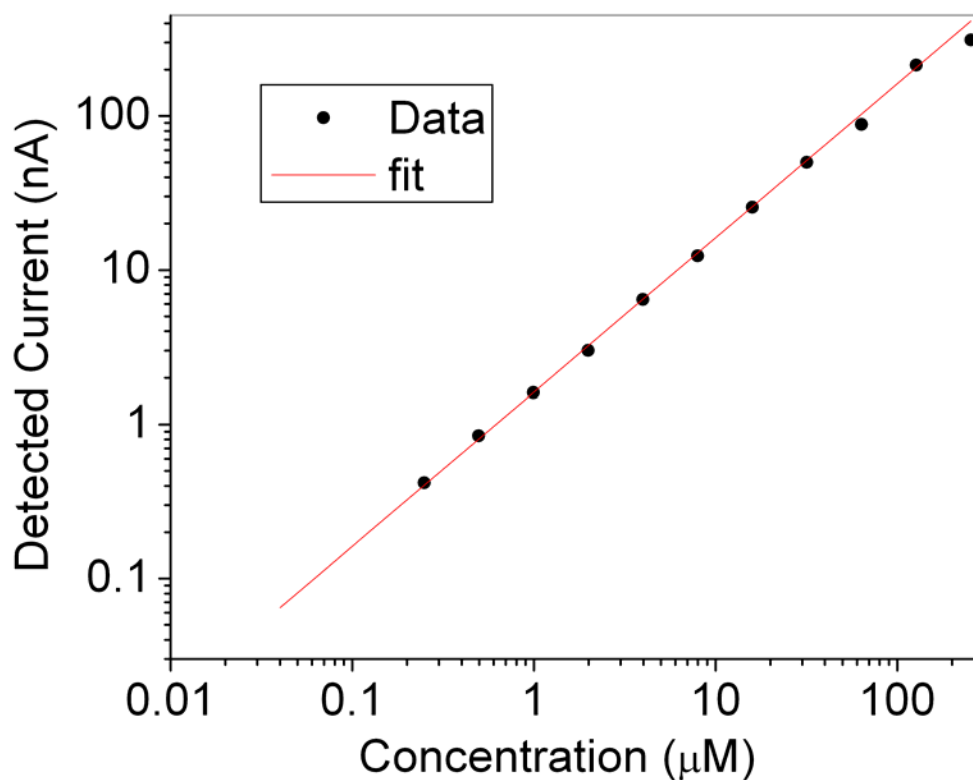


Fig. 8.8. Sensor sensitivity measurement in microfluidic format. Sensor response due to IR-800 (LI-COR, Inc.) in methanol under continuous flow ($100\mu\text{L/hr.}$). Laser output power is 1.9mW at a wavelength of 773nm .

Once again, laser background limits the sensor sensitivity. This experiment is conducted with a sensor without the improved metal blocking structures described in Section 7.2.2. Therefore, the background from direct incidence of spontaneous emission is comparable to the laser background due to reflections. With no optical interface above the sensor, the laser background is measured to be 29nA for a laser drive current, I_{drive} , of 10mA . With only the lens in place above the sensor, the background increases to 56nA , which results from optical scattering and reflections off the lens and black anodized lens mount. Due to the non-optimal broadband coating of the lens, there is significant reflection occurring from the lens when compared to the microfluidic substrate. Finally, the addition of the microfluidic channel with running buffer results in a total laser background of 63.5nA as reported above.

8.2.3 COMPARISON TO THEORY AND SIMULATION

Simple theoretical calculations agree reasonably well with the sensor response reported above. Table 8.1 lists parameters needed to theoretically calculate the sensor response. The following simple equation, derived in Section 2.2, is used to calculate the theoretical sensor response for detector current, I_{Det} ,

$$I_{Det} = \frac{\lambda_{em} q}{hc} P_{Las} QE_{Dye} QE_{Det} C_{lens} T_{Filter} (1 - 10^{-\varepsilon d M}), \quad (8.1)$$

where q is Coulomb's constant, h is Plank's constant, c is the speed of light, λ_{em} is the wavelength of the fluorescence emission, ε is the molar absorption coefficient, d is the channel depth, and M is the dye concentration. For simplicity, a constant λ_{em} of 805nm is assumed, which is the wavelength at the fluorescence maximum. The other relevant parameters are listed in Table 8.1 and are calculated or determined in the preceding characterization detailed in this thesis (See Sections 6.1, 6.2 and 8.1). By plugging in the parameters found in Table 8.1, $d = 45\mu\text{m}$, $P_{las} = 1.9\text{mW}$, and $M = 1\mu\text{M}$, the detector response is calculated to be 3.0nA from Eqn. 8.1. Experimentally, the detector response is found to be 1.6nA for a 1 μM concentration. The discrepancy between this simplified theory and measurement is due to the varying channel width. Eqn. 8.1 assumes a constant channel depth, whereas the channel depth changes across the channel profile, as shown in Fig. 8.3. In addition, due to the ring shaped laser spot, a significant amount of laser power illuminates the edge of the microfluidic channel, where the channel depth varies sharply. More sophisticated modeling is needed to determine the sensor performance as discussed below.

Absorptivity (ε) at $\lambda = 773 \text{ nm}$	QE of Dye	QE of Detector	Filter Trans.	Lens Collect.
161,000 $\text{cm}^{-1} \text{M}^{-1}$	15 %	100 %	40 %	2.5 %

Table 8.1. Important sensing parameters used to calculate the theoretical sensor response. These parameters are determined in the characterization presented in this thesis (See Sections 6.1, 6.2 and 8.1).

An optical ray tracing program called ASAP is used to simulate the sensor response. A geometric model of the sensor is programmed into ASAP and used to model the laser beam propagation, excitation of fluorescent molecules and resulting fluorescence signal propagation, shown in Fig. 8.9. As shown in Fig. 8.9, the simulation shows good agreement with experimental results and illustrates that optical simulations can be highly successful in modeling sensor behavior.

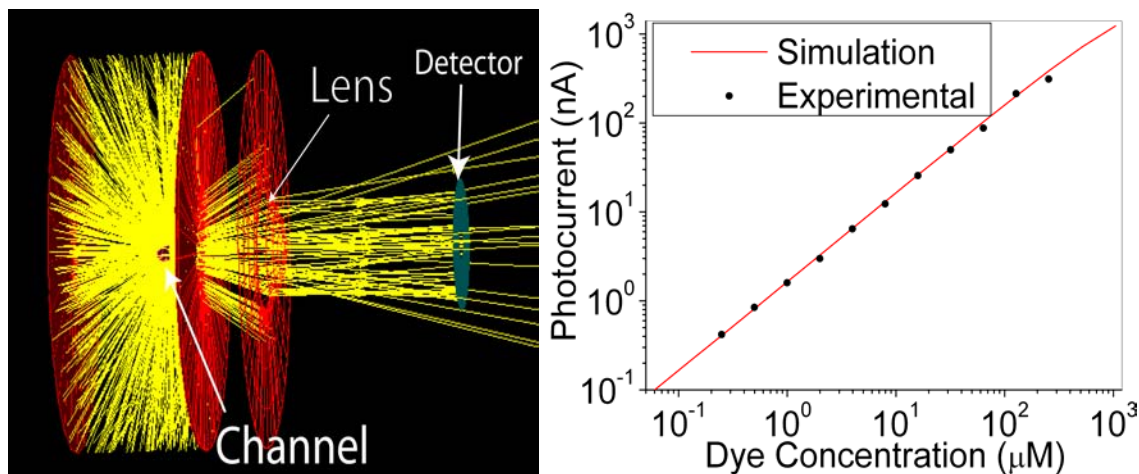


Fig. 8.9. Simulation of fluorescence sensing with ASAP. (Left) Geometric ASAP model of sensor with fluorescence signal propagation. (Right) Simulated sensor response together with measurement.

8.2.4 DISCUSSION

The detection limits reported above are comparable to or within an order magnitude of other integrated fluorescence sensors coupled to microfluidic channels seen in the literature [28,58,60,63,65] (See Fig. 8.10). In approaches with a similar optical architecture to the one presented in this thesis, detection limits of 17nM and 120nM have been reported [60,65]. The advantage of our approach is a completely monolithically integrated sensor solution for drastically reduced size and cost and increased parallelism.

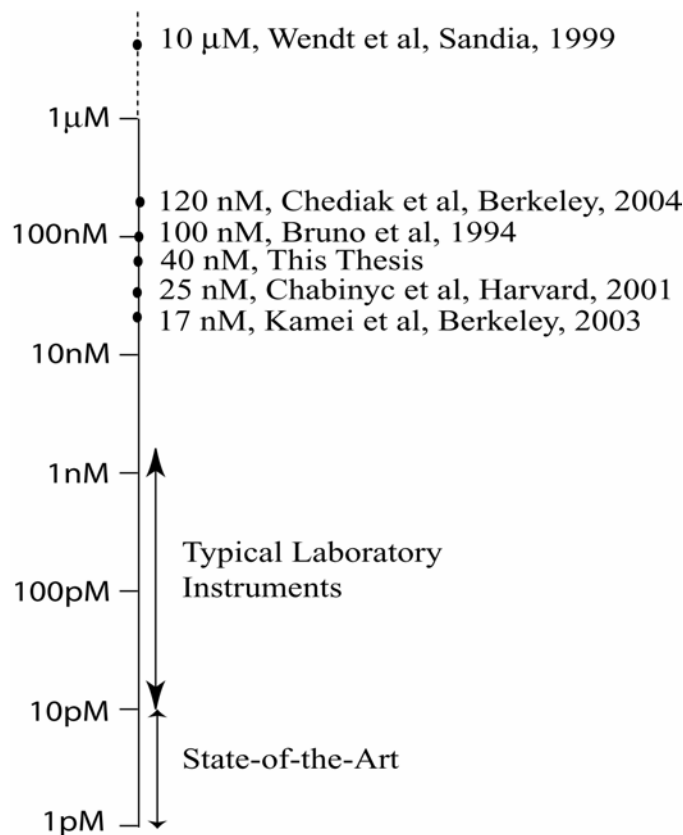


Fig. 8.10. Sensitivity comparison to well known approaches towards integrated fluorescence sensors for microfluidic applications found in the literature [28,58,60,63,65].

Unfortunately, as one moves to applications that employ aqueous buffers, the QE of IR-800 dye in solution decreases, thereby reducing the sensitivity of this approach for certain biologically relevant applications. In simple experiments with a fluorimeter (Instruments S.A.- FluoroMax-2), it is found that the QE of IR-800 covalently attached to the end of a single-stranded DNA oligonucleotide in aqueous buffer (10mM phosphate buffered saline, pH 8.0) drops by a factor of about 2.5 when compared to the dye in methanol.

The detection limits reported here will be sufficient for certain medical diagnostic applications, such as immunoassays and clinical chemistry [7]. However, for many applications, this level of sensitivity will not be sufficient. Preamplification methods, such as polymerase chain reaction (PCR) and surface immobilization, will be needed for successful detection in certain applications. For example, on-chip PCR combined with integrated detection would be useful in overcoming sensitivity limitations [6]. As a

comparison to typical detection limits seen in the laboratory, fluorescence detection limits using bulk-optic approaches are typically between 0.1–1.0 nM. Again, the ability to have discrete bulk optical components allows for good rejection of laser background due to the use of highly optimized spectral filters and the ability to spatially separate the optical components. As discussed below, large increases in sensitivity of the sensor presented in this thesis will be possible in the future and enable more widespread application.

8.3 IMPROVING SENSOR SENSITIVITY

As discussed above, the sensitivity of the sensor is much lower than typical and highly optimized laboratory equipment, as shown in Fig. 8.10. Fortunately, large increases in sensor sensitivity are possible through reducing laser background and increasing fluorescence collection efficiency. With the improvements suggested below, it is believed that at least a two order of magnitude improvement in sensor sensitivity is possible, enabling this technology to reach sensitivities comparable to discrete component systems.

Specular reflection of the laser beam dominates the laser background level as discussed in Section 7.3. Laser beam reflections can be easily filtered with interference filters because laser beam emission is monochromatic and occurs over a relatively narrow angular distribution. Clearly, the current filtration of OD 3 must be improved to reduce the background from these reflections. It is believed that much larger filtration is possible with the unconventional $\text{Al}_x\text{Ga}_{1-x}\text{As}$ semiconductor filter technology used in the present design. Already, filters with OD 4 performance have been demonstrated as described in Section 6.2.2. However, if the current filter technology proves inadequate, then conventional dielectric filter technology may be deposited directly onto the current design to increase filtration [48,59]. Through modifications to the filter, it is believed that a two order of magnitude increase in sensor sensitivity is possible.

Another significant increase in sensitivity can occur through maximizing the fluorescence collection efficiency. The emission filter limits the transmission of the fluorescent signal to ~40% due to the reflectivity sidelobes above 795nm as discussed in

Section 6.2.2. These reflectivity sidelobes can be eliminated by changing the DBR design slightly [48], allowing for an increase in fluorescence collection efficiency. In addition, utilizing sensing architectures that collect a greater portion of the fluorescence signal would increase the sensitivity. For example, in the microfluidic sensor, larger collection efficiency would be possible by utilizing a lens with a higher NA. Through these modifications, it is believed that the efficiency of the current sensor can be improved by a factor of 2-4.

As discussed in Section 7.3.2, spatial filtration may result in significant reductions of laser background. As shown in Fig. 7.10, the laser background can be significantly reduced by increasing the separation between the optoelectronic sensor and optical interfaces above. In the microfluidic experiment, the spacing between the sensor and lens is limited by the laser beam divergence and the lens aperture. For the 14° FWHM beam divergence and $840\mu\text{m}$ aperture lens diameter used in the experiment above, a maximum spacing of approximately 3.5mm can be reached without clipping a significant portion of the laser beam with the lens aperture. Fortunately, much lower divergences are possible with VCSELs and would allow greater spacing between the sensor and lens above [124]. A greater spacing between the sensor and lens would result in large reductions of laser background due to increased spatial filtration.

8.4 CONCLUSIONS

Sensor sensitivity is examined in a microarray and microfluidic format. The sensor sensitivity is useful for a variety of applications in medical diagnostics and is also comparable to well known integrated sensing approaches found in the literature. The current sensitivity is limited by laser background due to back reflection of the laser beam in combination with poorly performing optical filters. Large increases in sensitivity will be possible by increasing the spectral and spatial filtration to reduce laser background and by increasing fluorescence collection efficiency. Through systematic design improvements, it is believed detection limits of less than 1nM can be reached with this technology.

CHAPTER 9

SUMMARY AND FUTURE WORK

9.1 SUMMARY

This thesis demonstrates pioneering research in the area of integrated optical sensors for biological applications. The design of the sensor capitalizes on optoelectronic technologies for telecommunications and monolithically integrates a vertical-cavity surface-emitting laser (VCSEL), PIN photodetector and emission filter to create a miniature and fully integrated fluorescence sensor. By utilizing semiconductor batch fabrication processes and packaging, this sensor promises drastically reduced size and cost and increased parallelism, which could enable a range of interesting new applications in biological sensing.

This work marks the first effort to integrate the laser and photodetector together in such close proximity to achieve fluorescence sensing. Due to the close integration, laser background sources are created and limit the sensitivity of the sensor. Metal optical blocking structures are integrated to reduce laser background levels, and greater than 10^6 optical isolation between the photodetector and VCSEL is achieved. This important result shows that optoelectronic devices can be monolithically integrated and maintain sufficient optical isolation for fluorescence sensing. Due to poor optical filter performance, reflections from optical interfaces above the sensor currently limit the sensor sensitivity.

In order to test sensitivity, the sensor is integrated onto a microfluidic channel. In continuous flow, an experimental and theoretical limit of detection is determined to be 250nM and 40nM, respectively, of IR-800 dye in methanol. These detection limits are comparable to other integrated solutions detailed in the literature and illustrate that the sensor could be useful in certain applications, such immunology. In the future, order of magnitude improvements in sensitivity are expected by improving the filter performance

and other system modifications. It is believed that this technology can achieve detection limits of less than 1nM and be useful for a variety of practical applications.

9.2 FUTURE WORK

9.2.1 LASER BACKGROUND REDUCTION

Unfortunately, the current filter $\text{Al}_x\text{Ga}_{1-x}\text{As}$ design does not perform at the designed optical density (OD) 5, but yields only OD 3 rejection. This small rejection causes large laser background levels, which limits sensor sensitivity, due to optical reflections and scattered laser light. Fortunately, it is found that better performance of OD 4 is possible with $\text{Al}_x\text{Ga}_{1-x}\text{As}$ filters by raising the material bandgap to reduce parasitic sub-bandgap absorption and filter fluorescence. It is believed that larger filter rejection is possible by continuing to raise the material bandgap. At the $\text{Al}_x\text{Ga}_{1-x}\text{As}$ direct-to-indirect band crossover point ($x \approx 0.4$), drastically reduced filter fluorescence may be possible due to less efficient radiative recombination, which may drastically improve filter performance [39,40]. Integration of conventional dielectric filter technology is another viable option to improve filter performance. Dielectric filters could be deposited onto the current $\text{Al}_x\text{Ga}_{1-x}\text{As}$ filters to provide additional filtration at the cost of more complex fabrication procedures.

In addition to the design improvements suggested above, a great deal more freedom exists in the design of the filter. Exploring this space should result in much better filtering solutions. For example, implementing $\text{Al}_x\text{Ga}_{1-x}\text{As}$ absorption based filters in combination with interference filters is promising. Eliminating the reflectivity sidelobes in the current distributed Bragg reflector (DBR) design should increase the current fluorescence transmission efficiency of 40% to near 100% transmission, marking a factor of 2.5 improvement.

Optical isolation elements enable an internal optical isolation of greater than 10^6 between the photodetector and integrated laser. It is believed that even greater isolation may be possible than that reported in this thesis. Careful study of the residual internal

background may illuminate some design solutions to further reduce background and improve sensitivity. Defects in the metal blocking layers, such as pin-holes, may be the cause of the remaining detector background. Instead of optical interaction, electrical coupling may be responsible for the increase of detector background during laser operation. Electrically isolating the devices would be successful in eliminating electrical coupling.

The photoresist reflow step during the fabrication of metal blocking elements limits how close the VCSEL and photodetector can be integrated. In the proximity design, a closer integration would increase fluorescence collection efficiency and design flexibility. There are many possible solutions that would enable optical isolation elements while maintaining close integration. Coating the sensor with pigmented or absorbing polymers is an interesting alternative method to using metal layers.

Spontaneous emission can be difficult to filter and create large background in fluorescence sensing systems. Most off-the-shelf laser sources have an aperture to eliminate unwanted spontaneous emission. Creating VCSELs with micro-apertures would be an interesting analog to discrete sources. Fabrication processes similar to those used for the metal optical blocks could be used to create micro-apertures. The micro-aperture could significantly reduce background from reflected spontaneous emission.

9.2.2 OPTICAL SYSTEM DESIGN

An enormous design space waits to be explored in designing the optical system surrounding the integrated optoelectronic sensor. Optical designs that offer a large amount of spatial filtration would be particularly successful in increasing sensor sensitivity. The imaging architecture would be interesting to explore and offers the benefits of increased spatial filtration and high speed operation. In addition, it is desirable to design the system for maximum fluorescence collection efficiency. For example, by utilizing a larger numerical aperture lens in the microfluidic sensor, large gains in sensitivity may be possible.

9.2.3 APPLICATIONS

Implementing the sensor in more sophisticated biological applications is a logical extension of this work. Microfluidic implementations are particularly appealing with this technology. The sensor could be used for a variety of applications, such as capillary electrophoresis (CE) and chromatography. It would be interesting to explore portable diagnostic applications and investigate the advantages of near-infrared (NIR) detection during the analysis of complex field samples. Exploring sensitivity and experimental repeatability gains by having a robust sensor bonded with a microfluidic channel is appealing. Demonstrating highly parallel sensing architectures for increased throughput would be impressive. As applications are explored, the sensor may need to be redesigned to be compatible with different fluorescent markers. For example, moving towards shorter wavelengths would be appealing due to the presence of high quality dyes available from 600-700nm. Exploring the design tradeoffs would be interesting as the sensor is redesigned for different spectral ranges.

APPENDIX A

EPITAXIAL STRUCTURES

Chapter 5 gives a general overview of the epitaxial fabrication and semiconductor processing procedures needed to realize the integrated sensors. This Appendix exactly details the growth recipe and epitaxial structures for the devices discussed in this thesis.

A.1 LOW-NOISE PHOTODETECTOR (WAFER P222)

%Integrated Filter

20nm GaAs; $N_{\text{silicon}} = 1\text{E}19 \text{ cm}^{-3}$
274.7nm $\text{Al}_{0.3}\text{Ga}_{0.7}\text{As}$; $N_{\text{silicon}} = 1\text{E}18 \text{ cm}^{-3}$

%Repeat 20 times the next 2 lines
63.2nm $\text{Al}_{0.98}\text{Ga}_{0.02}\text{As}$; $N_{\text{silicon}} = 1\text{E}18 \text{ cm}^{-3}$
54.9nm $\text{Al}_{0.3}\text{Ga}_{0.7}\text{As}$; $N_{\text{silicon}} = 1\text{E}18 \text{ cm}^{-3}$

%Repeat 19 times the next 2 lines
63.2nm $\text{Al}_{0.98}\text{Ga}_{0.02}\text{As}$; $N_{\text{silicon}} = 5\text{E}18 \text{ cm}^{-3}$
54.9nm $\text{Al}_{0.3}\text{Ga}_{0.7}\text{As}$; $N_{\text{silicon}} = 5\text{E}18 \text{ cm}^{-3}$

%Detector Active Region

109.9nm $\text{Al}_{0.3}\text{Ga}_{0.7}\text{As}$; $N_{\text{silicon}} = 1\text{E}18 \text{ cm}^{-3}$
50nm GaAs; $N_{\text{silicon}} = 1\text{E}18 \text{ cm}^{-3}$
1500nm GaAs; Undoped
350nm GaAs; $P_{\text{carbon}} = 5\text{E}18 \text{ cm}^{-3}$

%Substrate

P+ GaAs substrate

A.2 INTEGRATED SENSOR (WAFER P763-5)

%Top DBR

20nm GaAs; $P_{\text{carbon}} = 5\text{E}19 \text{ cm}^{-3}$
36.3nm $\text{Al}_{0.25}\text{Ga}_{0.75}\text{As}$; $P_{\text{carbon}} = 6\text{E}18 \text{ cm}^{-3}$
20nm Grading $\text{Al}_{0.95}\text{Ga}_{0.05}\text{As} > \text{Al}_{0.25}\text{Ga}_{0.75}\text{As}$; $P_{\text{carbon}} = 6\text{E}18 \text{ cm}^{-3}$

41.7nm Al_{0.95}Ga_{0.05}As ; P_{carbon} = 6E18 cm⁻³

%Repeat 15 times the next 4 lines

20nm Grading Al_{0.25}Ga_{0.75}As > Al_{0.95}Ga_{0.05}As; P_{carbon} = 6E18 cm⁻³

36.3nm Al_{0.25}Ga_{0.75}As; P_{carbon} = 6E18 cm⁻³

20nm Grading Al_{0.95}Ga_{0.05}As > Al_{0.25}Ga_{0.75}As; P_{carbon} = 6E18 cm⁻³

41.7nm Al_{0.95}Ga_{0.05}As; P_{carbon} = 6E18 cm⁻³

%Repeat 6 times the next 4 lines

20nm Grading Al_{0.25}Ga_{0.75}As > Al_{0.95}Ga_{0.05}As ; P_{carbon} = 2E18 cm⁻³

36.3nm Al_{0.25}Ga_{0.75}As; P_{carbon} = 2E18 cm⁻³

20nm Grading Al_{0.95}Ga_{0.05}As > Al_{0.25}Ga_{0.75}As; P_{carbon} = 2E18 cm⁻³

41.7nm Al_{0.95}Ga_{0.05}As ; P_{carbon} = 2E18 cm⁻³

%Repeat 4 times the next 4 lines

20nm Grading Al_{0.25}Ga_{0.75}As > Al_{0.95}Ga_{0.05}As ; P_{carbon} = 1E18 cm⁻³

36.3nm Al_{0.25}Ga_{0.75}As; P_{carbon} = 1E18 cm⁻³

20nm Grading Al_{0.95}Ga_{0.05}As > Al_{0.25}Ga_{0.75}As; P_{carbon} = 1E18 cm⁻³

41.7nm Al_{0.95}Ga_{0.05}As ; P_{carbon} = 1E18 cm⁻³

20nm Grading Al_{0.25}Ga_{0.75}As > Al_{0.95}Ga_{0.05}As ; P_{carbon} = 1E18 cm⁻³

36.3nm Al_{0.25}Ga_{0.75}As; P_{carbon} = 1E18 cm⁻³

%Oxide Aperture

20nm Grading Al_{0.98}Ga_{0.02}As > Al_{0.25}Ga_{0.75}As ; P_{carbon} = 1E17 cm⁻³

42nm Al_{0.98}Ga_{0.02}As; P_{carbon} = 1E17 cm⁻³

50nm Grading Al_{0.3}Ga_{0.7}As > Al_{0.98}Ga_{0.02}As ; P_{carbon} = 1E17 cm⁻³

%Cavity

43.5nm Al_{0.3}Ga_{0.7}As; Undoped

7nm Al_{0.11}Ga_{0.89}As; Undoped Quantum Well

8nm Al_{0.3}Ga_{0.7}As; Undoped

7nm Al_{0.11}Ga_{0.89}As; Undoped Quantum Well

8nm Al_{0.3}Ga_{0.7}As; Undoped

7nm Al_{0.11}Ga_{0.89}As; Undoped Quantum Well

8nm Al_{0.3}Ga_{0.7}As; Undoped

7nm Al_{0.11}Ga_{0.89}As; Undoped Quantum Well

29.5nm Al_{0.3}Ga_{0.7}As; Undoped

%Oxide Aperture

50nm Al_{0.3}Ga_{0.7}As; N_{silicon} = 5E17 cm⁻³

63.2nm Al_{0.98}Ga_{0.02}As; N_{silicon} = 1E18 cm⁻³

%Bottom DBR and Intracavity Contact

10nm GaAs; N_{silicon} = 5E19 cm⁻³

270.7nm Al_{0.25}Ga_{0.75}As; N_{silicon} = 1E18 cm⁻³

%Repeat 20 times the next 2 lines
63.1nm Al_{0.95}Ga_{0.05}As ; N_{silicon} = 1E18 cm⁻³
55nm Al_{0.25}Ga_{0.75}As; N_{silicon} = 1E18 cm⁻³

%Repeat 20 times the next 2 lines
63.1nm Al_{0.95}Ga_{0.05}As ; N_{silicon} = 5E18 cm⁻³
55nm Al_{0.25}Ga_{0.75}As; N_{silicon} = 5E18 cm⁻³

%Detector Active Region

109.9nm Al_{0.25}Ga_{0.75}As; N_{silicon} = 1E18 cm⁻³
50nm GaAs; N_{silicon} = 1E18 cm⁻³
2000nm GaAs; Undoped
50nm GaAs; P_{carbon} = 1E18 cm⁻³
200nm GaAs; P_{carbon} = 2E18 cm⁻³

%Substrate

P+ GaAs substrate

APPENDIX B

PROCESSING RECIPES

Chapter 5 gives a general overview of the epitaxial fabrication and semiconductor processing procedures needed to realize the integrated sensors. This Appendix specifically details the exact steps used for each processing procedure described in Chapter 5. The Appendix is organized by general processing procedure with the specific fabrication steps listed beneath each procedure.

B.1 ELECTRICAL CONTACTS

B.1.1 LITHOGRAPHY FOR 1.5 μ m FILM BILAYER LIFTOFF PROCESS

Oxide removal in beaker

-1:10 Ammonium Hydroxide:DI water for 1min

Singe wafer at 120C for at least 2min on hotplate

Spin HMDS at 5500rpm for 20s with Headway manual spinner

Spin LOL2000 (Shipley) for 3000A film with Headway manual spinner

-Pour at 500rpm and hold for 5s

-Ramp to 1500rpm and hold for 75s

Backside LOL2000 removal with swabs and EC13 (Shipley) solvent

Bake LOL2000 at 170C for 6min on hotplate

Spin 3612 (Shipley) for 1.5 μ m film with Headway manual spinner

-Cover wafer completely with resist while not spinning

-Ramp to 500rpm and hold for 5s

-Ramp to 3000rpm and hold for 40s

Backside 3612 removal with swabs and EC13 solvent

Bake 3612 at 90C for 60s on hotplate

Edge bead exposure (15mW/cm²) for 100s with Karl Suss MA-6 mask aligner

-Use wafer scraps as mask

Develop in LDDW26 (Shipley) for 1min to remove edge bead in beaker

Rinse with DI water

Mask exposure (15mW/cm²) for 2s with Karl Suss MA-6 mask aligner

Develop in LDDW26 for 40s in beaker

-Should see double line that is characteristic of bilayer undercut

Rinse with DI water

B.1.2 LITHOGRAPHY FOR 3 μ m FILM BILAYER LIFTOFF PROCESS

Oxide removal in beaker

-1:10 Ammonium Hydroxide:DI water for 1min

Singe wafer at 120C for at least 2min on hotplate

Spin HMDS at 5500rpm for 20s with Headway manual spinner

Spin LOL2000 (Shipley) for 3000A film with Headway manual spinner

-pour at 500rpm and hold for 5s

-ramp to 1500rpm and hold for 75s

Backside LOL2000 removal with swabs and EC13 (Shipley) solvent

Bake LOL2000 at 170C for 6min on hotplate

Spin SPR220-3 μ m (Shipley) for 3.0 μ m film with Headway manual spinner

-cover wafer completely with resist while not spinning

-ramp to 500rpm and hold for 5s

-ramp to 3000rpm and hold for 40s

Backside SPR220 removal with cotton swabs and EC13 solvent

Bake SPR220 at 90C for 10min on hotplate

Edge bead exposure (15mW/cm²) for 100s with Karl Suss MA-6 mask aligner

-use wafer scraps as mask

Develop in LDDW26 for 1min to remove edge bead in beaker

Rinse with DI water

Mask exposure (15mW/cm²) for 4s with Karl Suss MA-6 mask aligner

Develop in LDDW26 for 75s in beaker

-should see double line that is characteristic of bilayer undercut

Rinse with DI water

B.1.3 METAL DEPOSITION FOR P-CONTACT AND LIFTOFF

Polymer descum with Drytek RIE Etcher

-20sccm O₂, 100W, 170mT for 30s

Oxide removal in beaker

-1:10 Ammonium Hydroxide:DI water for 30s

Deposit metal with Innotec E-beam Evaporator

-P-contact: 250A Ti/400A Pt/2300A Au

-Place in evaporator immediately after oxide removal

Liftoff with 1165 (Shipley) solvent in beaker

-Remember that flash point of 1165 is 75C

-Use ultrasonic bath if necessary

B.1.4 METAL DEPOSITION FOR N-CONTACT AND LIFTOFF

Polymer descum with Drytek RIE Etcher

-20sccm O₂, 100W, 170mT for 30s

Oxide removal in beaker

-1:10 Ammonium Hydroxide:DI water for 30s

Deposit metal with Innotec E-beam Evaporator
-N-contact: 400A Au/120A Ge/125A Ni/2000A Au
-Place in evaporator immediately after oxide removal
Liftoff with 1165 (Shipley) solvent in beaker
-Remember that flash point of 1165 is 75C
-Use ultrasonic bath if necessary

B.1.5 THERMAL ANNEALING

Rapid thermal anneal (AG Associates, Mini-Pulse) for N-contact
-Ramp to 420°C in 1min from room temperature
-Hold at 420°C for 1min
-Return to room temperature

B.2 ETCHING

B.2.1 LITHOGRAPHY FOR 2 μ M RESIST ETCH MASK

Oxide Removal in beaker
-1:10 Ammonium Hydroxide:DI water for 1min
Singe wafer at 120C for at least 2min on hotplate
Spin HMDS at 5500rpm for 20s with Headway manual spinner
Spin AZ9220 (Clariant) for 2 μ m film with Headway manual spinner
-cover wafer completely with resist while not spinning
-ramp to 500rpm and hold for 5s
-ramp to 4.5krpm and hold for 40s
Backside AZ9220 removal with swabs and acetone
Bake AZ9220 at 110C for 90s on hotplate
Edge bead exposure (15mW/cm²) for 100s with Karl Suss MA-6 Mask Aligner
-use wafer scraps as mask
Develop in 421k Developer (Clariant) for 1min to remove edge bead in beaker
Rinse with DI water
Mask exposure (15mW/cm²) for 20s with Karl Suss MA-6 Mask Aligner
Develop in 421k Developer for about 25s in beaker
-watch for endpoint of development and add 5s
Rinse with DI water
Hard bake mask resist with hotplate for dry etching
-130C for 30min

B.2.2 LITHOGRAPHY FOR 7 μ M RESIST ETCH MASK

Oxide removal in beaker

-1:10 Ammonium Hydroxide:DI water for 1min

Singe wafer at 120C for at least 2min on hotplate

Spin HMDS at 5500rpm for 20s with Headway manual spinner

Spin AZ9260 (Clariant) for 7 μ m film with Headway manual spinner

-Cover wafer completely with resist while not spinning

-Ramp to 500rpm and hold for 5s

-Ramp to 4.5krpm and hold for 60s

Backside AZ9260 removal with swabs and acetone

Bake AZ9260 at 110C for 2min and 45s on hotplate

Edge bead exposure (15mW/cm²) for 100s with Karl Suss MA-6 mask aligner

-Use wafer scraps as mask

Develop in 421k Developer (Clariant) for 2min to remove edge bead in beaker

Rinse with DI water

Mask exposure (15mW/cm²) for 40s with Karl Suss MA-6 mask aligner

Develop in 421k Developer for about 1min in beaker

-Watch for endpoint of development and add 15s

Rinse with DI water

Hard bake mask resist with hotplate for dry etching

-130C for 30min

B.2.3 MESA DRY ETCHING

Mount sample onto Plasmaquest carrier wafer

-Cover backside of sample as evenly as possible with double-sided copper tape for good etch uniformity.

ECR-RIE Dry Etch with Plasmaquest

-15sccm Ar, 10sccm BCl₃ and 1.5sccm Cl₂

-400W microwave power, 55W RF plasma power and 2mT chamber pressure

-Sample temperature held at 13C

-Etch rate \approx .1 μ m/min

Strip resist if done with etch mask

-Use solvent such as acetone or 1165 remover

-May need polymer descum if baked on hard

B.2.4 WET ETCH SEQUENCE FOR INTRACAVITY CONTACT

Oxide removal in beaker

-1:10 Ammonium Hydroxide:DI water for 1min

-no rinse and place immediately into next etch

Selective etch onto Al_{0.98}Ga_{0.02}As with citric acid in beaker

-1:12 Hydrogen Peroxide (30%): citric acid

-wafer color is black when lands on Al_{0.98}Ga_{0.02}As \approx 2 min.

-no rinse and place immediately into next etch
Selective Etch onto GaAs with BOE in beaker
-1:15 BOE (6:1):DI water for 30s
Rinse immediately with DI water
%Surface treatment for contact layer
Oxide Removal in beaker
-1:10 Ammonium Hydroxide:DI water for 30s
Rinse with DI water
Hydrogen Peroxide (30%) etch for 20s in beaker
Rinse with DI water
Oxide Removal in beaker
-1:10 Ammonium Hydroxide:DI water for 30s
Rinse with DI water

B.3 OXIDATION

Oxide Removal in beaker
-1:10 Ammonium Hydroxide:DI water for 1min
Place in Oxidation Furnace
-95C bubbler temperature and 400C furnace temperature
-100sccm N₂ through bubbler
-Oxidize for about 14min for 20μm oxide penetration
-calibration runs highly recommended

B.4 VIA AND METAL BLOCK FORMATION

B.4.1 LITHOGRAPHY FOR RESIST MICROSTRUCTURES

Singe wafer at 120C for at least 2min on hotplate
Spin HMDS at 5500rpm for 20s with Headway manual spinner
Spin AZ9260 (Clariant) for 9μm film with Headway manual spinner
-cover wafer completely with resist while not spinning and wait 30s
-ramp to 500rpm and hold for 5s
-ramp to 3krpm and hold for 60s
Backside AZ9260 removal with swabs and acetone
Bake AZ9260 at 110C for 2min and 45s on hotplate
Edge bead exposure (15mW/cm²) for 100s with Karl Suss MA-6 mask aligner
-use wafer scraps as mask
Develop in 421k Developer (Clariant) for 2min to remove edge bead in beaker
Rinse with DI water
Mask Exposure (15mW/cm²) for 40s with Karl Suss MA-6 mask aligner
Develop in 421k Developer for about 1min in beaker

-watch for endpoint of development and add 15s
Rinse with DI water

B.4.2 OVEN CURE

Cure resist in BLUEM Oven
-Cure in N₂ Atmosphere
-1.5hr ramp to 140C and hold for 2hr
-4.5hr ramp to 325C and hold for 2hr
-1hr ramp to 25C

B.4.3 LITHOGRAPHY FOR 7 μ m FILM BILAYER LIFT-OFF PROCESS

Oxide Removal in beaker
-1:10 Ammonium Hydroxide:DI water for 1min
Singe wafer at 120C for at least 2min on hotplate
Spin HMDS at 5500rpm for 20s with Headway manual spinner
Spin LOL2000 (Shipley) for 3000A film with Headway manual spinner
-pour at 500 rpm and hold for 5s
-ramp to 1500 rpm and hold for 75s
Backside LOL2000 removal with swabs and EC13 (Shipley) solvent
Bake LOL2000 at 170C for 6 min on hotplate
Spin SPR220-7 μ m for 7.0 μ m film with Headway manual spinner
-cover wafer completely with resist while not spinning
-ramp to 500rpm and hold for 5s
-ramp to 5000rpm and hold for 40s
Backside SPR220 (Shipley) removal with swabs and EC13 solvent
Bake SPR220 at 90C for 10min on hotplate
Edge bead exposure (15mW/cm²) for 100s with Karl Suss MA-6 mask aligner
-use wafer scraps as mask
Develop in LDDW26 (Shipley) for 2min to remove edge bead in beaker
Rinse with DI water
Mask Exposure (15mW/cm²) for 12s with Karl Suss MA-6 mask aligner
-4 exposures for 3s with 30s interval
Develop in LDDW26 for 2min and 15s in beaker
-should see double line that is characteristic of bilayer undercut
Rinse with DI water

B.4.4 METALIZATION FOR VIA AND METAL BLOCK

Deposit metal with Innotec E-beam Evaporator
- 250A Ti/2000A Au
Liftoff with 1165 solvent in beaker
-Remember that flash point of 1165 is 75C and use ultrasonic if necessary

BIBLIOGRAPHY

- [1] A. Manz, N. Graber, and H. M. Widmer, "Miniaturized total chemical-analysis systems: a novel concept for chemical sensing," *Sens. Actuators B-Chem*, vol. 1, pp. 244-248, 1990.
- [2] A. J. Tudos, G. A. J. Besselink, and R. B. M. Shasfoort, "Trends in miniaturized total analysis systems for point-of-care testing in clinical chemistry," *Lab Chip*, vol. 1, no. 2, pp. 83-95, 2001.
- [3] G. H. W. Sanders, and A. Manz, "Chip-based microsystems for genomic and proteomic analysis," *TRAC-Trends Anal. Chem.*, vol. 19, no. 6, pp. 364-378, 2000.
- [4] E. Verpoorte, and N. F. de Rooij, "Microfluidics Meets MEMs," *Proc. IEEE*, vol. 91, no. 6, 2003.
- [5] L. Bousse, C. Cohen, T. Nikiforov, A. Chow, A. R. Kopf-Sill, R. Dubrow, and J. W. Parce, "Electrokinetically controlled microfluidic analysis systems," *Ann. Rev. Biophys. Biomolec. Struct.*, vol. 29, pp. 155-181, 2000.
- [6] B. M. Paegel, R. G. Blazej, and R. A. Mathies, "Microfluidic devices for DNA sequencing: sample preparation and electrophoretic analysis," *Curr. Opin. Biotech.*, vol. 14, no. 1, pp. 42-50, 2003.
- [7] K. E. Petersen, W. A. McMillan, G. T. A. Kovacs, M. A. Northrup, L. A. Christel, and F. Pourahmadi, "Toward next generation clinical diagnostic instruments: scaling and new processing paradigms," *J. Biomed. Microdev.*, vol. 1, no. 1, pp. 71-79, 1998.
- [8] P. A. Auroux, D. Iossifidis, D. R. Reyes, and A. Manz, "Micro total analysis systems. 2. analytical standard operations and applications," *Anal.Chem.*, vol. 74, no. 12, pp. 2637-2652, 2002.
- [9] E. M. Southern, "DNA chips: analyzing sequence by hybridization to oligonucleotides on a large scale," *Trends Genet.*, vol. 12, no. 3, pp. 110-115, 1996.
- [10] A. Brecht, and G. Gauglitz, "Recent developments in optical transducers for chemical or biochemical applications," *Sens. Actuator B-Chem.*, vol. 38-39, pp. 1-7, 1997.
- [11] R. L. Edelstein, C. R. Tamanaha, P. E. Sheehan, M. M. Miller, D. R. Baselt, L. J. Whitman, and R. J. Colton, "The BARC biosensor applied to the detection of biological warfare agents," *Biosens. Bioelectron.*, vol. 14, no. 10-11, pp. 805-813, 2000.

- [12] E. Verpoorte, "Chip vision-optics for microchips," *Lab Chip*, vol. 3, pp. 42N-52N, 2003.
- [13] T. Vo-Dinh, and B. Cullum, "Biosensors and biochips: advances in biological and medical diagnostics," *Fresenius J. Anal. Chem.*, vol. 366, pp. 540-551, 2000.
- [14] J. Lichtenberg, N. F. de Rooij, and E. Verpoorte, "Sample pretreatment on microfabricated devices," *Talanta*, vol. 56, no. 2, pp. 233-266, 2002.
- [15] A. J. de Mello, and N. Beard, "Dealing with 'real' samples: sample pre-treatment in microfluidic systems," *Lab Chip*, vol. 3, no. 1, pp. 11N-19N, 2003.
- [16] P. N. Prasad, *Biophotonics*. Hoboken, NJ: Wiley-Interscience, 2003.
- [17] J. C. Fister, S. C. Jacobson, L. M. Davis, and J. M. Ramsey, "Counting single chromophore molecules for ultrasensitive analysis and separations on microchip devices," *Anal. Chem.*, vol. 70, no. 3, pp. 431-437, 1998.
- [18] J. R. Lakowicz, *Principles of Fluorescence Spectroscopy*. 2nd Ed. New York: Kluwer Academic/Plenum, 1999.
- [19] M. A. Mycek, and B. W. Pogue, *Handbook of Biomedical Fluorescence*. New York: Marcel Dekker, 2003.
- [20] D. B. Murphy, *Fundamentals of Light Microscopy and Electronic Imaging*. New York: Wiley Liss, 2001.
- [21] H. P. Haugland, *Handbook of Fluorescent Probes and Research Chemicals*, 6th Ed. Eugene, OR: Molecular Probes, 1996.
- [22] F. H. Kasten, "Introduction to fluorescent probes: Properties, history and applications," in *Fluorescent and Luminescent Probes for Biological Activity*, W. T. Mason, ed., pp. 12-33. London: Academic Press, 1993.
- [23] S. A. Soper, J. H. Flanagan, Jr., B. L. Legendre, Jr., D. C. Williams, and R. P. Hammer, "Near-infrared, laser-induced fluorescence detection for DNA sequencing applications," *IEEE J. Sel. Top. Quantum. Electron.*, vol. 2, no. 4, pp. 1129-1139, 1996.
- [24] G. Ocvirk, T. Tang, and D. J. Harrison, "Optimization of confocal epifluorescence microscopy for microchip-based miniaturized total analysis systems," *Analyst*, vol. 123, pp. 1429-1434, 1998.
- [25] J. B. Pawley, *Handbook of Biological Confocal Microscopy*, 2nd Ed. New York: Plenum, 1995.
- [26] D. C. Harris, "Fundamentals of spectrophotometry," in *Quantitative Chemical Analysis*, 5th Ed, pp. 511-534. New York: W. H. Freeman and Company, 1999.

- [27] E. Hecht, *Optics*, 4th Ed. Reading, Mass.: Addison-Wesley, 1998.
- [28] A. E. Bruno, F. Maystre, B. Krattiger, P. Nussbaum, and E. Gassmann, "The pigtailed approach to optical detection in capillary electrophoresis," *Trac- Trends Anal. Chem.*, vol. 13, no. 5, pp. 190-197, 1994.
- [29] J. C. Roulet, E. Verpoorte, R. Volkel, H. P. Herzig, N. F. de Rooij, and R. Dandiker, "Microlens systems for fluorescence detection in chemical microsystems," *Opt. Eng.*, vol. 40, no. 5, pp. 814-821, 2001.
- [30] J. Sowell, L. Strekowski, and G. Patonay, "DNA and protein applications of near-infrared dyes," *J. Biomed. Opt.*, vol. 7, no. 4, pp. 571-575, 2002.
- [31] R. S. Duthie, I. M. Kalve, S. B. Samols, S. Hamilton, I. Livshin, M. Khot, S. Nampalli, S. Kumar, and C. W. Fuller, "Novel Cyanine dye-labeled dideoxynucleoside triphosphates for DNA sequencing," *Bioconjugate Chem.*, vol. 13, no. 4, pp. 699-706, 2002.
- [32] R. Weissleder, C. H. Tung, U. Mahmood, and A. Bogdanov, Jr., "In vivo imaging of tumors with protease-activated near-infrared fluorescent probes," *Nature Biotechnology*, vol. 17, pp. 375-378, 1999.
- [33] K. F. Buechler, P. McPherson, J. Anderberg, K. Nakamura, S. Lesefko, and B. Noar, "Microarray immunoassays in the microfluidic triage protein chip," *Proceedings of the uTAS*, Monterey, CA, pp. 42-44, 2001.
- [34] K. J. Halbhauer, and K. Konig, "Modern laser scanning microscopy in biology, biotechnology and medicine," *Annals of Anatomy*, vol. 185, pp. 1-20, 2003.
- [35] X. Li, B. Chance, A. G. Yodh, "Fluorescent heterogeneities in turbid media: limits for detection, characterization, and comparison with absorption," *Applied Optics*, vol. 37, pp. 6833-6844, 1998.
- [36] D. C. Williams, and S. A. Soper, "Ultrasensitive near-IR fluorescence detection for capillary gel electrophoresis and DNA sequencing applications," *Anal. Chem.*, vol. 67, pp. 3427-3432, 1995.
- [37] R. E. Bailey, and S. Nie, "Alloyed semiconductor quantum dots: tuning the optical properties without changing the particle size," *J. Am. Chem. Soc.*, vol. 125, pp. 7100-7106, 2003.
- [38] J. E. Berlier, A. Rothe, G. Buller, J. Bradford, D. R. Gray, B. J. Filanoski, W. G. Telford, S. Yue, J. Liu, C. Y. Cheung, W. Chang, J. D. Hirsch, J. M. Beechem, R. P. Haugland, and R. P. Haugland, "Quantitative comparison of long-wavelength Alexa fluor dyes to Cy dyes: Fluorescence of the dyes and their bioconjugates," *J. Histochem. Cytochem.*, vol. 51, pp. 1699-1712, 2003.
- [39] S. L. Chuang, *Physics of Optoelectronic Devices*. New York: Wiley, 1995.

- [40] A. Baldereschi, E. Hess, K. Maschke, H. Neumann, K. R. Schulze, and K. Unger, "Energy band structure of $\text{Al}_x\text{Ga}_{1-x}\text{As}$," *Journal of Physics C*, vol. 10, pp. 4709-4717, 1977.
- [41] P. Bhattacharya, *Semiconductor Optoelectronic Devices*, 2nd Ed. Upper Saddle River, NJ.: Prentice Hall, 1997.
- [42] E. D. Palik, *Handbook of Optical Constants of Solids*, Vol. 1. Orlando: Academic Press, 1985.
- [43] H. C. Casey, and M. B. Panish, *Heterostructure Lasers: Part B, Materials and Operating Characteristics*. New York: Academic Press, 1978.
- [44] S. R. Johnson, and T. Tiedje, "Temperature dependence of the Urbach edge in GaAs," *J. Appl. Phys.*, vol. 78, pp. 5609-5613, 1995.
- [45] A. E. Siegman, *Lasers*. Mill Valley, CA: University Science Books, 1986.
- [46] L. A. Coldren, and S. W. Corzine, *Diode Lasers and Photonic Integrated Circuits*. New York: Wiley, 1995.
- [47] C. W. Wilmsen, H. Temkin, and L. A. Coldren, *Vertical-Cavity Surface-Emitting Lasers: Design, Fabrication, and Applications*. New York: Cambridge University Press, 1999.
- [48] H. A. Macleod, *Thin-Film Optical Filters*, 3rd Ed. Philadelphia: Institute of Physics Pub, 2001.
- [49] A. Yariv, *Quantum Electronics*, 3rd Ed. New York: Wiley, 1989.
- [50] H. Soda, K. Iga, C. Kitahara, and Y. Suematsu, "GaInAsP/InP surface emitting injection lasers," *Japan J. Appl. Phys.*, vol. 18, pp. 2329-2330, 1979.
- [51] W. W. Chow, K. D. Choquette, J. H. Crawford, K. L. Lear, and G. R. Hadley, "Design, fabrication, and performance of infrared and visible vertical-cavity surface-emitting lasers," *IEEE J. Quantum Electronics*, vol. 33, pp. 1810-1824, 1997.
- [52] J. D. Lambkin, "Red VCSEL technology," *Compound Semiconductor*, vol. 6, pp. 65-70, 2000.
- [53] S. P. Denbaars, "Gallium-nitride-based materials for blue to ultraviolet optoelectronics devices," *Proc. IEEE*, vol. 85, no. 11, pp. 1740-1749, 1997.
- [54] K. D. Choquette, J. F. Klem, A. J. Fischer, O. Blum, A. A. Allerman, I. J. Fritz, S. R. Kurtz, W. G. Breiland, R. Sieg, K. M. Geib, J. W. Scott, and R. L. Naone, "Room temperature continuous wave InGaAsN quantum well vertical-cavity lasers emitting at 1.3 μm ," *Electronics Letters*, vol. 36, no. 16, pp. 1388-1390, 2000.

- [55] M. A. Wistey, S. R. Bank, H. B. Yuen, L. Goddard, and J. S. Harris, Jr., "Monolithic, GaInNAsSb VCSELs at 1.46 μm on GaAs by MBE," *Electronics Letters*, vol. 39, no. 25, pp. 1822-1823, 2003.
- [56] G. L. Duveneck, A. P. Abel, M. A. Bopp, G. M. Kresbach, and M. Ehrat, "Planar waveguides for ultra-high sensitivity of the analysis of nucleic acids," *Anal. Chim. Acta*, vol. 469, no. 1, pp. 49-61, Sept. 2002.
- [57] P. N. Zeller, G. Voirin, and R. E. Kunz,, "Single-pad scheme for integrated optical fluorescence sensing," *Biosensors and Bioelectronics*, vol. 15, pp. 591-595, 2000.
- [58] M. L. Chabinye, D. T. Chiu, J. Cooper McDonald, A. D. Stooch, J. F. Christian, A. M. Karger, and G. M. Whitesides, "An integrated fluorescence detection system in poly(dimethylsiloxane) for microfluidic applications," *Anal. Chem.*, vol. 73, no. 18, pp. 4491-4498, Feb. 2001.
- [59] J. R. Webster, M. A. Burns, D. T. Burke, and C. H. Mastrangelo, "Monolithic capillary electrophoresis device with integrated fluorescence detector," *Anal. Chem.*, vol. 73, no. 7, pp. 1622-1626, Apr. 2001.
- [60] T. Kamei, B. M. Paegel, J. R. Scherer, A. M. Skelley, R. A. Street, and R. A. Mathies, "Integrated hydrogenated amorphous Si photodiode detector for microfluidic bioanalytical devices," *Anal. Chem.*, vol. 75, pp. 5300-5305, 2003.
- [61] J. C. Roulet, R. Volkel, H. P. Herzig, E. Verpoorte, N. F. de Rooij, and R. Dandliker, "Performance of an integrated microoptical system for fluorescence detection in microfluidic systems," *Anal. Chem.*, vol. 74, pp. 3400-3407, 2002.
- [62] G. M. Yee, N. I. Maluf, P. A. Hing, M. Albin, and G. T. A. Kovacs, "Miniature spectrometers for biochemical analysis," *Sensors and Actuators A*, vol. 58, pp. 61-66, 1997.
- [63] J. R. Wendt, M. E. Warren, W. C. Sweatt, C. G. Bailey, C. M. Matzke, D. W. Arnold, A. A. Allerman, T. R. Carter, R. E. Asbill, and S. Samora, "Fabrication of high performance microlenses for an integrated capillary channel electrochromatograph with fluorescence detection," *J. Vac. Sci. Technol. B*, vol. 17, no. 6, pp. 3252-3255, Nov. 1999.
- [64] A. E. Bruno, S. Barnard, M. Rouilly, A. Waldner, J. Berger, and M. Ehrat, "All-solid state miniaturized fluorescence sensor array for the determination of critical gases and electrolytes in blood," *Anal. Chem.*, vol. 69, no. 3, pp. 507-513, Feb. 1997.
- [65] J. A. Chediak, Z. Luo, J. Seo, N. Cheung, L. P. Lee, and T. D. Sands, "Heterogeneous integration of CdS filters with GaN LEDs for fluorescence detection microsystems," *Sensors and Actuators A*, vol. 111, pp. 1-7, 2004.

- [66] H. Kosaka, "Smart integration and packaging of 2-D VCSEL's for high-speed parallel links," *IEEE J. Sel. Top. Quantum. Electron.*, vol. 5, pp. 184-192, 1999.
- [67] A. V. Krishnamoorthy, and K. W. Goosen, "Optoelectronic-VLSI: photonics integrated with VLSI circuits," *IEEE J. Sel. Top. Quantum. Electron.*, vol. 4, no. 6, pp. 899-912, 1998.
- [68] P. Yuan, S. Wang, X. Sun, X. G. Zheng, A. L. Holmes, and J. C. Campbell, "Avalanche photodiodes with an impact-ionization-engineered multiplication region," *IEEE Photonics Technol. Lett.*, vol. 12, no. 10, pp. 1370-1372, 2000.
- [69] O. Sjolund, D. A. Louderback, E. R. Hegblom, J. Ko, and L. A. Coldren, "Monolithic integration of substrate input/output resonant photodetectors and vertical-cavity lasers," *IEEE J. Quantum Electron.*, vol. 35, no. 7, pp. 1015-1023, 1999.
- [70] C. G. Fonstad, "Very large scale monolithic heterogeneous optoelectronic integration: the epitaxy-on-electronics, silicon-on-gallium arsenide, and aligned pillar bonding techniques" in *Heterogeneous Integration*, edited by Elias Towe, SPIE, 2000.
- [71] W. Lenth, A. Chu, L. J. Mahoney, R. W. McClelland, R. W. Mountain, and D. J. Silversmith, "Planar GaAs p-i-n photodiode with picosecond time response," *Appl. Phys. Lett.*, vol. 46, no. 2, pp. 191-193, 1985.
- [72] D. Tauber, G. Wang, R. S. Geels, J. E. Bowers, and L. A. Coldren, "Large and small signal dynamics of vertical cavity surface emitting lasers," *Appl. Phys. Lett.*, vol. 62, pp. 325-327, 1993.
- [73] M. Eisner, and J. Schwider, "Transferring resist microlenses into silicon by reactive ion etching," *Opt. Eng.*, vol. 35, pp. 2979-2982, 1996.
- [74] K. H. Jeong, and L. P. Lee, "A new method of increasing numerical aperture of microlens for biophotonic MEMs," *Proceedings of IEEE Conference on Microtechnologies in Medicine & Biology*, Madison, WI, pp. 380-383, 2002.
- [75] S. Sinzinger and J. Jahns, *Microoptics*, 2nd Ed. Cambridge: Wiley-VCH, 2003.
- [76] P. Nussbaum, R. Volkel, H. P. Herzig, M. Eisner, and S. Haselbeck, "Design, fabrication and testing of microlens arrays for sensors and microsystems," *Pure and Applied Optics*, vol. 6, pp. 617-636, 1997.
- [77] J. C. Roulet, R. Volkel, H. P. Herzig, E. Verpoorte, N. F. de Rooij, and R. Dandliker, "Microlens systems for fluorescence detection in chemical microsystems," *Opt. Eng.*, vol. 40, no. 5, pp. 814-821, May 2001.

- [78] E. Thrush, O. Levi, W. Ha, G. Carey, L. J. Cook, J. Deich, S. J. Smith, W. E. Moerner, and J. S. Harris, Jr., "Integrated semiconductor vertical-cavity surface-emitting lasers and PIN photodetectors for bio-medical fluorescence sensing," *J. Quantum Electron.*, vol. 40, pp. 491-499, 2004.
- [79] M. H. MacDougal, P. D. Dapkus, A. E. Bond, C. K. Lin, and J. Geske, "Design and fabrication of VCSEL's with Al_xO_y -GaAs DBR's," *IEEE J. Sel. Top. Quantum Electron.*, vol. 3, pp. 905-915, 1997.
- [80] A. Cho, *Molecular Beam Epitaxy*. Woodbury, NY: American Institute of Physics, 1994.
- [81] R. Williams, *Modern GaAs Processing Methods*. Boston: Artech House, 1990.
- [82] S. K. Ghandhi, *VLSI Fabrication Principles: Silicon and Gallium Arsenide*, 2nd Ed. New York: J. Wiley, 1994.
- [83] R. T. Huang, and D. Renner., "Improvement in dark current characteristics and long-term stability of mesa InGaAs/InP p-i-n photodiodes with two-step SiN_x surface passivation," *IEEE Photonics Technol. Lett.*, vol. 3, pp. 934-936, 1991.
- [84] G. A. Porkolab, Y. J. Chen, S. A. Merritt, S. A. Tabatabaei, S. Agarwala, F. G. Johnson, O. King, M. Dagenais, R. A. Wilson, and D. R. Stone, "Wet-chemistry surface treatment for dark-current reduction that preserves lateral dimensions of reactive ion etched $\text{Ga}_{0.47}\text{In}_{0.53}\text{As}$ p-i-n diode photodetectors," *IEEE Photonics Technol. Lett.*, vol. 9, pp. 490-492, 1997.
- [85] R. Yeats and K. Von Dessonneck, "Polyimide passivation of $\text{In}_{0.53}\text{Ga}_{0.47}\text{As}$, InP, and InGaAsP/InP p-n junction structures," *Appl. Phys. Lett.*, vol. 44, pp. 145-147, 1984.
- [86] G. B. Stringfellow, *Organometallic Vapor-Phase Epitaxy: Theory and Practice*, 2nd Ed. San Diego: Academic Press, 1999.
- [87] D. B. Young, J. W. Scott, F. H. Peters, M. G. Peters, M. L. Majewski, B. J. Thibeault, S. W. Corzine, and L. A. Coldren, "Enhanced performance of offset-gain high-barrier vertical-cavity surface-emitting lasers," *IEEE J. Quantum Electron.*, vol. 29, pp. 2013-2022, 1993.
- [88] K. H. Gulden, M. Moser, S. Luscher, and H. P. Schweizer, "High performance near-IR (765nm) AlAs/AlGaAs vertical cavity surface emitting lasers," *Electron. Lett.*, vol. 31, pp. 2176-2179, 1995.
- [89] Y. H. Lee, B. Tell, K. F. Brown-Goebeler, R. E. Leibenguth, and V. D. Mittera, "Deep-red continuous wave top-surface-emitting vertical-cavity AlGaAs superlattice lasers," *IEEE Photonics Technol. Lett.*, vol. 3, pp. 108-109, 1991.

- [90] J. A. Lott, and H. K. Shin, "Red and deep red vertical cavity surface emitting lasers with top and bottom AlGaAs/Al-oxide distributed Bragg reflectors and AlGa-oxide current apertures," *23rd International Symposium on Compound Semiconductors*, pp. 377-380, Sept. 1996.
- [91] R. P. Schneider, Jr., J. A. Lott, K. L. Lear, K. D. Choquette, M. H. Crawford, S. P. Kilcoyne, and J. J. Figiel, "Metalorganic vapor phase epitaxial growth of red and infrared vertical-cavity surface-emitting laser diodes," *J. Crystal Growth*, vol. 145, pp. 838-845, 1994.
- [92] H. E. Shin, Y. G. Ju, J. H. Shin, J. H. Ser, T. Kim, E. K. Lee, I. Kim, and Y. H. Lee, "780nm oxidized vertical-cavity surface-emitting lasers with Al₁₁Ga_{0.89}As quantum wells," *Electron. Lett.*, vol. 32, no. 14, pp. 1287-1288, July 1996.
- [93] J. W. Scott, R. S. Geels, S. W. Corzine, and L. A. Coldren., "Modeling temperature effects and spatial hole burning to optimize vertical-cavity surface-emitting laser performance," *IEEE J. Quantum Electron.*, vol. 29, pp. 1295-1308, 1993.
- [94] B. J. Thibeault, J. W. Scott, M. G. Peters, F. H. Peters, D. B. Young, and L. A. Coldren, "Integrable InGaAs/GaAs vertical-cavity surface-emitting lasers," *Electron. Lett.*, vol. 29, pp. 2197-2199, 1993.
- [95] E. Thrush, O. Levi, K. Wang, M. A. Wistey, S. J. Smith and J. S. Harris, Jr., "High throughput integration of optoelectronic devices for biochip fluorescent detection," *Proc. SPIE.*, vol. 4982, pp. 162-169, Jan. 2003.
- [96] C. P. Chao, S. Y. Hu, P. Floyd, K. K. Law, S. W. Corzine, J. L. Merz., A. C. Gossard, and L. A. Coldren, "Fabrication of low-threshold InGaAs/GaAs ridge waveguide lasers by using in situ monitored reactive ion etching," *IEEE Photonics Technol. Lett.*, vol. 3, pp. 585-587, 1991.
- [97] J. H. Kim, D. H. Lim, and G. M. Yang, "Selective etching of AlGaAs/GaAs structures using the solutions of citric acid H₂O₂ and de-ionized H₂O buffered oxide etch," *J. Vac. Sci. Technol. B*, vol. 16, no. 2, pp. 558-560, 1998.
- [98] K. D. Choquette, K. M. Geib, C. I. H. Ashby, R. D. Twesten, O. Blum, H. Q. Hou, D. M. Follstaedt, B. E. Hammons, D. Mathes, and R. Hull, "Advances in selective wet oxidation of AlGaAs Alloys," *IEEE J. Sel. Top. Quantum Electron.*, vol. 3, pp. 916-926, 1997.
- [99] G. A. Porkolab, Y. J. Chen, S. A. Tabatabaei, S. Agarwala, F. G. Johnson, O. King, M. Dagenais, R. E. Frizzel, W. T. Beard, Jr., and D. R. Stone, "Air-bridges, air-ramps, planarization, and encapsulation using pyrolytic photoresist in the fabrication of three-dimensional microstructures," *J. Vac. Sci. Technol. B*, vol. 15, no. 6, pp. 1961-1965, Nov. 1997.

- [100] K. M. Geib, K. D. Choquette, D. Serkland, A. A. Allerman, and T. W. Hargett, "Fabrication and performance of two-dimensional matrix addressable arrays of integrated vertical-cavity lasers and resonant cavity photodetectors," *IEEE J. Select. Topics Quantum Electron.*, vol. 8, no. 4, pp. 943-947, July 2002.
- [101] P. K. Seigal, R. D. Briggs, D. J. Rieger, A. G. Baca, and A. J. Howard, "Adhesion studies of GaAs-based ohmic contact and bond pad metallization," *Thin Solid Films*, vol. 291, pp. 503-507, 1996.
- [102] S. Donati, *Photodetectors: Devices, Circuits, and Applications*. Upper Saddle River, NJ: Prentice Hall, 2003.
- [103] E. Thrush, O. Levi, K. Wang, M. A. Wistey, S. J. Smith and J. S. Harris, Jr., "Integrated semiconductor fluorescent detection system for biochip and biomedical applications," *Proc. SPIE*, vol. 4626, pp. 289-297, 2002.
- [104] M. Dentan, and B. D. Cremoux, "Numerical simulation of the nonlinear response of a p-i-n photodiode under high illumination," *J. Lightwave Technol.*, vol. 8, pp. 1137-1144, 1990.
- [105] L. Y. Lin, M. C. Wu, T. Itoh, T. A. Vang, R. E. Muller, D. L. Sivco, and A. Y. Cho., "High-power high-speed photodetectors-design, analysis, and experimental demonstration," *IEEE Trans. Microw. Theory Tech.*, vol. 45, pp. 1320-1331, 1997.
- [106] H. Liu, P. K. Dasgupta, and H. J. Zheng, "High performance optical absorbance detectors based on low noise switched integrators," *Talanta*, vol. 40, pp. 1331-1338, 1993.
- [107] F. Nabiev, and C. J. Chang-Hasnain, "Voltage drop in n- and p- type Bragg reflectors for vertical-cavity surface-emitting lasers," *IEEE Photon. Tech. Lett.*, vol. 7, pp. 733-735, 1995.
- [108] K. L. Lear, and R. P. Schneider, Jr., "Uniparabolic mirror grading for vertical cavity surface emitting lasers," *Appl. Phys. Lett.*, vol. 68, pp. 605-607, 1996.
- [109] E. Thrush, O. Levi, L. J. Cook, J. Deich, S. J. Smith, W. E. Moerner, J. S. Harris, Jr., "Laser background characterization in a monolithically integrated bio-fluorescence sensor," *Proceedings of SPIE*, vol. 5318, pp. 59-66, 2004.
- [110] E. Thrush, O. Levi, W. Ha, A. Kurtz, J. Hwang, S. J. Smith, W. E. Moerner, J. S. Harris, Jr., "Integrated semiconductor fluorescence sensor for portable biomedical diagnostics," *Conference on Lasers and Electro Optics-CLEO '03*, Baltimore, MD, June 2003.

- [111] E. Thrush, O. Levi, W. Ha, G. Carey, L. J. Cook, J. Deich, S. J. Smith, W. E. Moerner, and J. S. Harris, Jr., "Laser background rejection optimization in integrated optoelectronic fluorescence sensor," *Proceedings of μ TAS*, vol. 1, pp. 363-366, Oct. 2003.
- [112] E. Thrush, O. Levi, L. J. Cook, S. J. Smith, and J. S. Harris, Jr., "Greater than 10^6 optical isolation in integrated optoelectronic fluorescence sensor," *IEEE-EMBS Special Topic Conference on Microtechnologies in Medicine & Biology*, pp. 2080-2081, Sept. 2004.
- [113] C. C. Lin, D. G. Deppe, and C. Lei, "Role of waveguide light emission in planar microcavities," *IEEE J. Quantum Electron.*, vol. 30, pp. 2304-2313, 1994.
- [114] A. Onischenko, and J. Sarma, "Analysis of vertical and in-plane spontaneous emission in large diameter VCSELs," *IEEE Proc. Optoelectronics*, vol. 144, pp. 39-43, 1997.
- [115] E. Thrush, O. Levi, W. Ha, K. Wang, S. J. Smith and J. S. Harris, Jr., "Integrated bio-fluorescence sensor," *J. Chromatography A*, vol. 1013, pp. 103-110, Sept. 2003.
- [116] S. P. Fodor, R. P. Rava, X. C. Huang, A. C. Pease, C. P. Holmes, and C. L. Adams, "Multiplexed biochemical assays with biological chips," *Nature*, vol. 364, pp. 555-556, 1993.
- [117] M. Schena, D. Shalon, R. W. Davis, and P. O. Brown, "Quantitative monitoring of gene expression patterns with a complementary DNA microarray," *Science* (Washington D.C.), vol. 270, pp. 467-470, 1995.
- [118] W. Budach, A. P. Abel, A. E. Bruno, and D. Neuschafer, "Planar waveguides as high-performance sensing platforms for fluorescence-based multiplexed oligonucleotide hybridization assays," *Anal. Chem.*, vol. 71, pp. 3347-3355, 1999.
- [119] E. Krioukov, D. J. W. Klunder, A. Driessen, J. Greve, and C. Otto, "Integrated optical microcavities for enhanced evanescent-wave spectroscopy," *Optics Letters*, vol. 27, no. 17, pp. 1504-1506, 2002.
- [120] J. Fritz, E. B. Cooper, S. Gaudet, P. K. Sorger, and S. R. Manalis, "Electronic detection of DNA by its intrinsic molecular charge," *Proc. Nat. Acad. Sci.*, vol. 99, no. 22, pp. 14142-6, 2002.
- [121] B. P. Nelson, T. E. Grimsrud, M. R. Liles, R. M. Goodman, and R. M. Corn, "Surface plasmon resonance imaging measurements of DNA and RNA hybridization adsorption onto DNA microarrays," *Anal. Chem.*, vol. 73, no. 1, pp. 1-7, 2001.

- [122] E. Thrush, O. Levi, L. J. Cook, J. Deich, S. J. Smith, W. E. Moerner, and J. S. Harris, Jr., "Integrated semiconductor bio-fluorescence sensor integrated on micro-fluidic platform." *Conference on Lasers and Electro Optics-CLEO '04*, San Francisco, CA, June 2004.
- [123] E. Thrush, O. Levi, L. J. Cook, J. Deich, A. Kurtz, S. J. Smith, W. E. Moerner, and J. S. Harris, Jr., "Monolithically integrated semiconductor fluorescence sensor for microfluidic applications," In press in *Sensors and Actuators B*, 2004.
- [124] H. J. Unold, S. W. Z. Mahmoud, R. Jager, M. Grabherr, R. Michalzik, and K. J. Ebeling, "Large-area single-mode VCSELs and the self-aligned surface relief," *IEEE J. Select. Topics Quantum Electron.*, vol. 7, no. 2, pp. 386-392, 2001.
- [125] D. J. Throckmorton, T. J. Shepodd, and A. K. Singh, "Electrochromatography in microchips: reversed-phase separation of peptides and amino acids using photopatterned rigid polymer monoliths," *Anal. Chem.*, vol. 75, pp. 784-789, 2002.